ROLE OF SURFACE-LIKE ELASTIC CONSTANTS IN THE PHENOMENOLOGY OF CONFINED NEMATICS

A Dissertation
Presented to
The Academic Faculty

by

Karthik Nayani

In Partial Fulfillment
of the Requirements for the Degree
Doctor of Philosophy in the
School of Material Science and Engineering, Georgia Institute of Technology

Georgia Institute of Technology
May 2017

ROLE OF SURFACE-LIKE ELASTIC CONSTANTS IN THE PHENOMENOLOGY OF CONFINED NEMATICS

Approved by:

Dr. Mohan Srinivasarao, Advisor
School of Material Science and Engineering
Georgia Institute of Technology

Dr. Alberto Fernandez-Nieves
School of Physics
Georgia Institute of Technology

Dr. Jung Ok Park
School of Material Science and Engineering
Georgia Institute of Technology

Dr. Paul Goldbart
School of Physics
Georgia Institute of Technology

Dr. Anselm Griffin
School of Material Science and Engineering
Georgia Institute of Technology

Date Approved: January 09, 2017

To my parents and my uncle

ACKNOWLEDGEMENTS

I would start off by thanking my advisor Dr. Mohan Srinivasarao without whom none of the work presented in this dissertation would have been possible. His methodology of allowing students to have unbridled freedom in choosing a research topic and performing experiments brings about the best in their creativity. It is truly a great platform to begin one's scientific journey. Further, his constant encouragement to read literature on a wide range of topics not limited to the focus of research has proven to be invaluable to me. He provided me with a wealth of opportunities to widen my exposure by ensuring I attend several conferences and summer schools which were vital to my development as a scientist.

I would then like to thank my committee member Dr. Alberto Fernandez-Nieves. I owe my understanding and knowledge of soft matter physics largely to the interactions and discussions with him. He has had a deep impression of how I think about physical phenomenon and this has been the most gratifying experience of graduate school. His passion and perseverance towards science is infectious and will serve as a constant motivation.

I thank my committee member Dr. Jung Ok Park for painstakingly reading all my written documents. Her advice in many matters and constant support are gratefully acknowledged.

I thank Dean Paul Goldbart and Dr. Anselm Griffin for taking the time to be in my committee. It is a great privilege to have them in the committee. I thank them for the discussions during the proposal defense which were truly illuminating and brought about

some aspects of the phenomenology discussed that we had never considered before. I also thank them for suggested edits and new questions posed during the defense.

I would like to thank Dr. Jinxin Fu who is a post-doc in Dr. Srinivasarao's lab. His expertise with optical and spectroscopic instruments has helped me become a better experimentalist. Much of the work in this thesis is a result of a fruitful collaboration with him. I thank Perry Ellis who is a graduate student with Dr. Fernandez-Nieves for always being his creative self. Many an idea discussed here was born out of a conversation with him and his out of the box thinking. My understanding of nematic elasticity increased constantly and significantly through interactions with him. I thank Rui Chang who is a graduate student in Dr. Srinivasarao's lab for her help with experiments. I also thank all the current and past group member of Srinivasarao and Fernandez-Nieves labs for their comradery and support.

My parents have supported me unflinchingly throughout my education process. Nothing I ever do can repay them. My uncle has had a significant influence in my choices with regard to education. It was his wise advice that convinced me that graduate school was the right choice after college. For that reason, I owe all my learning in graduate school and in the future to him. I thank my sister, my grandmother and my cousins for their unshakable belief in my ability. My wing-mates and my friends have always been there to share banter and offer advice. They and all my loved ones have my continued gratitude.

Funding from Renewable Bioproducts Institute at Georgia Institute of Technology is gratefully acknowledged.

TABLE OF CONTENTS

LIST OF TABLES

LIST OF FIGURES

SUMMARY

Confined nematics are a natural setting to study aspects relating to phenomenology of symmetry breaking, evolution and dynamics of topological defects. In this study we highlight the interplay of the surface-like elastic constants with the phenomenology mentioned above. We exploit nematics confined to cylinders to study a spontaneous reflection symmetry breaking phase transition. The role of saddle-splay elasticity in driving this transition is described in detail. We also confine nematics to rectangular geometries which reveal novel director and defect configurations. We uncover surprising aspects regarding the scaling of surface-like elastic constants by studying morphological transitions of spherical nematic droplets. We exploit a monodomain- like configuration and the director arrangement in tactoids to shed light on the physics governing the nematic-biphasic transition of lyotropic chromonic liquid crystals. We also confine nematics to toroidal geometries with radial anchoring to delineate the coupling of geometry with the director configuration. Finally, the role of differential polarizability is demonstrated in the accurate determination of order parameters of liquid crystals.

CHAPTER 1. INTRODUCTION

1.1 Nematic liquid crystals

A crystalline solid has all its constituents located in a fixed periodic array and has both translational and orientational order. In complete contrast, an isotropic fluid phase has neither translational nor orientational order. Besides the conventional solid and isotropic fluid phases, there can exist other interesting phases of matter which display intermediate symmetry. The nematic liquid crystalline phase is a particularly exciting example of the said behavior [1,2]. Nematic liquid crystals are made of rod like molecules and possess orientational order that stems from the anisotropic shape and interactions of the constituent molecules. However, the centers of masses of these molecules have no translational order. Because of the intermediate symmetry, nematics possess several interesting properties. For instance, similar to fluids, nematic liquid crystals cannot resist a shear deformation, while the anisotropic shape and interactions result in having direction dependent properties like crystalline solids. These unique characteristics make liquid crystals well suited for a host of technological applications.

In addition to their technological relevance, nematic liquid crystals are a fascinating subject for testing and understanding the underlying physics relating to condensed matter. Identifying the symmetry (or broken symmetry) is a powerful way of understanding and predicting the behavior of a phase. Consider the phase transition from an isotropic phase to a nematic liquid crystalline phase. Clearly, the orientational symmetry of the isotropic phase is broken as the system undergoes a phase transition to the nematic phase. The order parameter characterizes the order in the phase of lower symmetry. Naturally, for nematic

liquid crystals the order parameter relates to the orientational distribution of the molecules in the system. With an appropriately chosen order parameter, it is possible to expand the free energy in the vicinity of the phase transition in powers of the order parameter[1]. The phenomenological approach of Landau can be used to describe the phase transition of many condensed matter systems. However, nematic liquid crystals happen to be one most convenient material to perform experiments which test several of these theoretical predictions. Further, with the help of appropriate phenomenological models, it is possible to predict the scaling behavior of several important physical characteristics of the phase. For instance, the scaling of the surface elastic constants with order parameter for nematics liquid crystals is an avenue that has not been addressed rigorously. We use experiments on confined liquid crystals as means to address this fundamental question and others of similar spirit.

Further, nematic liquid crystals are also a convenient playground to study topological defects. For ordered media, defect is a region where it is not possible to define the order parameter locally[3]. The distinguishing aspect of topological defects from other kinds of defects in an otherwise uniform medium is that, it is not possible to remove a topological defect by simple modifications to the local properties of the system. Herein lies the origin of the term topological. Homotopy theory provides the natural language for using the order parameter space to describe and classify defects in ordered systems [3,4]. In addition to revealing the symmetry of the phase, dynamics of defects provide wealth of information. Further, the study of dynamic evolution of defects produced in symmetry breaking phase transitions is a central problem in cosmology, particle physics and condensed matter physics[5].

Confined nematics are a natural setting to study both sets of phenomenology described above. We exploit nematics confined to cylinders to study a spontaneous reflection symmetry breaking phase transition. We also explore the dynamics of the novel defect configurations thus created. Further, we uncover surprising aspects regarding the scaling of surface-like elastic constants by studying the anchoring transitions of spherical nematic droplets. We also confine nematics to rectangular and toroidal geometries and study the coupling of geometry with the director configuration.

1.1.1 Confined Nematics

When nematic liquid crystals are confined to flat boundaries with planar boundary conditions, the ground state is a trivial configuration, where all molecules point along a specific direction, referred to as the easy axis of the director. Confinement of nematics to curved geometry results in a much richer phenomenology. The chosen ground state depends on the delicate balance between elastic, surface and external fields. Further, confined nematics like any other ordered material need to satisfy certain topological constraints depending on the nature of confinement. For instance, a crystalline lattice made of spherical particles covering the surface of a sphere cannot maintain its six-fold hexagonal close packing order all through the surface. In order to fill space, there need to be a minimum of 12 spheres that have five nearest neighbors in place of six[6]. Similarly, when nematics liquid crystals are confined to a sphere, there will be regions on the surface where the nematic director cannot be defined. These regions are termed as topological defects. The added requirement of satisfying topological constraints in addition to minimizing the free energy contributes to the added richness of the phenomenology of confined nematics. Further, confined nematics are excellent candidates for the

development of opto-electronic materials. Hence, there is added impetus for understanding the underlying physics of nematics under confinement.

1.2 **Nematic elasticity**

Governed by anisotropic interactions, the constituent molecules of a nematics tend to align parallel to each other along a common axis. The direction of the axis is described by a unit bivector **n**, known as the director. Any deformation of the uniform undistorted state costs energy. It is possible to construct a phenomenological continuum theory assuming weak deformation fields, i.e the deformations happen at a much larger length scale as compared to the molecular length ($\nabla n \ll \frac{1}{a}$), where a is the molecular length.

1.2.1 Frank's theory of elasticity

In his seminal work, Frank developed nematic elasticity along the lines of Hooke's description for solids[7]. The free energy density is treated as a quadratic function of the curvature strains and the analogues of the elastic moduli (referred to as Frank's elastic constants) appear as coefficients. The unit bi- vector **L** is chosen to represent the direction of preferred orientation in the neighborhood of any point. A local co-ordinate system is introduced with the z axis parallel to **L** at the origin. For this reference axis, the six components of the local curvature are:

"splay": $s_1 = \frac{\partial L_x}{\partial x}$, $s_2 = \frac{\partial L_y}{\partial y}$; "twist": $t_1 = -\frac{\partial L_y}{\partial x}$; $t_2 = \frac{\partial L_x}{\partial y}$; "bend": $b_1 = \frac{\partial L_x}{\partial z}$; $b_2 = \frac{\partial L_y}{\partial z}$ (1.1)

Figure 1.1 illustrates these elementary deformations. Expanding the components of the orientation vector to the leading order in the deformation terms, we get:

$$L_x = a_1 x + a_2 y + a_3 z + O(r^2);$$

$$L_x = a_4 x + a_5 y + a_6 z + O(r^2); \quad (1.2)$$

$$L_z = 1 + O(r^2)$$

Where, $s_1 = a_1,\ t_2 = a_2,\ b_1 = a_3, -t_1 = a_4, s_2 = a_5,\ b_2 = a_6$;

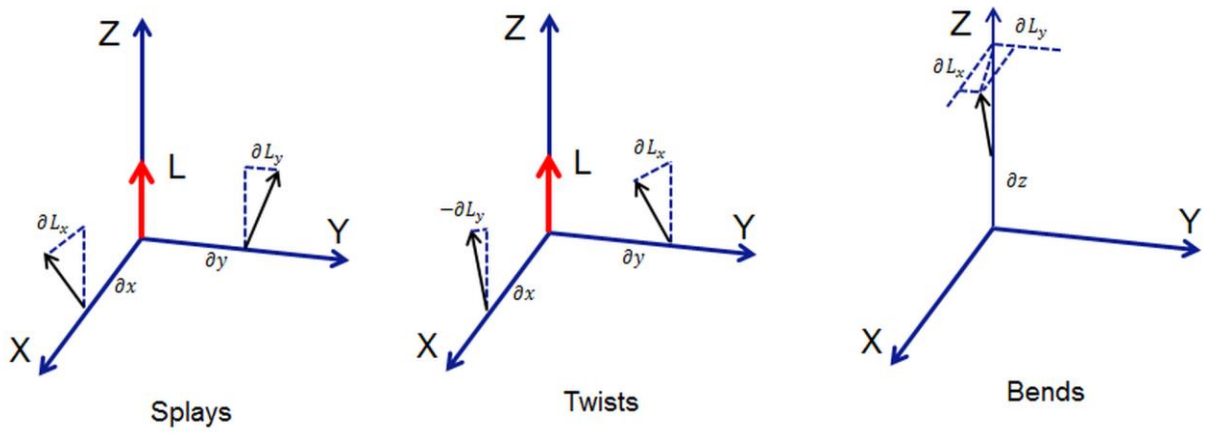

Figure 1.1 Splay, twist and bend deformations in the local co-ordinate frame

The free energy density can then be expressed as:

$$g = k_i a_i^{`} + \frac{1}{2} k_{ij} a_i^{`} a_j^{`} \quad (1.3)$$

The coefficient matrix, which consists of 36 terms, reduces to 4 terms using arguments of symmetry. The free energy density reads:

$$g = \frac{1}{2} k_{11}(s_1 + s_2)^2 + \frac{1}{2} k_{22}(t_1 + t_2)^2 + \frac{1}{2} k_{33}(b_1 + b_2)^2 - (k_{22} + k_{24})(s_1 s_2 + t_1 t_2) \quad (1.4)$$

Where, K_{11}, K_{22}, K_{33} are the elastic constants corresponding to the bulk splay, twist and bend terms, while K_{22}+K_{24} is the elastic constant associated with the saddle-splay contribution.

Clearly, Frank's model is one of phenomenological nature. Prior to Frank's work, Oseen had developed a model for liquid crystal elasticity using a molecular approach. The molecular model of Oseen and later work by Nehring and Suape include another term in the description of liquid crystal elasticity to the lowest order[8]. With the mixed splay-bend included, the elastic description of nematics truncated to the second order of deformation terms looks like:

$$F = \frac{1}{2}\int dV[K_{11}(\nabla \cdot \boldsymbol{n})^2 + K_{22}(\boldsymbol{n} \cdot \nabla \times \boldsymbol{n})^2 + K_{33}(\boldsymbol{n} \times \nabla \times \boldsymbol{n})^2 - (K_{24} + K_{22})\nabla \cdot (\boldsymbol{n}(\nabla . \boldsymbol{n}) + \boldsymbol{n} \times \nabla \times \boldsymbol{n}) + K_{13}(\nabla \cdot (\boldsymbol{n}(\nabla . \boldsymbol{n}))\,] \quad (1.5)$$

1.2.2 Description of Surface-like elastic constants in the liquid crystal literature

Although derived from the same principles as the bulk elastic constants, the K_{24} and K_{13} contributions to the free energy have often been neglected. We note that both these terms are pure divergence terms. It is possible to use Gauss's theorem to represent the volume integral of the divergence of these two terms as surface integrals. For this reason K_{24} and K_{13} have been referred to as surface elastic constants. This nomenclature is misleading as the deformations that these two elastic constants denote are truly bulk deformations which under the appropriate conditions can also be evaluated with a surface integral. For this reason, it is more appropriate to label them as "surface-like" elastic constants [8].

A common argument used to justify neglecting the two terms in the liquid crystal literature is that the gradients in the director field were assumed to be negligible when approaching the infinitely removed boundary. However, the important distinction is that,

the divergence term has to be calculated all throughout the bulk. Furthermore, unlike other fields of condensed matter, boundaries are crucial in understanding the behavior of liquid crystals and they are seldom infinitely removed from the bulk.

Consider a spherical droplet with radial boundary conditions with the director being defined as n_r=1, $n_\theta = 0$, $n_\emptyset$=0. We write the individual deformation terms (non-zero) of the Free energy contribution:

For this configuration; $(\nabla.n)^2 = \frac{1}{r^2}$ and $\nabla.\left(\mathrm{n}(\nabla.n)\right) = \frac{1}{r^2}$

Hence, $F_{radial} = 4\pi R(2K_{11} - (K_{24} + K_{22}) + 2K_{13})$

Looking at the expressions for the individual contributions and the overall free energy, we see that, not only are the contributions of the surface-like terms non-negligible but they also have the same functional form as the splay contribution. Clearly, the surface-like contributions cannot be neglected no matter how small or how large the droplet's size ($R\rightarrow\infty$).

In this thesis, we focus on the saddle-splay elastic contribution to the director organization in several different confining geometries. Recent experiments that have demonstrated the pivotal role played the saddle-splay contribution in the phenomenology pertaining to toroidal confinement [9] has grabbed our attention towards this subject as well as that of several others [10-13].

1.2.3 Contribution of the saddle-splay term for the case of planar anchoring

We have seen in the description of Frank's elasticity in the section above that the saddle-splay term in the local frame of reference is given by: $-(k_{22}+k_{24})(s_1 s_2 + t_1 t_2)$. For the case of planar anchoring, it is possible to re-express the saddle- splay term in terms of the principal curvatures of the confining surfaces. This treatment brings about the coupling of the saddle-splay term with the geometry of the confining boundary in a intuitive form. The mathematical treatment is shown below [11]:

We start from the expression of Frank's free energy

$$F = \frac{1}{2}\int dV[K_{11}(\nabla \cdot \boldsymbol{n})^2 + K_{22}(\boldsymbol{n} \cdot \nabla \times \boldsymbol{n})^2 + K_{33}(\boldsymbol{n} \times \nabla \times \boldsymbol{n})^2 - (K_{24}+K_{22})\nabla \cdot (\boldsymbol{n}(\nabla.\boldsymbol{n}) + \boldsymbol{n} \times \nabla \times \boldsymbol{n})]$$

Contribution of the saddle- splay term is:

$$F_{24} = -\frac{1}{2}(K_{24}+K_{22})\int dV[\,\nabla \cdot (\boldsymbol{n}(\nabla.\boldsymbol{n}) + \boldsymbol{n} \times \nabla \times \boldsymbol{n})]$$

Converting it to a surface integral using Gauss's theorem:

$$F_{24} = -\frac{1}{2}(K_{24}+K_{22})\int dS[\,\nu \cdot (\boldsymbol{n}(\nabla.\boldsymbol{n}) + \boldsymbol{n} \times \nabla \times \boldsymbol{n})]$$

Where, ν is the unit normal vector of the surface. For the case of planar anchoring, $\nu.\boldsymbol{n}$ =0, so the first term drops out leaving us with:

$$F_{24} = -\frac{1}{2}(K_{24}+K_{22})\int dS[\nu \cdot (\boldsymbol{n} \times \nabla \times \boldsymbol{n})]$$

Consider $\boldsymbol{n} \times \nabla \times \boldsymbol{n}$**:**

$$(n \times \nabla \times n)_a = \in_{abc} n_b \in_{cpq} \partial_p n_q = \left(\delta_{ap}\delta_{bq} - \delta_{aq}\delta_{bp}\right) n_b \partial_p n_q = -n_b \partial_b n_a$$

Also, from product rule

$$\nu_b \partial_a n_b + n_b \partial_a \nu_b = \partial_a (\nu_b n_b) = 0$$

So, we can re-write the contribution of F_{24} as:

$$F_{24} = -\frac{1}{2}(K_{24} + K_{22}) \int dS[\nu \cdot (n.\nabla)n]$$

Defining the extrinsic curvature tensor as:

$L_{ij} = e_i.(e_j.\nabla)\nu$, where e_1 and e_2 are the directions of principal curvatures k_1, k_2.

$$F_{24} = -\frac{1}{2}(K_{24} + K_{22}) \int dS n_i L_{ij} n_j \ ;$$

From the definition of the principal curvature we have

$$F_{24} = -\frac{1}{2}(K_{24} + K_{22}) \int dS(k_1 n_1^2 + k_2 n_2^2)$$

Hence, the saddle-splay contribution can be expressed as $F_{24} = -\frac{1}{2}(K_{24} + K_{22}) \int dS(k_1 n_1^2 + k_2 n_2^2)$, where k_1 and k_2 are the principal curvatures at a point on the surface and n_1 and n_2 the director components along the corresponding directions. Figure 1a illustrates the principal curvatures of a cylinder with the help of a schematic.

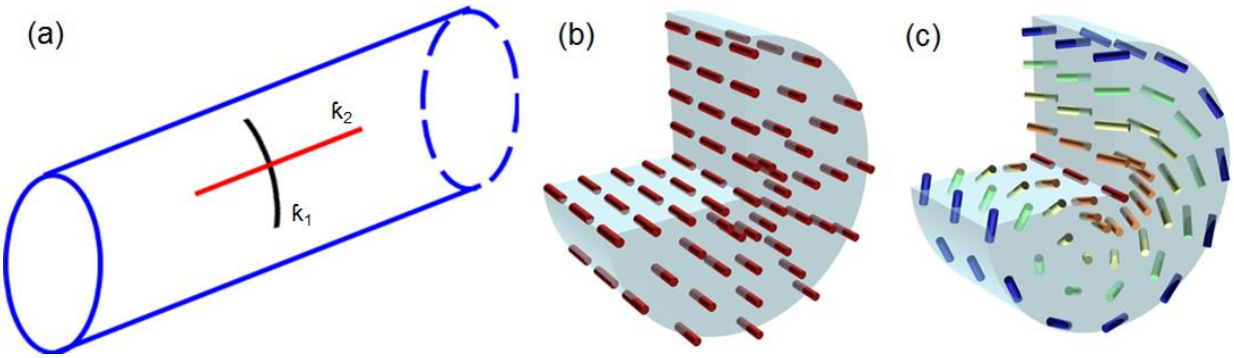

Figure 1.2 Schematics illustrating: (a) two principal curvatures of a cylinder (b) axial configuration (c) doubly-twisted configuration

This representation of saddle- splay contribution sheds tremendous insight on the role played by saddle splay when the two principal curvatures are different. For instance, a cylinder has: $n_1 = n_\theta$ and $n_2 = n_z$; hence $k_1 = 1/R$ and $k_2 = 0$. As a result, for the case of cylindrical geometry, the integral of F_{24} is minimized when the director at the surface is along the e_θ direction as opposed to an axial configuration wherein the director points along the z-axis (e_z). The axial configuration is illustrated in Figure 1.2b. Clearly, the contribution of the saddle-splay term for the axial configuration is zero.

There is a more intricate configuration for liquid crystals confined to a cylinder, which involves a significant contribution of the saddle-splay term. This configuration is the doubly-twisted configuration, which is illustrated in Figure 1.2c. The simplest representation of the director profile in this configuration is: n_r=0, $n_\theta = \omega\frac{r}{R}$, $n_z = \sqrt{1 - n_\theta^2}$, where, ω is a measure of the amount of twist. Recent experiments on liquid crystals confined to toroids clearly demonstrated the preference of the doubly-twisted director configuration over axial or concentric configurations [9,11]. For the simple ansatz described above, the contribution of the saddle-splay terms increases monotonously with increasing

twist angle (increasing twist angle implies a larger $n_\theta$component at the surface). Looking at the local frame of reference too, this configuration involves twist deformation along two perpendicular planes ($t_1 t_2 \neq 0$). Hence, the contribution of saddle-splay term increases with increasing twist angle and under the right conditions this structure can be the chosen ground state over the axial configuration [9,12]. We describe in greater detail the experimental finding of the doubly-twisted configuration for nematics confined to cylinders in Chapter 2.

1.3 **Organization of the thesis**

Having motivated the likelihood of the prominent role that the surface-like elastic constants might play under the appropriate confinement, we show the results pertaining to the cylindrical confinement of lyotropic chromonic liquid crystals (LCLCs) in Chapter 2. Saddle-splay elastic constant plays a key role in determining the ground state of LCLCs under cylindrical confinement. In Chapter 3 we continue the confinement studies of LCLCs. We explore the nematic organization in rectangular and square capillaries. The confinement studies on LCLCs reveal interesting physics pertaining to the aggregation behavior of these materials. This aspect is explored in Chapter 4 where Raman scattering measurements of order parameter and optical observations of tactoids reveal rich phenomenology relating to the nematic-isotropic transition of these materials. In Chapter 5, we perform experiments seeking to test an often neglected prediction of phenomenological theories pertaining to the scaling of the surface-like elastic constants. A surprising transition from bipolar to radial morphology is observed when nematics emulsions are heated sufficiently close to transition temperature. We explain this transition by appealing to the contrasting scaling of the saddle-splay elastic constant in comparison

to the bulk terms. Chapter 6 continues the theme of confinement experiments on nematics, but this time in the unique geometry of a torus. We study normally anchored nematic tori and discuss the coupling of the unique geometric features of the torus with the director organization. At several places in the thesis, we utilize Raman scattering measurements to determine the order parameters of the nematic phase. Chapter 7 discusses the role of a molecular property called differential polarizability in obtaining reliable data using this technique. We have used LCLCs as the choice of nematic phase at various junctures in this thesis to ask and try to answer some fundamental questions. Chapter 8 however discusses the aspect of aligning LCLCs for using them in technological applications. We use a previously reported extension of Berreman's theory to discuss the ideal experimental profiles of tessellated patterns which are commonly used for aligning liquid crystals.

CHAPTER 2. ROLE OF SADDLE-SPLAY ELASTICITY IN DETERMINING THE GROUND STATE OF CHROMONIC LIQUID CRYSTALS CONFINED TO CYLINDRICAL CAPILLARIES

After the discussion on the role of saddle-splay elastic constant on confined nematics and in particular with respect to cylindrical confinement, we discuss the experiments pertaining to the cylindrical confinement of lyotropic chromonic liquid crystals (LCLCs) in this chapter.

2.1 Introduction

LCLCs are composed of plank like molecules with a poly-aromatic core and polar peripheral groups. The poly-aromatic cores stack face to face governed by π-π interactions[14,15]. At low concentrations the aggregates are short and orient randomly. As the concentration increases the aggregates increase in length and eventually form a nematic phase. Although Onsager's excluded volume theory would be the intuitive way to describe the isotropic-nematic transition of these lyotropic systems, it has been found that the critical concentration of isotropic-nematic transition is much lower than that predicted by Onsager[16]. Several models like Y-stacks and slip stacks have been suggested to address the discrepancy[17]. Another curious aspect of these phases is the fact that the twist elastic constant (K_{22}) is an order of magnitude lower than the splay (K_{11}) and bend (K_{33}) constants[18,19]. In this regard, LCLCs bear striking similarity with several other polymeric nematics whose K_{22}/K_{11} and K_{22}/K_{33} are of the same order of magnitude as LCLC's[20-23]. This seems to be a feature common to nematics whose constitutent nematogens are

composed of semiflexible units. These fascinating features of LCLCs distinguish them from small molecule thermotropic nematics, thus conferring on confined LCLCs new and richer phenomenology.

Spontaneous reflection symmetry breaking has been observed previously in tactoids of disodium cromoglycate (DSCG)[24]. Competition of the twist and splay deformation energies has been used to describe the emergence of chirality of the twisted tactoids. Such an argument is particularly valid in the case of LCLCs due to the twist elastic constant being an order of magnitude smaller than the splay elastic constant. Similarly, spherical droplets of Sunset Yellow FCF (SSY) with planar boundary conditions also break reflection symmetry by relieving the costly splay close to the surface defects (boojums) with a twist deformation[25]. In both of these cases any permitted ground state with or without twist involves a deformation of the director. The uniqueness of our work lies in the fact that when confined to a cylindrical geometry with planar anchoring, we uncover a configuration with significant distortions, even though there exists a configuration free of director deformations, the axial configuration, where the director lies along a cylindrical axis. We demonstrate that the often-neglected saddle-splay (K_{24}) contribution is crucial in stabilizing the observed twisted director profile in cylindrical capillaries. Provided there is sufficient anisotropy between the saddle-splay and the twist elastic constants, the saddle-splay term not only screens the twist but also stabilizes the director deformation by decreasing the free energy of the twisted configuration below that of the deformation-free structure.

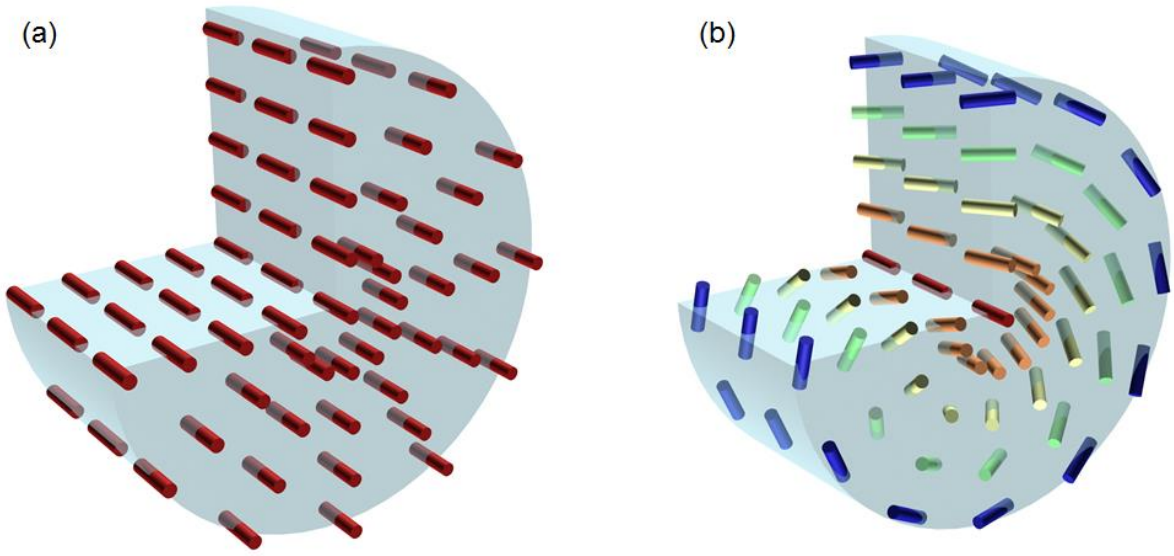

Figure 2.1 Schematics of director configurations in a cylindrical capillary: (a) Axial and (b) Double twist.

2.2 Director configuration in LCLCs confined to cylinders

2.2.1 Polarized optical microscopy observations

Consider an axial director profile as illustrated in Figure 2.1a. For this director configuration the intensity profile of the transmitted light is of the form: $I \propto sin^2(2\emptyset_p)$, where $\emptyset_p$ is the angle between the director and the polarizer. The intensity is a minimum when the director is either parallel or perpendicular to the incident polarization, corresponding to complete extinction of the light. The maxima in the intensity correspond to the cases where the director makes an angle of 45° with respect to the incident polarization direction. POM images of two angular positions of a capillary filled with DSCG are shown in Figure 2.2a and 2.2b, which correspond to the long axis of the capillary being parallel and at 45° with respect to the incident polarization direction, respectively. It should be noted that neither one of these situations display the expected extinction of the

incident light. This truly remarkable feature points to the fact that we must have a twisted structure in place of an axial one. In an axial configuration, the image corresponding to Figure 2.2a would be one of complete extinction of light. Instead we see that the intensity in both Figures 2.2a and 2.2b are comparable. This implies that the plane of polarization of the incident light is rotated by the liquid crystal and upon exiting the capillary, it is at an angle to the analyzer that is not 0^o or 90^o. This is a classic signature of twist. A doubly twisted configuration, which could explain the observed experimental images is illustrated in Figure 2.1b. The director of this configuration is axial at the center of the cylinder and twists progressively as it approaches the surface. We confirm the anchoring at the surface of the cylinder is planar by studying the tactoids that nucleate when the LCLC is in the biphasic region. The inset of Figure 2.2a shows a bipolar tactoid, which serves as a confirmation that the surface anchoring is planar.

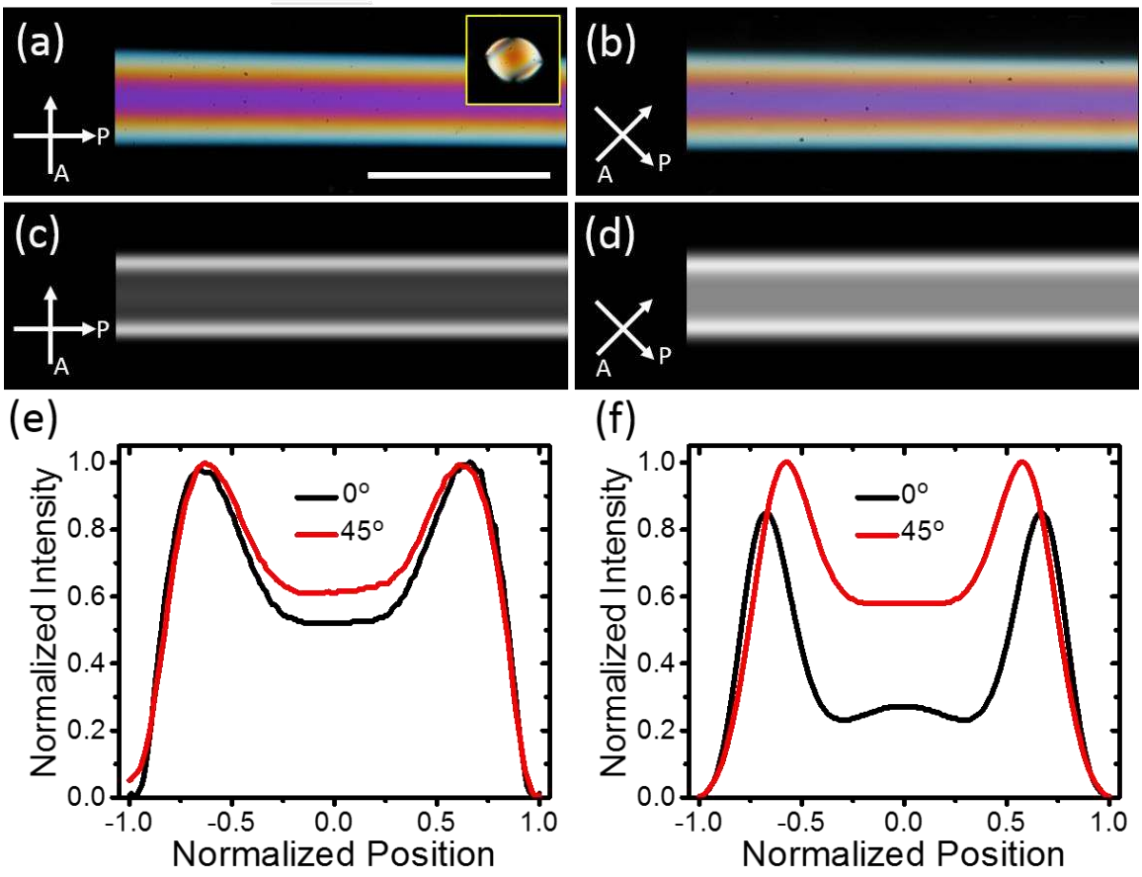

Figure 2.2 (a, b) Polarized optical microscope images of DSCG in a cylindrical capillary. Scale bar is 100 □m. The inset shows a bipolar tactoid of DSCG nucleating on the capillary wall in the biphasic temperature region under monochromatic light of 551 nm. (c, d) Simulation images of double twist configuration. (e) Intensity profiles of the cross sections of Fig 2(a) (black line) and 2(b) (red line). (f) Intensity profile of the cross section of Fig 2(c) (black line) and Fig 2(d) (red line).

2.2.2 Jones Matrix simulations of doubly-twisted structure

To test the hypothesis of double twist we perform Jones matrix simulations with a simple doubly twisted director ansatz. Jones matrices quantify the change in the polarization state as it traverses the sample. The director field is specified by $n=n_r e_r + n_\theta e_\theta + n_z e_z$ where e_r, e_θ and e_z are the orthonormal vectors in cylindrical coordinates, with $n_r=0$, $n_\theta = \omega\frac{r}{R}$, $n_z= \sqrt{1-n_\theta^2}$. The twist parameter ω determines the amount of twist in the

system; $\omega=0$ corresponds to an axial configuration. r is the radial distance from the center of the circular cross-section and R is its radius. Indeed, the simulated POM textures conform to the experimental observations that the light is not extinguished when the capillary long axis is parallel to the polarization of the incident light, which is evident from Figure 2.2c. Further we note that the intensity when the angle between the incident polarization direction and the cylindrical long axis is 45°, I_{45}, is always greater than the intensity when the angle between the incident polarization and the cylindrical long axis is 0°, I_0, which is also in agreement with the experimental observations. Furthermore, the intensity profiles along the cross-section of the sample of both experiments and simulations are consistent with each other, as shown in Figures 2.2e and 2.2f allude to this. The simulations capture the important characteristics of experimental profiles. The consistency of simulation and experiments indicates that doubly twisted configuration likely reflects the molecular arrangement inside the capillary.

We address the question of the driving force for the doubly twisted configuration over the axial configuration by considering the contribution of the saddle-splay (K_{24}) term in the free energy expression:

$$F = \frac{1}{2}\int dV[K_{11}(\nabla \cdot \boldsymbol{n})^2 + K_{22}(\boldsymbol{n} \cdot \nabla \times \boldsymbol{n})^2 + K_{33}(\boldsymbol{n} \times \nabla \times \boldsymbol{n})^2 - (K_{24} + K_{22})\nabla \cdot (\boldsymbol{n}(\nabla . \boldsymbol{n}) + \boldsymbol{n} \times \nabla \times \boldsymbol{n})] \quad (2.1)$$

Where, K_{11}, K_{22} and K_{33} are the Frank elastic constants associated with splay, twist and bend bulk deformations. The splay-bend (K_{13}) contribution has been a contentious topic in nematic elasticity, but we can safely neglect the K_{13} term in our study as we are dealing with a case of planar anchoring[26]. The role of the saddle splay term, which is

weighted with the elastic constant K_{24}, is subject to great debate. Several studies have neglected the contribution of saddle-splay under strong anchoring conditions. This argument stems from the fact the bulk integral of the saddle-splay can be reduced to a surface integral using Gauss's theorem, and that the contribution of saddle-splay on the surface would be negligible compared to the cost of anchoring violation. However, this argument is rather misguided as the saddle-splay contribution can only be neglected if the director depends only on one Cartesian coordinate, which is not the case in our experiments[26]. For planar anchoring, this implies that when the confining boundaries are curved, the contribution of K_{24} cannot be trivially neglected. Further in geometries like cylinders where the two principal curvatures are very different, the contribution of saddle splay can play a pivotal role in determining the director configuration.

We highlight the crucial role played by the saddle-splay term in the spontaneous reflection symmetry breaking of the director configuration resulting in a doubly twisted configuration for cylindrical confinement. For the case of planar anchoring, the saddle-splay term tends to align the director along the direction of largest principal curvature. This can be better understood when the contribution of K_{24} to the free energy per unit length is written in the form: $F_{24} = -\frac{1}{2}(K_{24} + K_{22}) \int dS(k_1 n_1^2 + k_2 n_2^2)$, where k_1 and k_2 are the principal curvatures at a point on the surface and n_1 and n_2 the director components along the corresponding directions. For a cylinder, $n_1 = n_\theta$ and $n_2 = n_z$; hence $k_1 = 1/R$ and $k_2 = 0$. As a result, for the case of cylindrical geometry, the integral of F_{24} is minimized when the director at the surface is along the e_θ direction. This drives the system to twist and provided that there is sufficient anisotropy of the elastic constants, the twisted structure is always stable. We tend to this argument with a simple theoretical model below.

2.3 Contribution of saddle-splay term to the free energy for the case of cylindrical confinement

The same ansatz, which was used for the Jones matrix simulations, is used for the theoretical calculations. We obtain an expression in leading order of ω for the free energy per unit length:

$$\frac{F}{2\pi K_{33}} = \frac{(K_{22}-K_{24})}{K_{33}}\omega^2 + \frac{\omega^4}{4} + \sum_3^{\infty}\frac{K_{22}}{K_{33}}\frac{\omega^{2n}}{2n} \quad (2.2)$$

The form of the free energy is completely analogous to the Landau theory of magnetism. It is, in fact, the sign of the quadratic term which controls whether the system adopts an axial configuration or breaks reflection symmetry, resulting in a doubly twisted director configuration. This theory is generic and would describe the reflection symmetry breaking of any nematic fluid. Provided $K_{24} > K_{22}$, the director is always going to be twisted. For LCLCs the low value of K_{22} confer them with the possibility of satisfying the twisting criterion. We can conclude that the value of K_{24} for the LCLCs used in the experiments is always greater than K_{22} as the director is twisted in all the experiments. Although our model is simplistic in terms of the ansatz used, we capture the essential physics with the criterion that $K_{24} > K_{22}$ for a twisted structure.

We note that the ansatz we use is the simplest we can assume for a double-twisted director ansatz. We have not minimized the Euler-Lagrange equation for the free energy assuming a general ansatz. This is the more rigorous treatment was performed elsewhere and the reader is referred to reference 27, where the treatment is described in detail. The ansatz so obtained has the form [27]: $n = cos\alpha\ sin\beta\ \hat{r} + sin\alpha sin\beta\hat{\theta} + cos\beta\hat{z}$ where, $\alpha=\frac{\pi}{2}$

and $\beta = \arctan(\frac{2\sqrt{K_{22}K_{24}(K_{24}-2K_{22})\frac{r}{R}}}{\sqrt{K_{33}}(K_{24}-(K_{24}-2K_{22})\frac{r^2}{R^2})}$. We note that the authors define the K_{24} term as $\frac{1}{2}K_{24}(\nabla\cdot(\boldsymbol{n}(\nabla.\boldsymbol{n})+\boldsymbol{n}\times\nabla\times\boldsymbol{n})]$ in place of $\frac{1}{2}(K_{24}+K_{22})\nabla\cdot(\boldsymbol{n}(\nabla.\boldsymbol{n})+\boldsymbol{n}\times\nabla\times\boldsymbol{n})]$ and hence the necessary accommodations have to be made when comparing the two ansatz and final free energy expressions.

From their description we note that while assuming a linear variation of the twist angle captures the essential physics some of the more intricate details relating to the intensity profiles are captured better by the ansatz obtained by minimizing the Euler-Lagrange equation for minimizing the free energy[27].

2.4 **Wave-guiding experiments for the measurement of twist angle**

To confirm the twisting criterion, we calculate the value of K_{24} by comparing the value of the twist parameter ω measured experimentally and that obtained after minimizing equation 2.2 with the experimental measure of ω. We determine the twist parameter by measuring the twist angle as one traverses the diameter of the cylinder. In the Mauguin limit, where $\phi \ll |\Gamma| = \left|\frac{2\pi}{\lambda}(n_e - n_o)d\right|$, with ϕ the total twist angle and Γ the retardation caused by the anisotropy of the refractive indices, the director field serves as a waveguide to the incident polarized light.

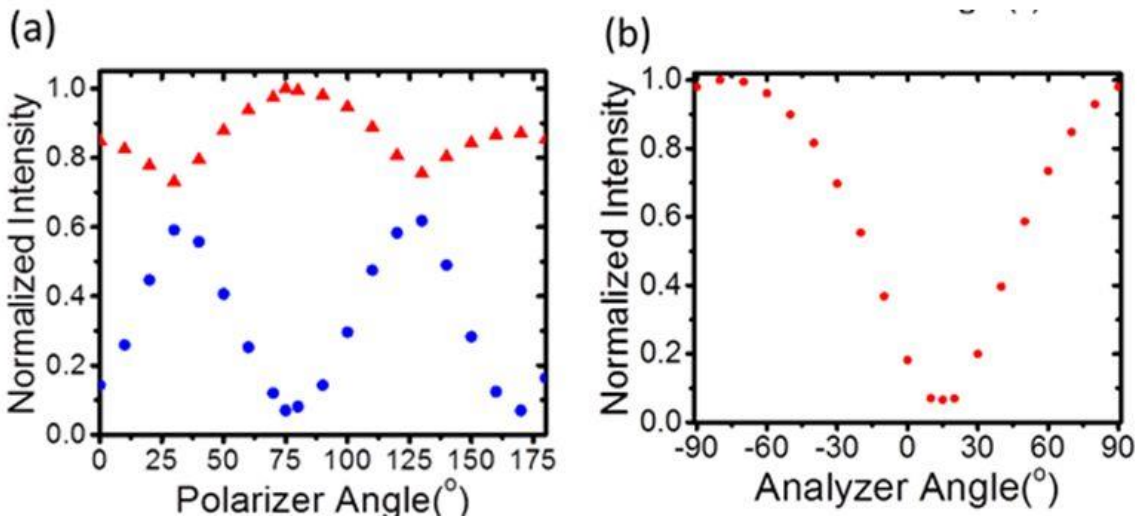

Figure 2.3 (a) The maximum (red triangle dots) and minimum (black square dots) transmitted intensities at every polarizer angle when analyzer is rotated throughout 180°. (b) The transmitted intensity at every analyzer angle when the polarizer is fixed at 75°.

As the birefringence, $n_e - n_o$, is fairly low (~0.02) for DSCG, we use capillaries of diameter 400 μm to satisfy the waveguiding requirement. When the waveguiding criterion is met, the minimum in transmitted intensity corresponds to the situation where, the entry polarization of the incident light is along the long axis (extraordinary waveguiding) or short axis (ordinary waveguiding) and the analyzer is perpendicular to the exit direction of the light. Theoretically this corresponds to zero transmitted intensity. To determine this specific polarizer analyzer combination, we first rotate the analyzer every 5 degrees and at a given polarizer orientation. Then, the polarizer is rotated by 5 degrees and the analyzer rotation is repeated for the new polarizer orientation. The red triangles and blue circles in Figure 3a show the maximum and minimum intensities so obtained for the different polarizer orientations. It is evident from **Error! Reference source not found.**a, the m inimum transmitted intensity corresponds to a polarizer angle of 75° for DSCG. For this polarizer orientation the transmitted intensity as a function of the analyzer rotation is shown

in Figure 2.3b. From the minimum in the plot of Figure 2.3b we estimate that the total twist angle is $(150 \pm 10)^{o}$.

2.4.1 Determination of the value of saddle-splay elastic constant

Since, within our ansatz, $\phi = 2 \sin^{-1}(\omega)$, we find that $\omega = 0.95 \pm 0.03$. Substituting the value of ω thus determined into the theoretical expression below:

$$\frac{K_{24}}{K_{33}} = \frac{1}{2}\left(\frac{2K_{22}}{K_{33}} + \omega^2 + \sum_3^{\infty} \frac{K_{22}}{K_{33}}\, \omega^{2n-2}\right) \tag{2.3}$$

We find that the range of $\frac{K_{24}}{K_{33}}$ for DSCG varies from 0.75 to 1.75 under the assumption that $\frac{K_{22}}{K_{33}} \sim 0.1$. We also perform the same experiment with SSY and obtain a twist angle close to 170^{o}. This would correspond to a value of $\frac{K_{24}}{K_{33}}$ of 6.75. We note that the exact value of $\frac{K_{24}}{K_{33}}$ is extremely sensitive to the value of the twist angle for large twists ($\omega \sim 1$). In comparison to small molecule liquid crystals like 5CB, we note that the value of K_{24} is significantly higher in comparison to the other elastic constants. For all the capillary dimensions (50, 100, 400 and 500 μm) used in the experiments, the twist angle measured is independent of the system size. This is another interesting aspect of our experimental system. Theoretically, we envision that very large values of twist per unit length can be obtained by cylindrical confinement of LCLCs. As the twist angle is independent of the system size, we can potentially confine LCLCs in as small a capillary as experimentally permitted and still obtain the same values of the twist angle. This makes our system a viable playground for a number of applications. We note that it is only the ratio of the elastic constants that dictates the magnitude of twist in the system. The obtained

values of $\frac{K_{24}}{K_{33}}$ are at odds with Ericksen's inequalities; these emerge on the basis that the Frank free energy is positive definite, with the minimum corresponding to a deformation free director. In our experiments the anisotropy of the elastic constants results in the formation of a ground state that is lower in energy than the deformation free ground state. Further, in the presence of a real interface we note that there is an interfacial K_{24} like term that arises from the interaction between nematic material and the boundary [28]. As the functional form of the two terms is identical it is not possible to measure only the contribution of the bulk K_{24} term with the wave-guiding measurements. This could also account for the dramatically higher value of K_{24} measured for LCLCs. Although, we note that this line of reasoning would hold true for thermotropic liquid crystals as well but the values of K_{24} experimentally measured for these materials is in expectation with theoretical simulations and in keeping with Ericksen's inequalities[9].

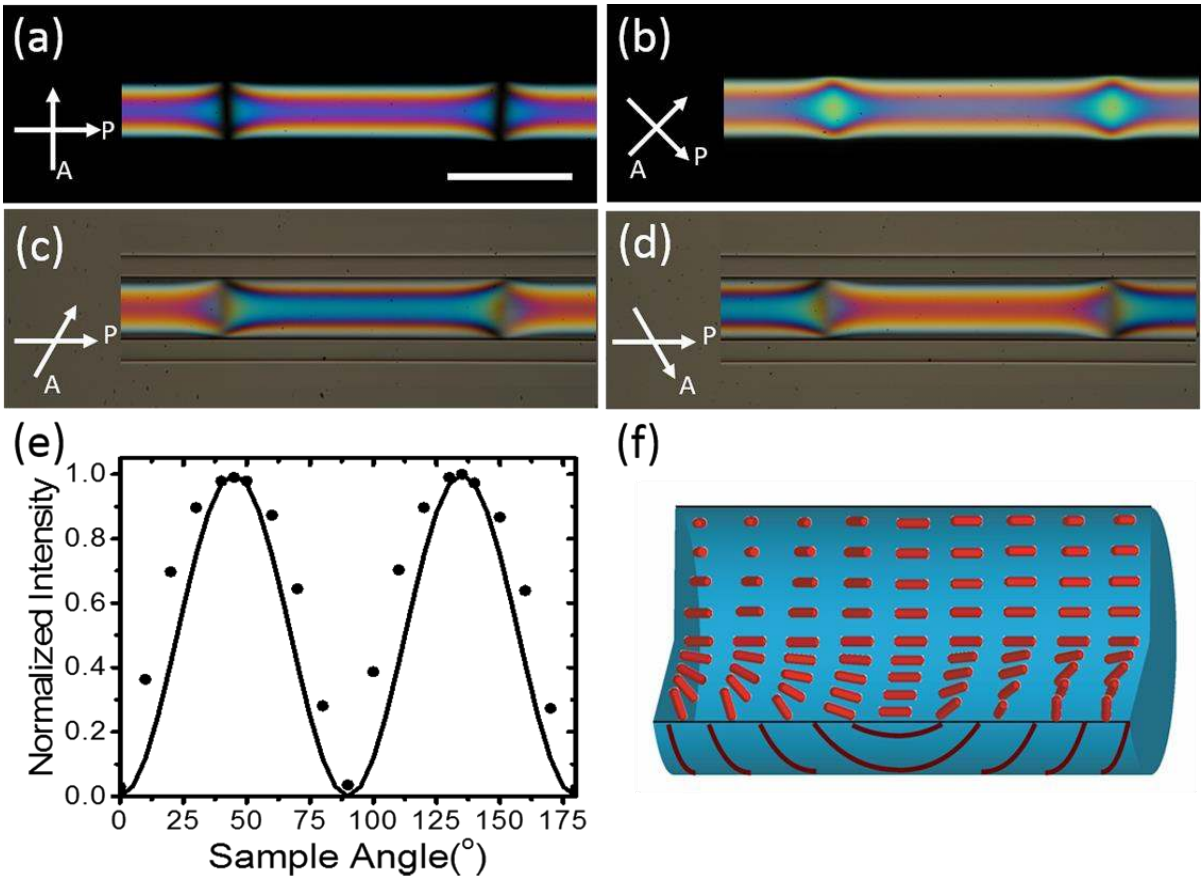

Figure 2.4 Polarized optical microscope images of DSCG in cylindrical capillaries with Neel Walls separating opposite twist handedness when the polarizer and analyzer make an angle of (a, b) 90o and (c, d) 60o. The opposite twist handedness is shown by the complementary intensity at complementary polarizer and analyzers. White arrows represent the direction of input polarizer (P) and analyzer (A). Scale bar is 100 um. (e) The intensity of the center of the wall region as the sample is rotated under crossed polarizers (black square dots) and the theoretical intensity profile of axial configuration (black line). (f) Corresponding schematic of the director alignment of the wall region.

2.5 Nature of defects separating oppositely twisted domains:

The sign of the twist parameter ω determines the handedness of the system and free energy is invariant to sign inversion. This implies that there is equal probability of finding domains of either handedness. Indeed, we see that there are multiple domains in a single capillary. Furthermore, these domains have opposite handedness and are separated by Neel

walls. Figure 2.4a demonstrates walls separating oppositely handed domains, where the sample is along the polarizer in a crossed polarizer setup. We note the extinction of the transmitted light from the center of the wall, indicating that it could be a Neel wall. In Figure 2.4b, where the sample makes an angle of 45^{o} with polarizer, the transmitted intensity is a maximum from the wall region. The intensity profile of the center of the wall as the sample is rotated under cross polarizers is reminiscent of an axial configuration as shown in Figure 2.4e. This confirms we, in fact, have a Neel Wall separating domains of opposite handedness, as illustrated in Figure 2.4f. We establish that the regions separated by the Neel wall are oppositely twisted from complementary polarizer and analyzer angles. For instance, the 60^{o} and -60^{o} as shown in Figure 2.4c and 2.4d, the domains show exactly complementary intensity profiles, which is a signature of opposite handedness of twist.

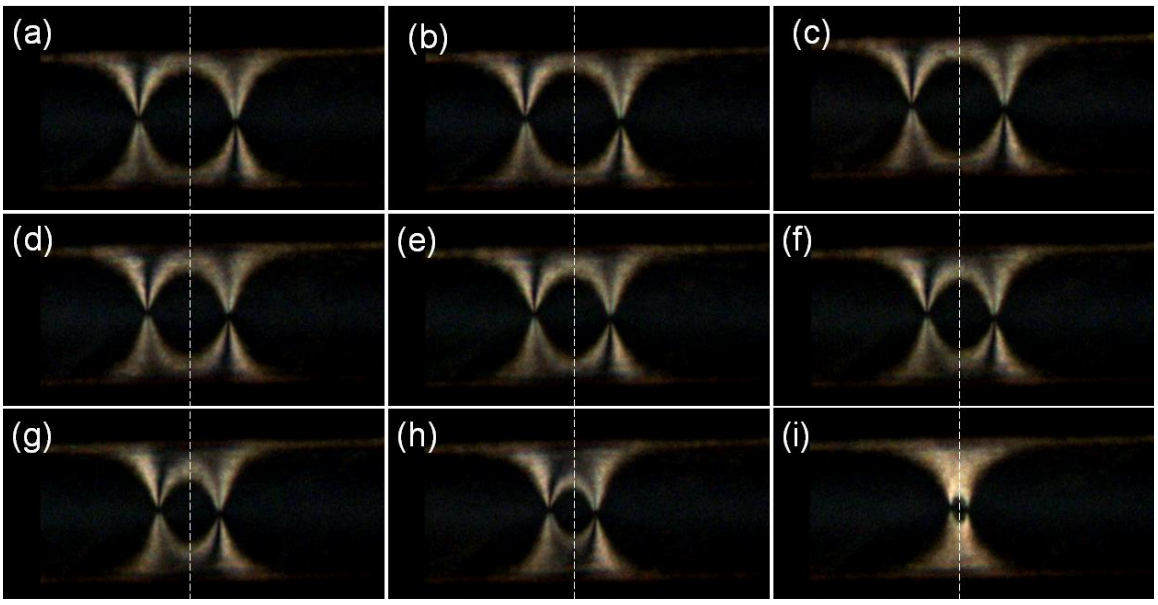

Figure 2.5 Doubly-twisted domain separated by point defects for SSY. a) to i) capture the stages of the annihilation dynamics of two oppositely charged defects. Dashed line is added along the midway plane between the two point defects to guide the eye.

2.5.1 Point defects separate oppositely twisted domains of SSY

Another well studied LCLC sunset yellow shows similar behavior as DSCG when confined to cylinders. However, the phenomenology differs in some critical details. We see that the doubly-twisted director configuration persists even for SSY but the twist angle measured from wave-guiding experiments is closer to 170^{o}. The higher twist angle for SSY confined to cylinder as compared to DSCG then corresponds to a higher relative value of K_{24}. We note that for DSCG, K_{24}/K_{33}~ 1 whereas the twist angle measurements of SSY correspond to a ratio of K_{24}/K_{33} ~ 5. In addition to the quantitative difference in the twist angle measured for the two LCLCs, the difference in the relative values of K_{24} also alters the qualitative phenomenology. As we described earlier, the regions of opposite handedness are separated by neel walls for DSCG. In contrast, regions of opposite twist are separated by point defects for SSY. This can be garnered from Figure 2.5.

The preference of either defect configuration can be rationalized by the local free energy cost surrounding the defect[13]. The detailed derivation is shown in the supporting information of reference 13. The preference of either configuration as a function of the relative cost of the saddle-splay elastic constant is plotted in Figure 2.6.

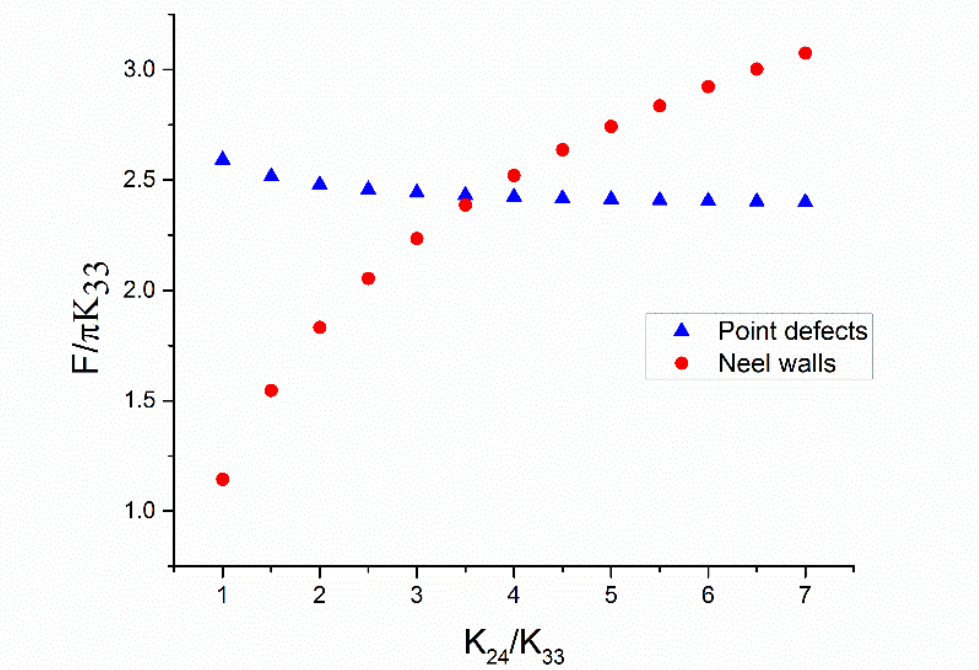

Figure 2.6 Free energy contribution of the configuration with neel walls and point defects

We gather from the plot that there is a transition around the relative cost of splay corresponding to K_{24}/K_{33} ~ 3.5 above which point defects are preferred as opposed to neel walls. The plot is consistent with our experiments[12,13].

The annihilation dynamics of these point defects is also of significance as it contrasts the behavior observed for hedgehogs [29]. Figure 2.5 shows snapshots of the annihilation process. We gather that the annihilation process is symmetric indicative of the local viscosities being identical for the two oppositely charged defects. This results from the fact that the director arrangement surrounding either defect is identical and involves the same deformations but in the opposite sense[27]. In contrast, the local arrangement of molecules surrounding a radial and hyperbolic hedgehog is quite different resulting in different local viscosities and hence asymmetric dynamics prior to annihilation[29]. Further

experiments are underway to quantify the dynamics of the annihilation process of the point defects observed in the doubly-twisted configuration.

2.6 **Conclusions**

In this chapter we demonstrated the emergence of spontaneous chirality when LCLCs are confined to cylinders with degenerate planar anchoring conditions. Remarkably the doubly twisted state is the chosen ground state even when there is a director configuration free of deformations. The contribution of the saddle-splay term drives the director to have a twisted structure. Our experiments present a unique and relatively straightforward path to measure the elastic constant K_{24} for LCLCs. This marks the first measurement of K_{24} for LCLCs. There is significant interest in the area of chiral separation of organic molecules in water. It has not escaped our attention that this configuration is an elegant platform for the detection and separation of chiral substances and enantiomers. We have shown that the LCLC has equal probability of acquiring one handedness and domains of opposite handedness are separated by a neel wall. These experiments highlight the fascinating aspect of highly anisotropic elastic constants, a distinctive feature of LCLCs. This coupled with the curved geometry results in various fascinating phenomena and hints towards richer phenomenology when LCLCs are confined in more exotic geometries.

2.7 **Materials and experimental details**

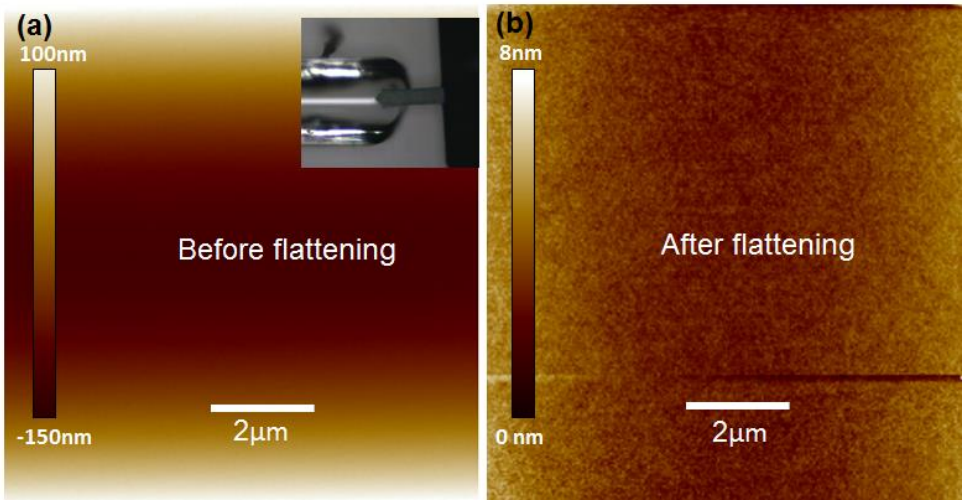

Figure 2.7 (a) Inner surface height profile of a 50µm-diameter cylindrical capillary, the inset shows the AFM tip scanning the bottom of the inner wall of the capillary; (b) The surface tomography of the inner wall by flattening image (a)

Aqueous solutions of SSY and DSCG were used in this study. Cylindrical capillaries (Vitrocom) of diameter 50, 100, 400 and 500 microns were used without any surface treatment. The capillaries were filled with 14, 16 and 18 wt% of DSCG and 30 wt% SSY by capillary force and then immediately sealed with epoxy to prevent water evaporation. The director profiles were interrogated using polarized optical microscopy (POM) (Leica DMRX Microsystem). In order to rule out any surface imperfections, we perform AFM measurements on the inner surface of the capillary.

CHAPTER 3. ROLE OF SADDLE-SPLAY ELASTICITY IN LYOTROPIC CHROMONIC LIQUID CRYSTALS CONFINED TO RECANGULAR AND SQUARE CAPILLARIES

After the results in the previous chapter on the confinement of LCLCs in cylinders, we present some counterintuitive results pertaining to LCLCs confined to rectangular and square capillaries.

3.1 Introduction

Liquid crystals under confinement have been a topic of interest for fundamental studies and application oriented research [30-34]. Confinement studies of liquid crystals have been performed for a range of geometries including spheres[25], cylinders[12,13,32], ellipsoids[24,35-37]. However, confinement studies in rectangular geometries are scarce[38]. This is perhaps due to the expectation of a simple axial configuration when nematics are confined to rectangles. However, in this chapter, we reveal rich physics pertaining to the confinement of LCLCs in rectangular capillaries.

We elucidate that in a rectangular capillary filled with SSY, a mono-domain like configuration evolves from an initially doubly-twisted director configuration, which forms due to the coupling of the curvature of the edges to the Frank free energy by the role of saddle-splay elasticity. The doubly-twisted region is eventually replaced by a planar monodomain in the center of the rectangle, and limited to the edges of the rectangular, with a defect line separating the two regions. In a square capillary, the doubly-twisted director

configuration remains the ground state because the energy cost of twist deformation is less than that of forming two defect lines.

3.2 **LCLCs confined to rectangles**

3.2.1 Polarized optical microscopy observations

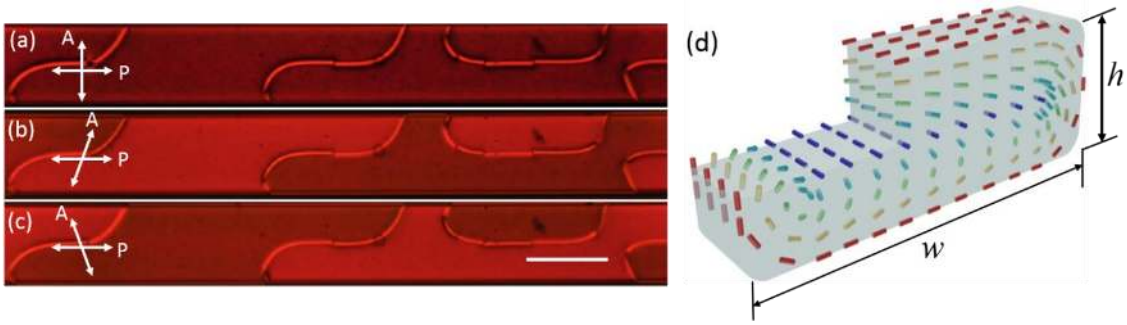

Figure 3.1 Crossed (a) and uncrossed (b)(c) polarized microscopic images of SSY with opposite twist domains in a rectangular capillary. Scale bar, 200 µm. (d) Schematic of the twisted director configuration in a rectangular capillary with thickness h=20µm and width *w*=200µm

Intuitively, an axial director profile with the director pointing along the long axis of the capillary is expected, when a liquid crystal is confined to a rectangular capillary with planar boundary conditions. This corresponds to a deformation free ground state. For an axial director configuration complete extinction is expected when the capillary is either parallel or perpendicular to the polarizers. This is in accordance with the expression for transmitted light intensity for the axial configuration: $I \sim \sin^2(2\varphi)\sin^2(\frac{\delta}{2})$, where φ is the angle between the director and the polarizer and δ is the phase retardation between ordinary and extraordinary light. However, in our experiments, after cooling the sample from isotropic to nematic phase, we find that there is transmitted light even when the capillary is parallel to the polarizer as shown in Fig. 3.1 (a). This hints that the director might be

twisted. Further, in the same figure, we can clearly see disclination lines that separate different domains. We establish that these are domains of opposite twist from the intensity profile of images obtained by uncrossing the polarizers. Fig. 3.1(b) and 3.1(c) correspond to images with polarizers making an angle of 70° and 110° with each other. As can be appreciated from Fig. 3.1 (b) and (c), the intensity profiles are complimentary for the two polarizer-orientations. This is an expected result if the light twists in an opposite sense in the two domains. Fig. 3.1(d) is a schematic that illustrates the doubly twisted director profile that is consistent with the experimental results.

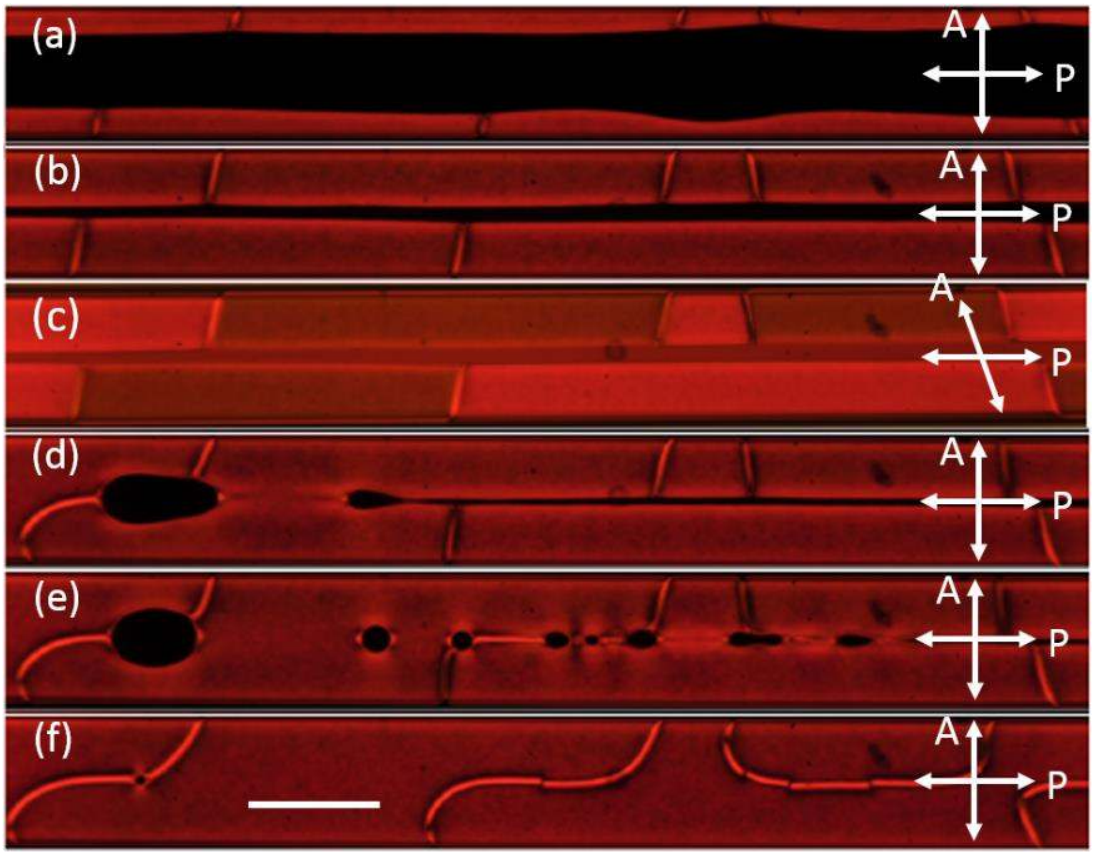

Figure 3.2 Time lapsed polarized microscopic images of SSY cooling down from isotropic phase to nematic phase. The twist region of random handedness nucleates at the edges and expands to the entire capillary. Polarizer and analyzer are crossed in (a)(b) and (d) (e) (f), uncrossed in (c). Scale bar is 200 µm

When the sample is cooled from the isotropic phase, we observe that the twist originates at the edges of the capillary. This is shown in Fig. 3.2 (a). The twisted fronts approach each other upon further cooling, engulfing the isotropic region in the center as shown in Fig. 3.2 (b)-(e). From the uncrossed polarized image of Fig. 3.2 (c), we see that there are domains of opposite twist at both edges, which are separated by disclination lines. The twisted domains are spatially random and have equal probability of acquiring either handedness. When the two twisted fronts meet in the center, the twisted domains of the same handedness merge; while the ones with opposite handedness are separated by disclination lines. This can be clearly seen by comparing Fig. 3.2 (c) with Fig. 3.2 (f).

3.2.2 Scaling arguments for free energy contributions

We explain using scaling arguments, the preference of a doubly-twisted director configuration as opposed to an axial configuration. We start with a simplistic assumption of treating the rectangular capillary as two flat planes capped with a semi-cylindrical edges, as illustrated in Fig. 3.1(d). Near the curved edges, the director would favor a doubly twisted profile. This is rationalized by the contribution of the saddle-splay term which lowers the free energy of the doubly-twisted director configuration. Consider the Frank free energy expression:

$$F = \frac{1}{2}\int dV[K_{11}(\nabla \cdot \boldsymbol{n})^2 + K_{22}(\boldsymbol{n} \cdot \nabla \times \boldsymbol{n})^2 + K_{33}(\boldsymbol{n} \times \nabla \times \boldsymbol{n})^2 - (K_{24} + K_{22})\nabla \cdot (\boldsymbol{n}(\nabla . \boldsymbol{n}) + \boldsymbol{n} \times \nabla \times \boldsymbol{n})] \quad (3.1)$$

Where, K_{11}, K_{22} and K_{33} are the elastic constants associated with the well understood splay, twist and bend bulk deformations. Note that the volume integral of the saddle splay contribution can be reduced to a surface integral by using Gauss's theorem.

For planar anchoring, it is illuminating to represent the surface integral of the saddle splay contribution in terms of the principal curvatures: $F_{24} = -\frac{1}{2}(K_{24} + K_{22}) \int dS(k_1 n_1^2 + k_2 n_2^2)$, where k_1 and k_2 are the principal curvatures at a point on the surface, and n_1 and n_2 the director components along the corresponding directions. Specifically, for a cylinder (or half cylinder): $n_1 = n_\theta$ and $n_2 = n_z$; hence $k_1 = 1/R$ and $k_2 = 0$, where R is the radius of the cylinder. Hence, the saddle splay term drives the director to point along the n_θ direction. For a twist angle close to 180° the contribution of K_{24} to the free energy per unit length would be $-\pi K_{24}$.

Although it is favorable to twist at the edges, the twisting in the flat region costs energy. A simple scaling argument would estimate the energy cost per unit length in the flat region to be of the order $K_{22}\frac{w}{h}$ (~$10K_{22}$, for our geometry), where w is the width of the rectangle and h is the height as shown in Fig. 1(d). This can be rationalized by noting that the twist deformation is along the height of the capillary and hence the twist energy density scales as ~ $\frac{1}{h^2}$. Multiplying with the area of the capillary (w*h) we get the scaling of the twist deformation cost per unit length to be $K_{22}\frac{w}{h}$. Hence the deformation cost of having a doubly-twisted director (F_{DT}) in a rectangular capillary is: $F_{DT} \sim (10K_{22} - \pi K_{24})$. Previous experimental estimates of K_{24} for SSY are about the order $50K_{22}$ [12,13]. Clearly this implies, $F_{DT} < 0$, and the doubly-twisted director is preferable when compared to axial configuration ($F_{axial} = 0$). This explains the initial doubly twisted director configuration in the rectangular capillary.

3.2.3 Time evolution of the doubly-twisted configuration

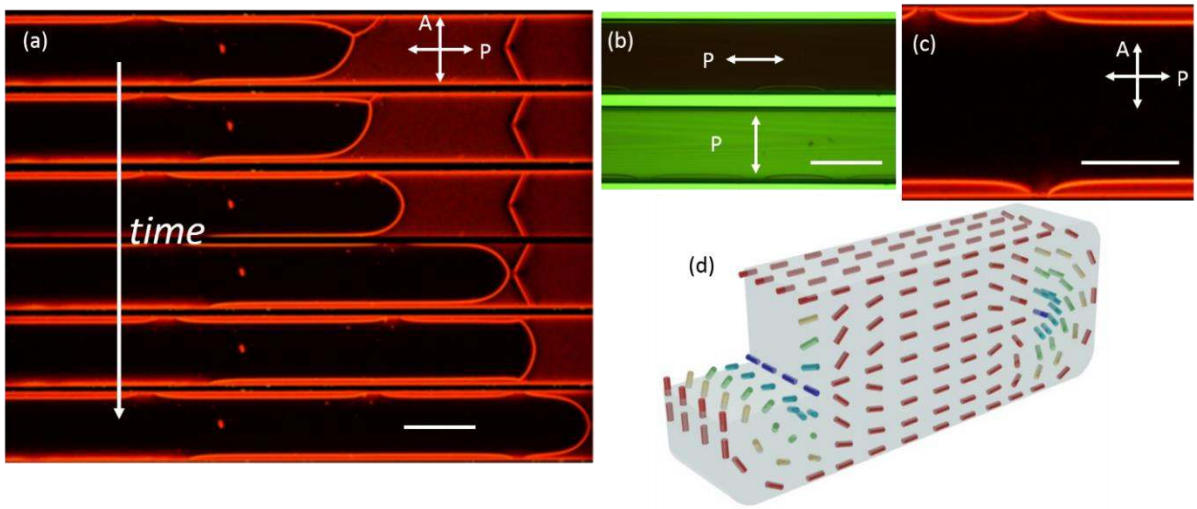

Figure 3.3 (a) Time evolution of the twisted configuration taken over by the monodomain like configuration. (b) Polarized light absorption of green light (551 nm) of the monodomian region. (c) Magnified crossed POM image of the monodomain region and twisted region and twisted region separated by the half disclination lines. Scale bar is 200 µm in (a) (b), and 100 µm in (c)

In a few hours the doubly-twisted director configuration evolves to a configuration that forms a monodomain in the flat regions of the capillary but remains twisted at the edges. A typical transition from metastable doubly twisted configuration to a monodomain like configuration is shown as the time-lapsed images in Fig. 3.3 (a). The orientation of the director in the monodomain region can be clearly discerned from the polarized absorption images using monochromatic light (551±4 nm) as shown in Fig 3.3(b). When the polarizer is along the long axis of the capillary, the image is dark indicating complete absorption of the incident light. In contrast, there is a strong transmission when the polarizer is along the short axis of the capillary. SSY has a broad absorption band around 400~530 nm, resulting from N=N and N-H bonds in the molecular plane [39]. Therefore, the director, which is perpendicular to the molecular plane, is along the short axis of the rectangular capillary. The director at the edges is still twisted and a half strength disclination line separates it from the monodomain region. The two regions separated by the disclination line are clearly

observed in the magnified image of Fig. 3 (c). Fig. 3(d) is the schematic of the director configuration of monodomain in center and twist near the edges.

For the new monodomain configuration there is no energy cost in the flat region. However, there is an added penalty of having two half-strength disclination lines [40,41]. The energy cost of the disclination core per unit length is of the order of $\pi K m^2$ [2,42,43], where m=1/2 is the strength of the line. As twist is the dominant deformation around the core, the energy cost of the core of the two lines is $\pi \frac{K_{22}}{2}$. Clearly, the cost of having two disclination lines is an order of magnitude lower than doubly twisting in the flat region (~$10K_{22}$). The monodomain like configuration is stable for weeks and is likely the ground state for SSY in rectangular capillaries.

3.3 Director configuration in square capillaries

3.3.1 Optical microscopy observations and scaling arguments to explain the observed structure

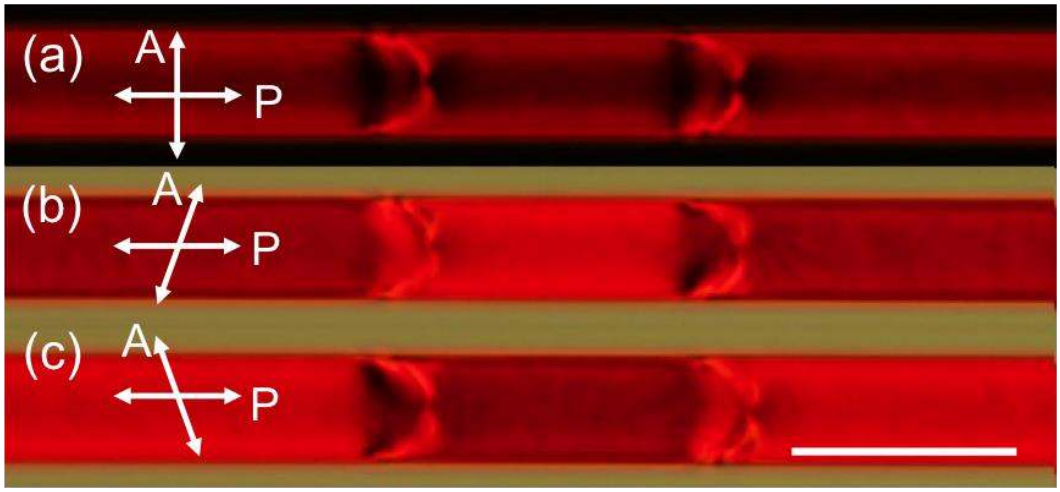

Figure 3.4 Crossed (a) and uncrossed (b)(c) polarized microscopic images of SSY with opposite twist domains in a square capillary. Scale bar is 100 µm.

In order to further confirm our theoretical analysis, we perform the same experiments with square capillaries with widths of 50 μm and 100 μm for comparison. From the cross-polarizers image in Fig 3.4 (a) and the uncross-polarizers images in Fig 3.4 (b) and (c), we can draw the same conclusion that the director of SSY liquid crystal is twisted in the square capillary as we did for the rectangular capillary. However, the doubly-twisted configuration in both 50 μm and 100 μm square capillaries keeps for months if the capillary is sealed well, and never changes to a monodomain like configuration as it does in a rectangular capillary. The difference can be well explained by our previous scaling arguments. The total free energy cost is: $F_{DT} \sim (K_{22}\frac{w}{h} - \pi K_{24})$ for a doubly-twisted configuration; and $F_{Mono} \sim (\pi\frac{K_{22}}{2} - \pi K_{24})$ for a monodomain like configuration in a rectangular capillary. For a square capillary, the aspect ratio $\frac{w}{h}$ is 1, causing that F_{DT} is smaller than F_{Mono}. Therefore, a doubly-twisted configuration is more favorable to SSY liquid crystal confined in a square capillary. One can also have a better estimation of the core energy cost of the half-strength disclination line, by making a series of rectangular capillaries of different aspect ratios and checking their ground state configurations.

3.4 **Conclusion**

We observed a spontaneous double twist structure of SSY lyotropic liquid crystal in both rectangular and square capillaries. The twist structure in a flat rectangular capillary eventually evolves to a well-aligned planar mono domain, which can be exploited to measure order parameters and viscoelastic constants of LCLCs. We elucidate the key role of the saddle-splay elastic constant on the formation of the double twist structure in a rectangular/square capillary, where curvature only exists at the corners. With a simple

scaling argument, we explain the evolution of the mono-domain like configuration from the initially double twist configuration, and the different ground states of SSY under rectangular and square confinement.

CHAPTER 4. INSIGHTS INTO THE AGGREGATION BEHAVIOR OF LYOTROPIC CHROMONIC LIQUID CRYSTALS USING CONFINEMENT EXPERIMENTS

In the previous chapters, we described experiments pertaining to unusual director configurations observed when LCLCs where confined to several geometries. One of the observed configurations namely that of a mondomain is particular relevance in performing fundamental studies to determine various physical characteristics of LCLCs. In this chapter we exploit mono-domains to quantify the order parameter of LCLCs using Raman scattering experiments and answer some fundamental questions pertaining to aggregation of LCLCs. We also use optical observations on LCLC tactoids to corroborate the conclusions of the order parameter experiments.

4.1 Introduction

Perhaps the most fundamental question that can be asked when studying liquid crystals, is regarding the orientational order in the system. Quantifying the orientational order is helpful in estimation of several other physical properties of liquid crystals like the elastic constants[2]. In the context of LCLCs, the question of the order in the nematic phase involves rich physics as the aggregate length and packing are a function of both temperature and concentration. We seek to delineate the role of concentration and temperature in influencing the aggregation behavior and in turn the order of LCLCs.

Raman scattering experiments were used to study the thermal evolution of the order parameters for a range of concentrations. Of particular relevance were the order parameters

measured close to the nematic-biphasic transition of LCLCs. Remarkably, the measured order parameters at T_{NB} (T_{NB} is the nematic-biphasic transition temperature) are independent of concentration. We provide a simple model incorporating the volume fraction and average aggregate length to help understand the nematic-biphasic transition for LCLCs. These observations bring to light the rich physics pertaining to the nematic-biphasic transition of LCLCs [44].

Further, we present experimental observations on the textures of tactoids as a function of concentration at the same reduced temperature. We show that the director configurations in the confined tactoids can be exploited as an optical guide to delineate the role played by concentration and temperature in the aggregation of LCLCs. We explain the changes to the director configurations by appealing to the scaling of the elastic constants as a function of the aggregate lengths. The observations on tactoids corroborate the findings from Raman experiments.

4.2 Measurement of order parameters as a function of temperature and concentration

4.2.1 Polarized Raman scattering experiments:

We studied the degree of orientational order of SSY in nematic phase using polarized Raman scattering. Polarized Raman intensities are measured in two conditions, $I_{//}$ and $I_{\perp}$, which represent the scattered intensities when the polarizer and analyzer are parallel and crossed, respectively. Fig 4.1 (a) shows a typical angular spectrum of Raman intensity for SSY in the rectangular capillary. As we can see $I_{//}$ has a maximum when the polarizer and analyzer are parallel to the long axis of the capillary. This again confirms that

the molecular plane is along the long axis of the capillary, and hence the director aligns normal to the long axis. We employ a Lorentzian fit to the 1596 cm^{-1} peak that corresponds to the aromatic ring stretching. Peak heights as function of angular position of the director is plotted in Fig. 4.1 (b). As expected for a monodomain, $I_{//}$ and $I_{\perp}$ have 2-fold and 4-fold symmetry, respectively. The depolarization ratio $I_{\perp}/I_{//}(\theta)$ is consequently obtained and fitted using the following equation [45,46],

$$R(\theta) = \frac{(r-1)^2\{56+40\langle P_2\rangle+(9-105\cos 4\theta)\langle P_4\rangle\}}{56(8r^2+4r+3)-40(4r^2-r-3)(1+3\cos 2\theta)\langle P_2\rangle+3(r-1)^2(9+20\cos 2\theta+35\cos 4\theta)\langle P_4\rangle} \quad (4.1)$$

Where, $\langle P_2\rangle$ and $\langle P_4\rangle$ are the 2nd and 4th moments of the orientational distribution function, r is the ratio of differential polarizability. Measurements are performed for concentrations ranging from 0.95M to 1.15M.

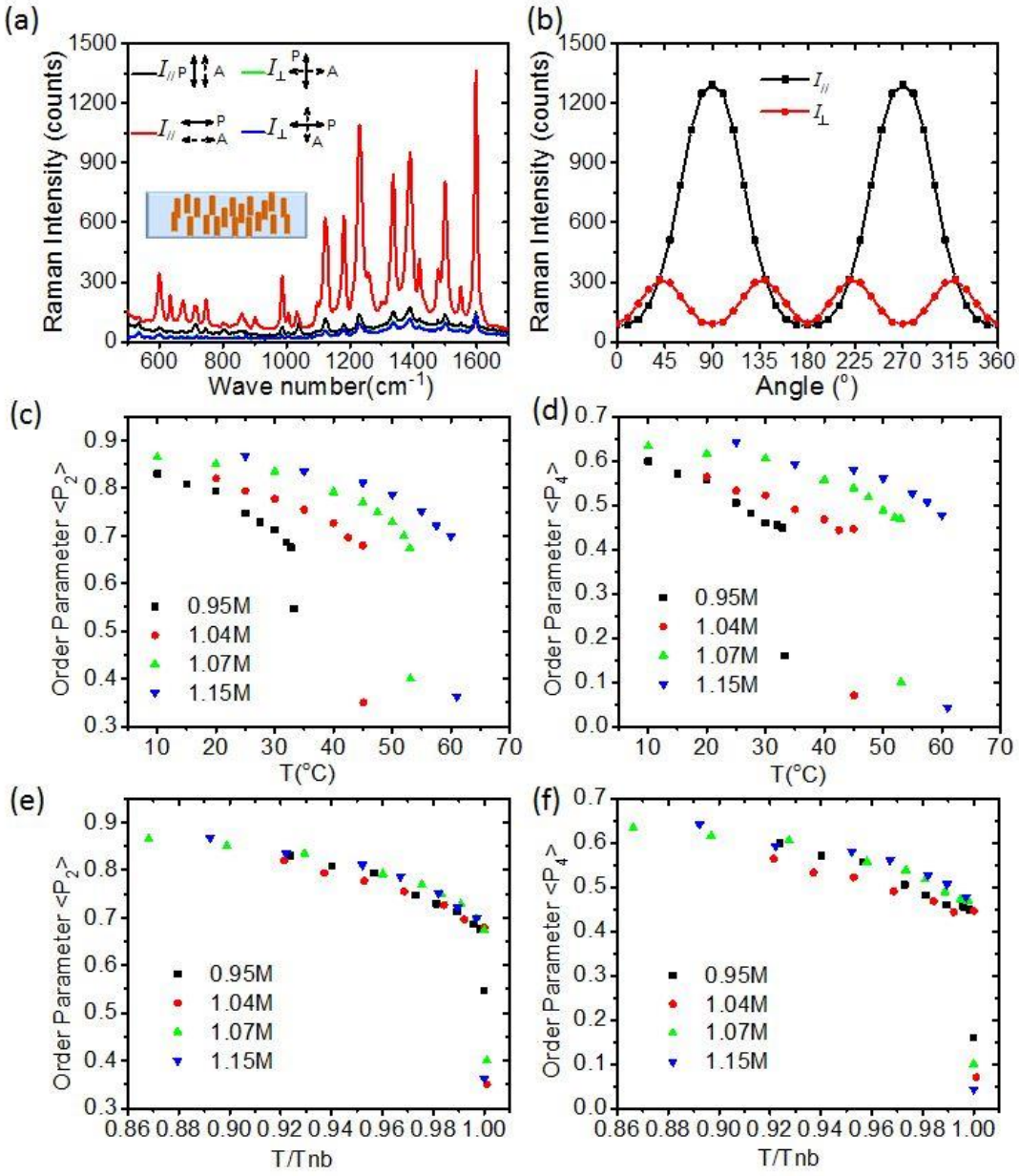

Figure 4.1 (a) Polarized Raman spectra of SSY at 0o and 90o (b) Raman intensities of 1596 cm-1 peak measured as a function of the capillary orientation (c) (d) P_2 and P_4 as a function of temperature (e) (f) P_2 and P_4 plotted against their reduced temperatures for different concentrations

The variation of the $\langle P_2 \rangle$ and $\langle P_4 \rangle$ as function of temperature and concentration are shown in Figure 4.1 (c) and (d). Order parameters for SSY increase with concentration at a given temperature. This is a unique property of LCLCs. Although the quantitative

values of $<P_2>$ and $<P_4>$ as a function of the temperature and concentration are informative, we can gain more physical insight by normalizing the temperature axis with nematic- biphasic transition temparature T_{NB}. This can clearly help in discerning and separating the roles played by concentration and temperature. Figure 4.1 e and 4.1 f are the plots of the order parameters as a function of the reduced temperature for different concentrations. It is evident from these plots that $<P_2>$ and $<P_4>$ are the same for every concentration at $T = T_{NB}$.. Further, the $<P_2>$ and $<P_4>$ dependence on the reduced temperature T/T_{NB} is independent of concentration for SSY. Thus, the only role played by concentration is to change the T_{NB}.

4.2.2 Simple model to explain the order parameter data

To explain the concentration independence of order parameters, we start with Onsager's idea that the two key factors determining the orientational order are: volume fraction φ and aspect ratio L/D 47. In our experiment, φ can be calculated from the SSY concentration using $\varphi = cM/(cM + \rho)$ [39,48], where $M = 452.36g/mol$ is the molar mass of SSY molecular, c is the concentration and $\rho = 1.4g/cm^3$ is the density of SSY aggregates [39]. The aspect ratio L/D can be determined by estimating the length L of the SSY aggregates. The diameter D, which is about the size of a SSY molecule, is the same for all the aggregates [39,49].

We use a simple model of one dimensional self-assembling units [50] to estimate the length distribution of the aggregates. The relative volume fraction X_N of aggregates containing N molecules is, $X_N = N(X_1 e^{\alpha/k_B T})^N e^{-\alpha/k_B T}$, where $X_1 = \frac{(1+2\varphi e^{\alpha/k_B T}) - \sqrt{1+4\varphi e^{\alpha/k_B T}}}{2\varphi e^{2\alpha/k_B T}}$ is the relative volume fraction of individual molecules [39,51], k_B

is the Boltzmann constant, T is the absolute temperature, and α is the inter-molecular attraction energy. The model assumes that the aggregation process is isodesmic. A commonly accepted value of α is around $7.25\ k_BT$, as estimated from several experiments [14,39,48,52] and molecular dynamic simulations [53]. The model incorporates the variation of aggregate size distribution X_N with both temperature and concentration.

Using this model, we calculate the size distribution at T_{NB} for different concentrations as shown in Fig. 4.2 (a). We find that samples of higher concentration have shorter average aggregate length at T_{NB}. Further from Fig. 4.2 (b), which is a plot of the relative number of aggregates X_N/N with different length, we learn that there are more aggregates in a sample of higher concentration at T_{NB}. Although non-intuitive, these two results are very insightful in trying to gain physical understanding about LCLCs. For hard-rods the aspect ratio L/D is a constant and determines the critical volume fraction. However, in a LCLC system, the aspect ratio depends both on concentration and temperature. In spite of this complication, we provide a simple picture by examining the product $\varphi \cdot < N >$ for all the samples. As we can see from the table, at T_{NB} the product of $\varphi \cdot < N >$ is essentially the same for all samples.

Table 4.1 Product of φ·<N> for different concentrations

C(M)	0.95	1.04	1.07	1.15
φ	0.235	0.251	0.257	0.271
<N>	14.6	13.3	12.4	11.8
$\varphi \cdot < N >$	3.42	3.34	3.19	3.20

Even though LCLCs are composed of semi-flexible aggregates, we find that the hard-rod theory of Onsager's can qualitatively explain our experimental results. According to Onsager's theory, the order parameter is expressed as: $S \approx 1 - 3/\alpha$, where $\alpha \sim \frac{4}{\pi}(\varphi\frac{L}{D})^2 - \frac{45}{8} + o((\varphi\frac{L}{D})^{-2})$. From the expressions, it is clear that the order parameter can be fully determined by the product of φ and L/D. Our experiments quite surprisingly agree reasonably well with these predictions. Not only is the order parameter a constant at T_{NB} for all concentrations, but we have also shown using a simple model that $\varphi \cdot < L > /D$ is a constant at T_{NB}.

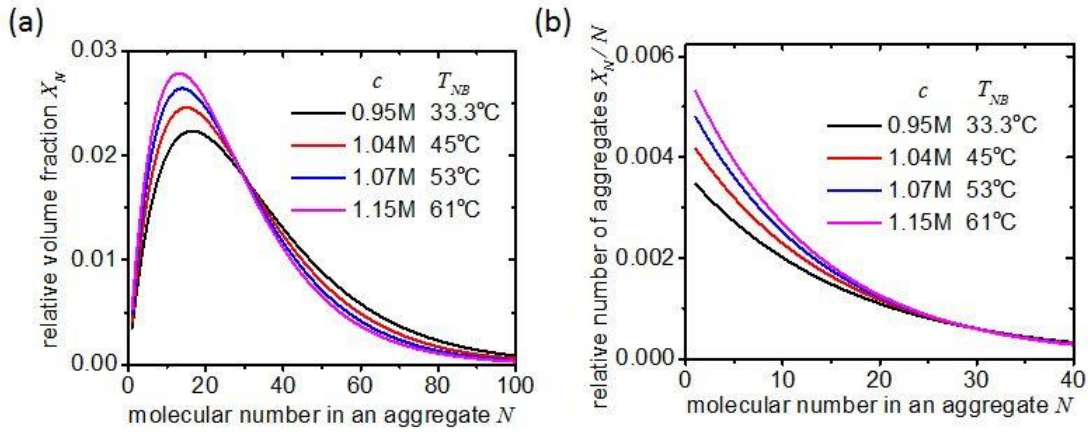

Figure 4.2 (a) Relative volume fraction of aggregates with different lengths at T_{NB} (b) Relative number of aggregates as a function of aggregate length for the four concentrations at T_{NB}

For a given concentration, entropy always favors more aggregates, while the π-π interaction between the molecules favors fewer but longer aggregates. The system equilibrates through the competition between the entropic and enthalpic contributions. As the temperature increases at a fixed concentration, the aggregate length decreases, and the product $\varphi \cdot < N >$ decreases. The system becomes biphasic when the value of $\varphi \cdot < N >$ is

smaller than 3.2. The transition temperature T_{NB} is determined by the critical length for a given concentration. Hence higher the initial concentration corresponds to higher T_{NB}.

4.3 Experiments on LCLC tactoids

We provide further evidence to substantiate the claims based on the Raman experiments by observing the textures of tactoids of SSY for different concentrations. When an isotropic phase of a lyotropic system undergoes a phase transition to an ordered nematic phase, the pathway is usually mediated through spindle shaped droplets called tactoids. Observation and analysis of tactoids has been an integral part of the investigations on liquid crystals, including some of the earliest experiments which motivated the seminal theory of Onsager [16,54]. In addition to shedding light on the nature of the isotropic- nematic phase transition, tactoids also provide a natural setting to study nematics under confinement [24,35,37,55,56]. Hence, they provide an attractive setting as a testbed for fundamental research as well as being relevant to technological applications. This has driven the experimental investigation of tactoids in a host of materials, including dispersions of viruses [54,57], proteins [58], inorganic platelets [59] and lyotropic chromonic liquid crystals (LCLCs) [24,60].

The director configuration in the tactoids is dictated by the individual contribution of the elastic constants, splay (K_{11}), twist (K_{22}) and bend (K_{33}) to the Frank free energy [24,35,37,55,61,62] . Historically, tactoids of lyotropic nematic liquid crystals have been found to have an elongated shape and adopt a bipolar configuration with the director following the meridional lines [54,58,59,62]. Only recently has a twisted-bipolar director configuration been experimentally realized for a LCLC system when it was crowded with polyethylene glycol (PEG) [24]. Twisted bipolar tactoids of cellulose nanocrystals have also been demonstrated

recently [63]. The emergence of chirality in achiral liquid crystals has fueled the curiosity of scientists ever since their discovery [64-67]. There have been a host of technological applications which take advantage of chiral configurations of confined liquid crystals [68,69]. In this section we exploit the emergence of a new chiral tactoidal structure to address fundamental questions pertaining to the aggregation behavior and the physics behind the nematic-biphasic transition of LCLCs.

LCLCs have gained increasing attention in the last two decades as an interesting yet poorly understood class of liquid crystals [51,70-74]. They are made up of plank-like molecules with a polyaromatic core and polar peripheral groups [14,75]. The π–π interactions result in the stacking of the constituent molecules[15]. The aggregation process is believed to be isodesmic; that is, addition or removal of molecules to a column is always associated with the same energy cost [39,76-79]. In addition to applications of technological relevance [80-85], LCLCs provide a fertile playground for fundamental studies. Of particular interest are studies dealing with confinement of these materials. The twist elastic constant for LCLCs is much lower than splay, bend and saddle-splay elastic constants [18,19]. This results in the emergence of spontaneous twist when LCLCs are confined to different geometries. Twisted structures have been reported previously in disodium cromoglycate (DSCG) tactoids [24], Sunset Yellow FCF (SSY) droplets [25] and for LCLCs confined to cylinders [12,13]. Another interesting aspect of LCLCs is that the length distribution of the constituent units is polydisperse and determined both by temperature and concentration [14,19,48]. A consequence of the polydisperse size distribution of LCLCs is a broad biphasic regime where the nematic and isotropic phases coexist [48]. However, there are several fundamental

questions pertaining to LCLCs including their aggregation behavior, elasticity and anchoring that need to be rigorously addressed [74].

We exploit tactoids for studying the effect of confinement on LCLCs for a range of temperatures and concentrations, as well as to uncover the underlying physics pertaining to the aggregation and phase transitional behavior of LCLCs [24]. We show that the director configurations in the confined tactoids can be exploited as an optical guide to delineate the role played by concentration and temperature in the aggregation of LCLCs. For high concentrations we observe the well understood bipolar tactoids. However, upon lowering the concentration we observe a mirror-symmetry breaking transition and the emergence of twisted-bipolar tactoids. We find that, for the same reduced temperature, T/T_{BI} (T_{BI} is the biphasic-isotropic transition temperature for the given concentration), the twist angle of the twisted-bipolar tactoids increases as the concentration is lowered. Concurrently, we observe a new director configuration, where the director is oriented concentrically and is free of singular defects. We make a case for this configuration being the escaped-concentric configuration while clearly distinguishing it from twisted-bipolar tactoids. The surprising finding is rationalized by using a simple model to calculate the average length and length distribution of the aggregates. We conclude that, at the same reduced temperature, lower concentrations on average have longer aggregates. Consequently the splay deformation in the bipolar droplets becomes prohibitive with increasing length of the aggregate [21].

4.3.1 Polarized optical microscopy:

Historically, tactoids of lyotropic liquid crystals have always conformed to the bipolar director configuration [36,54,58,59]. In this configuration the director follows the

meridional lines with the surface defects (or boojums) being located at the poles. This can be appreciated from the image in Figure 1a, which is an image of a bipolar tactoid under crossed polarizers. Note that the central part of the tactoid is completely dark. This is a characteristic feature of bipolar tactoids in the absence of twist. The sample corresponding to Figure 4.3a is 1.1M SSY observed at 59.5ºC (T/T_{BI} = 0.99). When the concentration is lowered to 1.0M (observation temperature 42.8ºC, T/T_{BI} = 0.99) we see that the bipolar tactoids develop a twist. This can be inferred via the transmitted light intensity in the central region of the tactoids in Figure 4.3b. The twisted director configuration acts as a waveguide for polarized light and results in a transmitted intensity even under crossed polarizers. The inset of Figure 4.3b shows the extinction of transmitted light when the polarizers are uncrossed, which serves as additional confirmation of the twisted structure. As the concentration is lowered below to 0.9M, we observe the emergence of a tactoidal configuration which exhibits a completely different texture. This new director configuration has a radial symmetry unlike bipolar or twisted-bipolar tactoids. The new configuration can be observed clearly in Figure 4.3c. The concentration of the corresponding sample is 0.9M and the observation temperature is 29.6ºC (T/T_{BI} = 0.99).

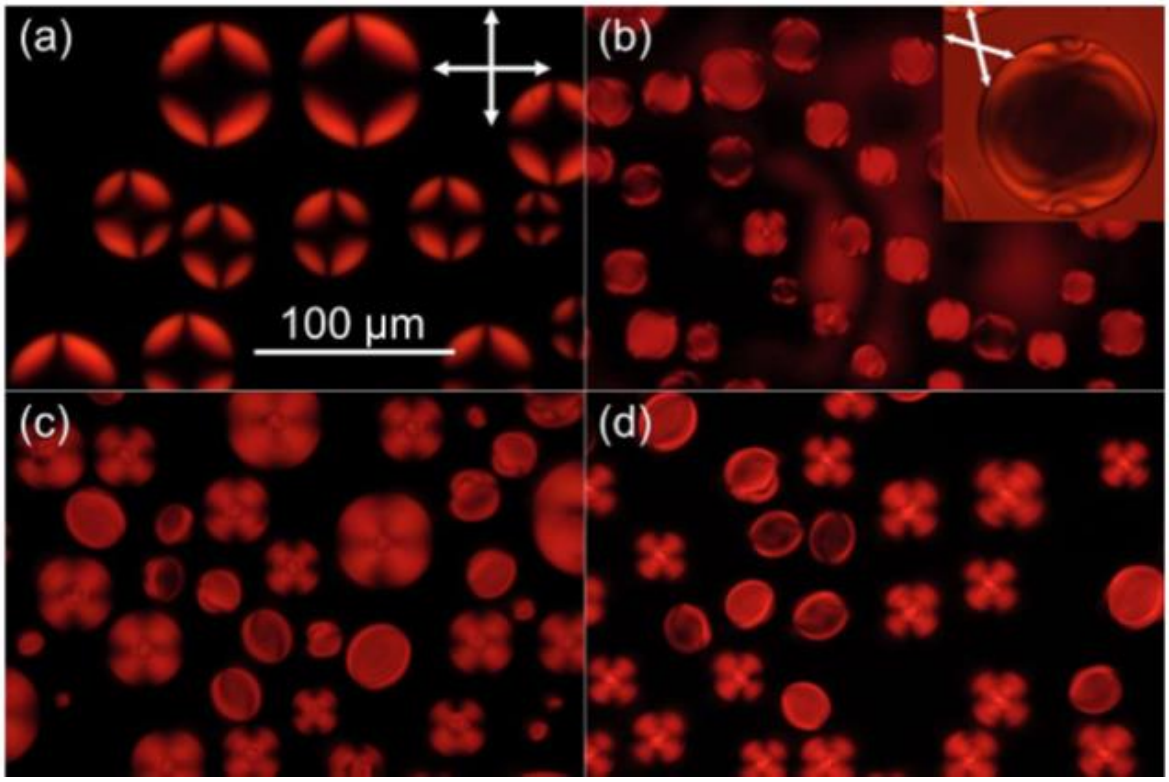

Figure 4.3 Polarized microscopic images of SSY tactoids at different concentrations (a) 1.1M, bipolar; (b) 1.0M, twisted-bipolar tactoids and a small fraction of tactoids with the new director configuration; (c) 0.9M, increased fraction of tactoids with the new director configuration. The inset in (b) shows the extinction in the center of a twist-bipolar tactoid when polarizers are uncrossed with monochromatic illumination (589nm). (d) polarized microscopic image of 1.0 M SSY tactoids with 2wt% PEG . The scale bar for all the images is 100 µm

In order to understand the physics behind the phenomenology pertaining to the configurational transformations in the tactoids, we first quantify the concentration dependence of the twist angle of the twisted-bipolar tactoids at the same reduced temperature, using wave-guiding experiments [25,86]. Where, the twist angle is defined as the angle the director on the surface of the tactoid makes with the axis of symmetry [25]. We observe that, at the same reduced temperature (T/T_{BI}), lower concentrations have a larger twist angle. Starting with purely bipolar tactoids (twist angle =0^o) the twist angle increases to about 135^o for a 0.8M sample. The data for all the concentrations is plotted in Figure

4.4a. It has been shown previously in the context of LCLC droplets, that, the equilibrium twist angle of twisted-bipolar droplets is determined by the balance of offsetting the energetically costly splay deformation at the expense of twist and bend deformations [25]. Their results show that a large fraction of the elastic deformation cost in bipolar and twisted-bipolar droplets is associated with the splay deformation surrounding the surface defects [25]. We perform similar numerical calculations, but by fixing the ratio of bend/twist while allowing the value of splay elastic constant to vary. This is shown in Figure 4.4b. The plot verifies the prediction that increasing cost of splay results in an increasing twist-angle of the twisted-bipolar tactoids. The twist angle data and the numerical calculations suggest that, for a given reduced temperature, the relative cost of splay (K_{11}/K_{33} and K_{11}/K_{22}) increases as the concentration is lowered.

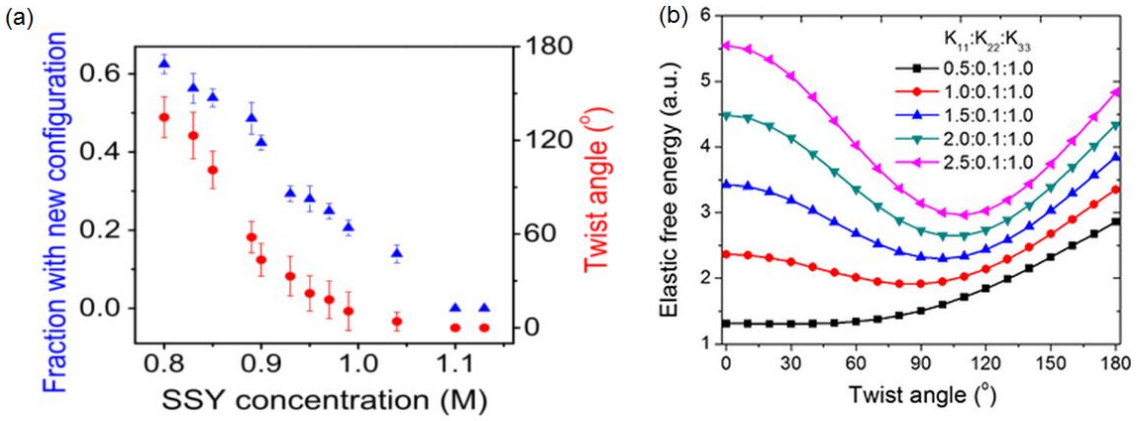

Figure 4.4 a) Twist angle of twisted bipolar tactoids and number fraction of the new director configuration as a function of temperature. b) Free energy cost of twisted-bipolar tactoids as a function of the different relative cost of splay

The elastic constants associated with the bulk deformations of a liquid crystal whose constituents are semi-flexible aggregates have contrasting scaling with the aggregate length, *L*. The splay elastic constant, as was alluded by Meyer, scales linearly

with the aggregate length ($K_{11} \sim \varphi L$) [19,21]. In contrast, the bend elastic constant for semiflexible aggregates is free to conform to the director orientation and hence is only dictated by the persistence length, λ_p, of the aggregates ($K_{33} \sim \varphi \lambda_p$). The twist elastic constant is also only a function of the persistence length and scales as $K_{22} \sim (\varphi \lambda_p)^{\frac{1}{3}}$ [22]. Persistence length is a molecular property which is a weak function of temperature and concentration [87]. On the other hand the aggregate length L is quite sensitive to changes in temperature and concentration [39]. Naturally, longer aggregates result in higher relative cost of splay. From the scaling of the elastic constants and the trend in the twist angle of twisted-bipolar tactoids, it is reasonable to deduce that, at the same reduced temperature lower concentrations have longer aggregates.

We also gather from Figure 4.3a to 4.3c that the fraction of tactoids with the new director configuration increases as the concentration is lowered. This is also quantified in Figure 4.4a. We postulate that this phenomenon is also a consequence of the relative increase in the splay cost as the concentration is lowered. We test this idea by increasing the cost of splay deformation of LCLCs while keeping the relative cost of bend and twist mostly unchanged. We achieve this with the addition of a small amount of polyethylene glycol (PEG) to SSY solutions. PEG is a widely used condensing agent. The use of PEG in influencing the aggregation behavior of LCLCs is well documented [24,88]. PEG remains in the isotropic part of the solution and exerts osmotic pressure on the nematic region resulting in the elongation of the aggregates. In essence, addition of PEG to a sample results in the increase of aggregate length consequently resulting in the increase of splay which scales linearly with aggregate length. Twist and bend on the other hand only scale with the persistence length and hence remain mostly unchanged.

Figure 4.3d is a cross-polarized image of a 1.0 M sample 0.5 wt% PEG. As compared to a 1.0M PEG free sample, which is Figure 4.3b, we see that Figure 4.3d clearly has a significantly higher fraction of tactoids adopting an escaped-concentric configuration. Not surprisingly, the twist angle of the twisted-bipolar tactoids also increases upon the addition of PEG. The measured twist angle of the twisted-bipolar tactoids in Figure 4.3b and 4.3d are about 18^{o} and 105^{o} respectively. We tabulate the fraction of tactoids adopting the new director configuration upon the addition of PEG for different concentrations in Table 4.2 below:

Table 4.2 Fraction of tactoids with new configuration as a function of PEG weight percent

SSY Concentration	0.90 M	1.00 M	1.04 M	1.13 M
Fraction with c(PEG) = 0 wt%	0.43	0.23	0.15	0.06
Fraction with c(PEG) = 0.5 wt%	0.53	0.43	0.32	0.26
Fraction with c(PEG) = 2 wt%	0.72	0.71	0.68	0.67

The trend is consistent for all concentrations and is in keeping with the idea that longer aggregates lead to greater fraction of tactoids with the new director configuration. We note that while PEG also increases the concentration of SSY aggregates [88], the scaling of both bend and splay is linear in concentration. Hence, the phenomenon observed upon the addition of PEG is largely due to changes to the aggregate lengths.

4.3.2 Dichroism experiments:

After establishing the phenomenology relating to the tactoidal configurational changes as a function of concentration, we shed more light on the nature of the new director

configuration that is prominent as the concentration is lowered. For this purpose, we perform linear dichroism studies on these droplets. The radial symmetry of the texture under crossed polarizers indicates that the director configuration is oriented in either a radial or a concentric fashion with a defect/escaped core at the center of symmetry. Comparing the regions of light extinction and light transmission in Figure 4.5b and 4.5c, we can rule out the possibility of a radial configuration. This can be ascertained by observing the intensity at the periphery of the droplet. In both instances the dark regions close to the periphery of the droplet, where the light is extinguished, are along the polarizer. This is contrary to the expectation if the droplet structure was radial. The molecular plane of sunset yellow molecules is perpendicular to the director orientation [38]. Hence, in a radial droplet, the extinction at the periphery should be perpendicular to the polarizer direction. The dichroism data suggests that the director is oriented concentrically as opposed to being radial. The simple concentric configuration involves an azimuthally oriented director with a line defect running through the center [25]. However, the formation of the line defect can be avoided through a twist deformation resulting in an escaped configuration. The swirl in the dichroism images is indicative of escape of the director configuration via a twist deformation.

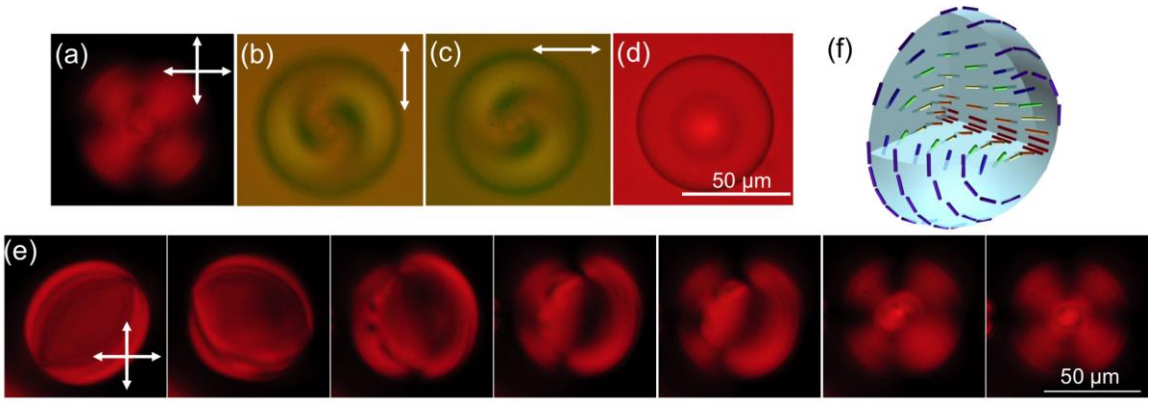

Figure 4.5 Dichroism, bright-field and transition images of SSY tactoids (a) under crossed polarizers. (b) under monochromatic illumination (551 nm) with vertical polarization. (c) under monochromatic illumination (551 nm) with horizontal polarization. (d) bright-field. (e) The transition from twisted bipolar to the new director configuration. The corresponding solution is 0.97M SSY doped with 0.5 wt% PEG. (f) A schematic of escaped-concentric configuration

4.3.3 Nature of defects in the new director configuration

Further information regarding the new configuration can be garnered by the bright-field images shown in Figure 4.5d. The surprising finding here is the lack of any indication of the presence of surface defects (boojums) which are a feature of the bipolar and twisted-bipolar configurations. Boojums when imaged under bright-field microscope can be readily distinguished due to the strong scattering off the defect core. The core of the defect has a different refractive index in comparison with the nematic phase. This results in strong scattering of light close to the defect. A combination of cross-polarized and bright-field images can be used to identify boojums. One such example is shown in Figure 4.6a and 4.6b, where scattering off the boojums of a twisted bipolar tactoid is readily obvious. However, in contrast, when the tactoids with the new configuration are observed under bright-filed microscopy, no scattering is apparent.

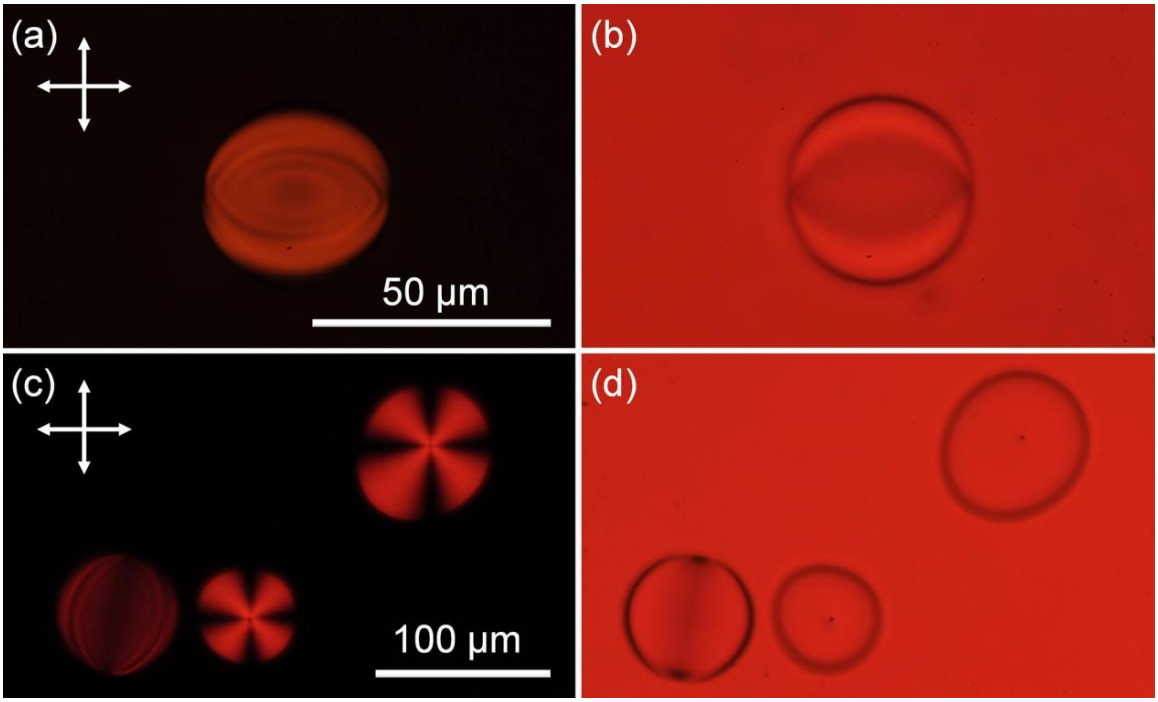

Figure 4.6 Microscopy images of tactoids. (a) and (b) are the polarized optical image and bright-field image of a twisted-bipolar tactoid. Two singular boojums can be clearly observed on each pole. (c) and (d) show the polarized optical image and bright-field image of tactoids in columnar phase. The tactoids exhibit concentric structure with a disclination line in the center. The singular line defects are clearly observed. The columnar tactoids are observed with 1.04 M SSY doped with 3 wt% PEG

The difference in the defect textures of the two configurations is made more apparent by examining the transition of a twisted-bipolar tactoid to one with the new configuration. This is shown in a sequence of images shown in Figure 4.5e. The sample under observation is 0.97M SSY solution with 0.5 wt% PEG. The tactoid initially has a twisted-bipolar configuration, and the boojums can be readily identified. As the configuration transitions, we see that the boojums are forced towards the center, while trying to maintain maximum separation via tracing a circular spiral (clockwise in this instance). Finally, from the last two snapshots we infer that the singular defects are replaced by a non-singular core of the new director configuration. Identifying the exact director configuration of the non-singular core is beyond our experimental capability. However, we

surmise that the reason for the preference of the non-singular core as opposed to the boojums is related to the cost of splay associated with the director field around the boojums, where most of the free energy cost of deformation is concentrated [25]. Finally, upon addition of 3wt% PEG to a 1.04 M SSY solution, the tactoids enter the columnar phase and adopt a concentric configuration. Scattering off the defects in the bright-field image for this case is again readily obvious. This is shown in Figure 4.6d.

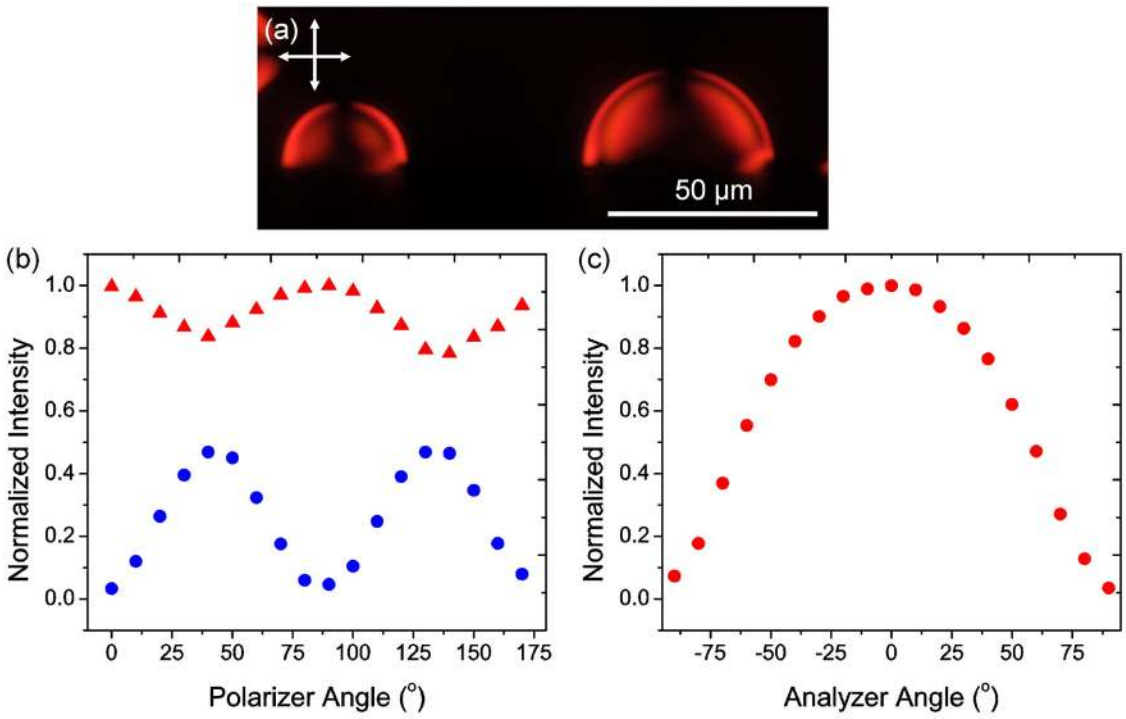

Figure 4.7 (a) Crossed polarized image of a 0.88M solution showing two escaped-concentric tactoids that have nucleated on the side wall of a square capillary (b) and (c) show the twist angle measurement of escaped-concentric tactoids. (b) The maximum (red triangles) and the minimum (blue circles) transmitted intensity at every polarizer angle when the analyzer is rotated through 180°. (c) The transmitted intensity at every analyzer angle when polarizer is fixed at horizontal position

At this juncture, having established the features of the new director configuration, we need to find the appropriate nomenclature to provide an identity for the configuration. Previous research on droplets of liquid crystals which possess a higher value of splay

elastic constant in comparison to twist and bend, has led to reports identifying the droplet structure as escaped-concentric [89]. However, distinguishing this configuration from a twisted-bipolar configuration has been fraught with controversy. In fact it was later argued that a 90° twisted-bipolar droplet is essentially the same as the suggested escaped-concentric structure [90]. Ironically, although the splay is largely concentrated close to the surface defect for twisted-bipolar configuration, the difference in the possible defect structures between the two configurations was never discussed in the context of minimizing the splay deformation [89]. We present observations that are consistent with the idea that the director trying to avoid the splay deformation, leads to the emergence, increasing number fraction and the arrangement near the defect of the new configuration. For these reasons, we find it is appropriate to call this new director configuration as escaped-concentric. Finally, we confirm that the twist angle of the escaped-concentric tactoids is indeed 90° by wave-guiding measurements on tactoids that happen to nucleate on the side wall of a square capillary. The data is presented in Figure 4.7. We hypothesize that the director avoids the formation of the boojums with a non-singular core which violates the anchoring in a small region by pointing axially. A schematic of the proposed escaped-concentric configuration is provided in Figure 4.5f. Far away from the defect/non-singular core the director arrangement in the escaped-concentric configuration is identical to a 90° twisted-bipolar tactoid. The important distinction however lies in the director arrangement near the defect.

4.4 **Conclusion**

Although LCLCs have been a subject of experimental curiosity for the past two decades, there are several unanswered questions pertaining to their phenomenology. In this chapter we use tactoids as a means to uncover rich physics pertaining to the nematic-

biphasic transition of LCLCs. In the process we also uncover several interesting phenomenology pertaining to tactoids, like breaking of achiral symmetry. In addition to being relevant to liquid crystal research the overarching themes in our work would be of interest to research in symmetry breaking phase transitions, chiral structures and colloidal physics among others.

Bipolar tactoids prevailed in our experiments when higher concentrations were observed optically. However, upon lowering concentration we observed a breaking of achiral symmetry and a predominance of twisted bipolar tactoids. On further reduction of concentration, the tactoids assume a surprising escaped-concentric director profile. An analysis of the aggregate length distribution at the same reduced temperature for different concentration reveals that lower concentrations on average have longer aggregates. The contrasting scaling of elastic constants with the aggregate length explains the experimental results qualitatively. The dramatic director configurational changes that we see are a direct result of the changes to aggregate size which can also be induced my crowding agents and other impurities like ions [24,48]. These reasons make the tactoidal droplets an extremely good candidate for sensor applications. The insights gained from optically observing tactoidal droplets were extended to understand the underlying physics of the nematic-biphasic transition. Order parameters $<P_2>$ and $<P_4>$ of SSY LCLC were measured close to the transition temperature and they were found to be independent of the concentration. We find that the product of volume fraction and the estimated average length of aggregates is almost a constant at T_{NB}. This provides an explanation for the invariance of the order parameter with concentration. The optical observation of tactoidal droplets and the order parameter measurements then lay the basis for the physical picture we put forward, which

corresponds to higher concentrations having shorter aggregates but a larger number of them, while, lower concentrations have longer but fewer aggregates at the transition temperature.

4.5 **Material and experimental details**

SSY was purchased from Sigma-Aldrich and TCI America with a purity of 90%. Polarized optical microscopy experiments were performed with a Leica DMRX microscope. Polarized Raman measurements were done using a Kaiser Raman Rxn system. Sample preparation: SSY was purchased from Sigma-Aldrich and TCI America with a purity of 90%. Further purification was carried out by dissolving it in deionized water and adding ethanol causing the SSY to precipitate. We then filtered the isolate and dried the powder in a vacuum oven. The purified SSY is then dissolved in deionized water to make SSY solutions. All rectangular glass capillaries were purchased from Vitrocom. Without further treatment, the capillaries were filled with isotropic SSY solutions by capillary action, and then placed on a glass slide. The ends were sealed with epoxy glue to prevent the water evaporation. The capillaries used for tactoidal experiments are 100 μm*1000μm. For Raman experiments the capillary dimensions are 20 μm* 200 μm**.** The dimension of the square capillary is 100 μm. The sample slide was placed on a Linkam T95-PE heat stage with a temperature control accuracy of 0.1^0C. The heat stage was mounted on the 360^0 rotation stage of the Leica DMRX microscope. The low magnification images were obtained with a 10x (NA=0.3) Leica objective and the high magnification images were obtained with a 100x (NA=1.4) Leica objective.

CHAPTER 5. SCALING OF SADDLE-SPLAY ELASTIC CONSTANT WITH THE ORDER PARAMETER

In this chapter, we provide experimental evidence towards an often-neglected theoretical prediction regarding the scaling of surface-like elastic constants. We study the bipolar to radial transition of liquid crystals confined to spherical droplets. Using the contribution of the individual elastic constants to the Frank free energy we conclude that the linear scaling of the saddle-splay elastic constant is likely to blame for the surprising transition in the spherical droplets when they are heated sufficiently close to the transition temperature.

5.1 Introduction

The order parameter for nematic liquid crystals is related to the orientational distribution of the molecules. The uniaxial order parameter S is an even function of the polar angle β, which is the angle between a given molecule and the director. Legendre polynomials provide the mathematical formalism for expressing S in terms of the polar angle β, which the molecules make with the director:

$$S = < \frac{3cos^2\beta - 1}{2} > \tag{5.1}$$

Where, < > denotes ensemble average.

It is customary to think of the bulk elastic constants associated with liquid crystals in terms of their quadratic scaling with order parameter as per the expectation of theoretical predictions [1,7]. This implies that the ratios of elastic constants do not change with the variation of temperature. For this reason, configurational transitions or changes to qualitative phenomenology are not expected when temperature and hence the order of the system is changed. However, another prediction of phenomenological models pertaining to the linear scaling of the surface-like elastic constants with order parameter has not been paid enough attention in an experimental sense [31]. In the recent years, the prominent role played by saddle-splay elastic constant in dictating the director configuration in confined geometries was demonstrated through clear experiments [9,12,13]. The prominent role played by saddle-splay in confined geometries in combination with the prediction of its linear scaling with order parameter gives rise to the possibility of the occurrence of interesting phenomenology when the order parameter of the system changes.

In this chapter we put the theoretical prediction pertaining to the scaling of saddle-splay elastic to an experimental test. A good approach to test this prediction would be comparing the director arrangement in an appropriate confinement close to the nematic-isotropic transition temperature and far away from it. The order parameter close to transition is quite small (S ~0.3) and gives rise to the possibility that the surface-like elastic constant that scale linearly might have a dominant role in comparison with the bulk elastic terms that have a quadratic scaling with order parameter. We show below that the use of spherical confinement of nematics is not only a convenient experimental choice but also one of the clearest ways to demonstrate the linear scaling of surface-like elastic constants.

5.2 Experiments of spherical droplets with planar anchoring conditions

5.2.1 Textural changes in the morphology of a bipolar droplet as a function of order parameter

There has been considerable interest in understanding the behavior of liquid crystals confined to micrometer sized droplets as they are promising candidates for opto-electronic applications and for use as sensors [25,34,68,69,91]. Liquid crystal drops are fundamentally relevant, as the coupling of geometry and topology with nematic order brings into play rich physics relating to transitions between thermodynamically stable defects [92,93]. Several studies have shown structural transformations of liquid crystals droplets as a function of external parameters like surface anchoring, electric and magnetic fields and even extremely small amounts of endotoxins [91,94,95].

We study liquid crystal emulsions dispersed in water/ polyvinyl alcohol (PVA). It is well known and widely reported that PVA imposes planar anchoring on liquid crystals [9,92,93]. The 5CB droplets surrounded by PVA adopt the expected bipolar configuration. The texture can be readily identified in Figure 5.1a where a bipolar drop is imaged with monochromatic light and crossed-polarizers. This is representative of the droplet morphology far from the transition temperature. The number of dark fringes observed in Figure 1a relates to the birefringence of the liquid crystal and the diameter of the droplet as $\Delta n * d = 2\pi m\lambda$, where m is number of fringes. As, the droplet is heated and consequently the order parameter (and birefringence) is reduced, we notice that the fringes observed in the experimental texture also decrease. This can be deduced in Figure 1b and 1c. This observation corresponds to the reduction of the birefringence with temperature. Finally, when the temperature is sufficiently close to the transition temperature (T/T_{NI} ~0.997) we first observe a metastable structure where a disclination ring can be clearly

discerned. This is shown in Figure 1d. The disclination ring quickly collapses to a radial hedgehog and a radial configuration can be clearly identified in Figure 1e.

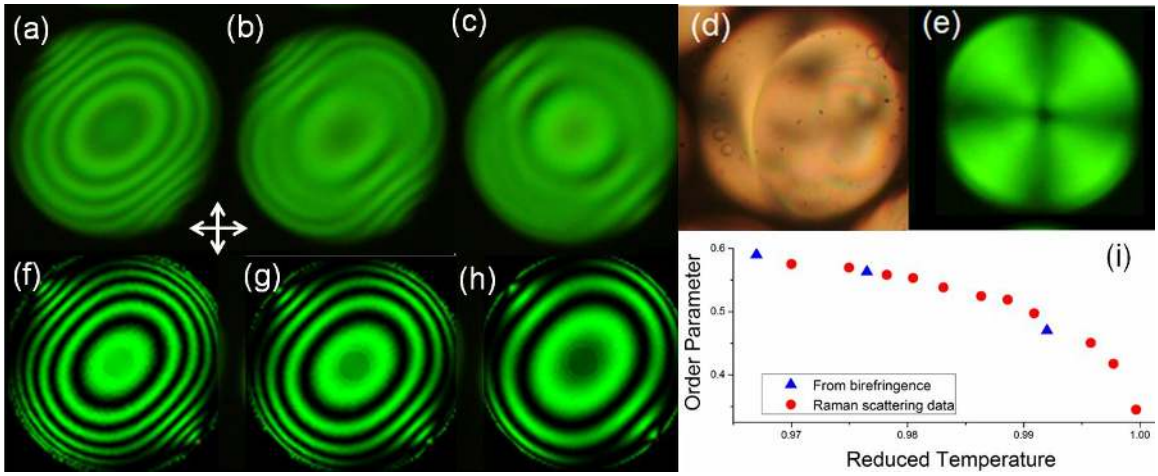

Figure 5.1 Thermal evolution of the droplet morphology a) Bipolar drop far from transition(T/T_{NI} ~0.97) b) and c) The dark fringes of the bipolar drop reduce as it is heated d) metastable configuration with disclination ring e) radial droplet at T/T_{NI} ~0.997 f) to h) are Jones calculus simulations that capture the experimental textures observed in a) to c); i) Order parameter data from Raman scattering experiments and from the values of birefringence used in the Jones calculus simulations

In order to understand the morphological evolution of the droplet configuration in a quantitative sense, we perform Jones calculus simulations which capture the experimental findings. Figure 1f to 1h are Jones calculus simulations of the droplet morphologies which replicate the experimental morphologies in Figure 1a to 1c in a quantitative sense by capturing the order of the fringes. The value of birefringence used for the simulations is correlated with the corresponding order parameter (Δn~S). We do this by noting that birefringence for 5CB can be quantified[2,96] using Haller's approximation as $\Delta n = \Delta n_o(1 - \frac{T}{T_{NI}})^{\beta}$. Δn_o is the birefringence at 0K and is obtained by extrapolating the experimental data using Haller's relation[96]. We use Δn_o reported in the literature to obtain order parameters from the values of the birefringence used in the simulations. The order

parameters so obtained are plotted along with the thermal evolution of the order parameters as measured from Raman scattering experiments in Figure 1i. We note that there is excellent agreement between the two sets of data and the changes to the bipolar morphology can be fully explained by the variation of the order parameter with temperature. However, the rationale for the surprising transition to a radial texture is less obvious. The transition from the bipolar to the radial configuration corresponds to an order parameter of S~ 0.4. We describe the pathway of the transition from the bipolar to the radial texture below.

5.2.2 Pathway of transition from bipolar to radial texture

Figure 5.2 shows the transformation stages of a bipolar drop as it is heated sufficiently close (S~0.4) to T_{NI}. A disclination ring nucleates from the initial bipolar configuration, the ring is then pushed to the edge where is collapses to a hedgehog, which then relaxes back to the center, to form a radial droplet. The steps described here are analogous to the droplet configurations reported in the literature when the anchoring conditions of the outer medium are varied [95]. However, in our case, the external conditions are kept constant and it is the interplay of the variation of elastic constants with temperature that brings about the transition.

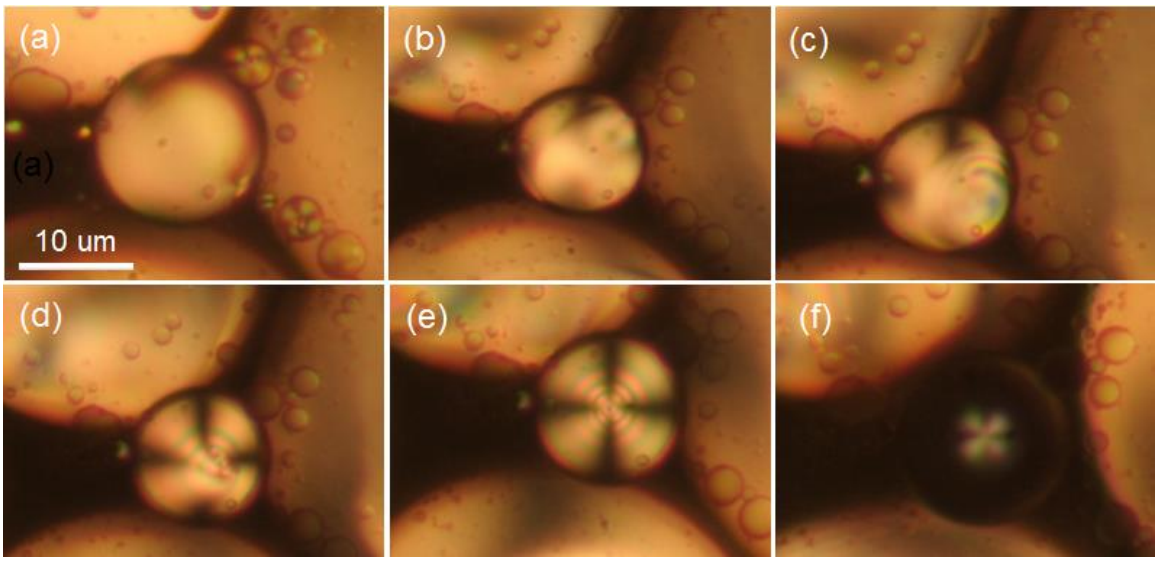

Figure 5.2 Transformation pathway of bipolar to radial structure when the droplet is heated close to transition. a) Bipolar droplet b) and c) formation of a disclination-ring at the periphery of the droplet d) and e) Saturn ring shrinks to a hedgehog and moves from the interface to the center of the droplet f) melting to the isotropic phase

The transition from bipolar to radial drop always occurs within 1°C from the transition temperature. To rule out any coincidental temperature induced changes in the anchoring conditions at around 35.5 °C which is transition temperature of 5CB, we perform the same experiment with another liquid crystal (E7) that has a much higher transition temperature than 5CB. We see the same transition from bipolar to radial configuration again within 1°C of the transition temperature (63.8 °C) ruling out any effects caused by changing anchoring conditions.

5.3 Free energy cost of deformation in bipolar and radial droplets

When confined to spherical drop the director adopts a configuration that minimizes the Frank free energy given by:

$$F = \frac{1}{2}\int dV[K_{11}(\nabla \cdot n)^2 + K_{22}(n \cdot \nabla \times n)^2 + K_{33}(n \times \nabla \times n)^2 - (K_{24} + K_{22})\nabla \cdot (n(\nabla . n) + n \times \nabla \times n)] + W sin^2(\theta - \theta_0) \quad (5.2)$$

Where, K_{11}, K_{22} and K_{33} are the familiar splay twist and bend elastic constants. The terms weighted by (K_{24} + K_{22}) is the saddle-splay contribution. *W* denotes the strength of the surface anchoring which forces the molecules at the surface to adopt degenerate planar anchoring.

We explain this remarkable transition from bipolar to radial configuration by considering the contribution of the saddle-splay elastic constant to the Frank free energy and its scaling behavior with respect to the order parameter. For the case of planar anchoring, the saddle-splay term tends to align the director along the direction of largest principal curvature. This can be better understood when the contribution of the saddle splay term to the free energy per unit length is written in the form: $F_{24} = -\frac{1}{2}(K_{24} + K_{22})\int dS(k_1 n_1^2 + k_2 n_2^2)$, where k_1 and k_2 are the principal curvatures at a point on the surface and n_1 and n_2 the director components along the corresponding directions. For the case of a spherical drop as the two principal curvatures are the same, the contribution of saddle splay term is a constant (-2(K_{24}+K_{22}) R) irrespective of whether the droplet is a bipolar droplet, twisted bipolar droplet or concentric. However, when we evaluate the contribution of the saddle splay term when the droplet adopts a radial configuration the contribution of saddle splay term to the free energy is (-4 (K_{24}+K_{22})R. The rationale behind the larger contribution of saddle-splay term in a radial drop can be reasoned by realizing that saddle-splay is a deformation of simultaneous splays and twists $-(k_{22} + k_{24})(s_1 s_2 + t_1 t_2)$. In a radial drop ($n_r = 1$) the contribution of the $s_1 s_2$ term is clearly the maximum.

However, for the case of the bipolar drop clearly the contribution of the $s_1 s_2$ term is smaller as the director has a n_θ component. The full expression for the deformation cost involved (assuming $K_{11} \sim K_{33}$) in a bipolar droplet and a radial droplet are given below:

$$F_{bp} = 5\pi K_{11} R - 2\pi(K_{24} + K_{22})R \tag{5.3}$$

$$F_r = 8\pi K_{11} R - 4\pi(K_{24} + K_{22})R + 2WR^2$$

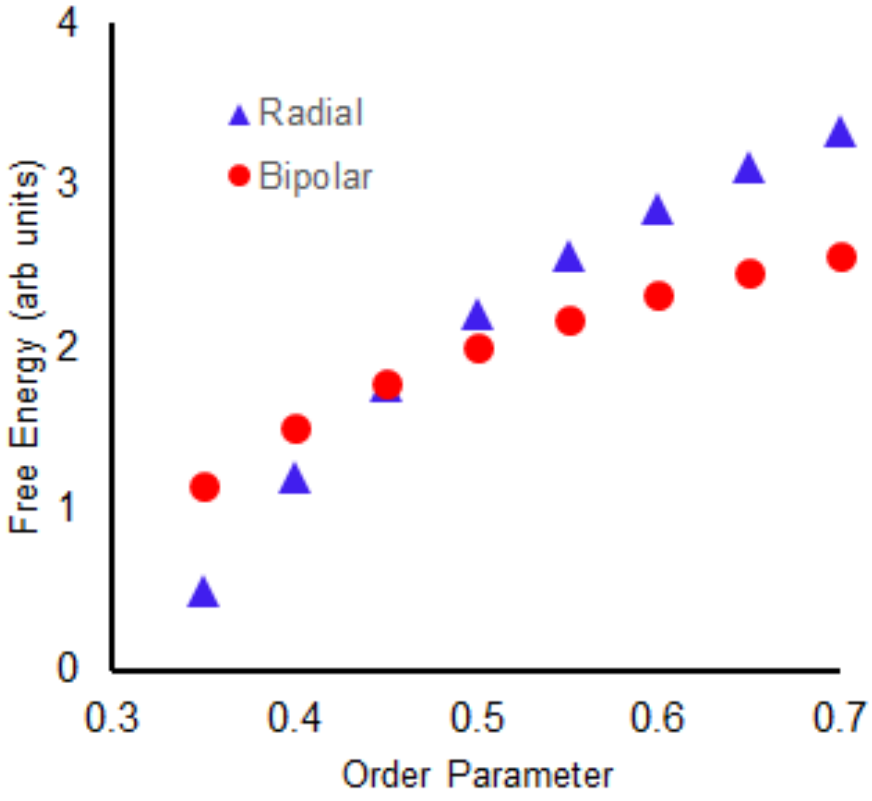

Figure 5.3 Free energy cost of deformation in bipolar and radial droplets as a function of the order parameter

Although the saddle splay contribution stabilizes the radial droplet more in comparison to a bipolar droplet, we still need to address the important question of why the transition depends on the order (temperature) of the system? We appeal to the prediction

of phenomenological theories that expect K_{24} to scale linearly with order parameter to explain these experimental results [31,32]. The scaling of the saddle-splay term is then in contrast with the bulk terms which scale with the order parameter in a quadratic fashion. The value of K_{24} has been experimentally measured to be around the value of K_{22} for 5CB[9,10]. These measurements and first principle calculations were performed far from the transition temperature (S~ 0.7). Closer to the transition temperature, where the order parameter is around 0.4, it is reasonable to expect the value of K_{24} ~ 2.5 K_{22} due to the linear scaling of K_{24} with S. This would then explain the driving force for the transition from bipolar to a radial droplet. Figure 5.3 is a plot of the energy cost of radial and bipolar configurations as a function of the order parameter. We approximate the normalized free energy cost of radial and bipolar droplets in terms of the order parameter as:

$$F_{BPnorm} = 5 - 2 * \frac{(S+S^2)}{2S^2} \qquad F_{Rnorm} = 4 * (2 - \frac{(S+S^2)}{2S^2}) + 0.2 \qquad (5.4)$$

The crossover in Figure 5.3 is in good agreement with the experimentally observed transition corresponding to S~0.4. Although the plot of the free energies in Figure 5.3 is in good agreement with the experiments, there is a caveat attached to the calculations. We note that in the free energy expressions for the radial droplets (equation 5.2), the anchoring term (W) has a quadratic (R^2) dependence ($F_W \sim WR^2$) with the system size while the elastic term has a linear dependence ($F_E \sim KR$). This implies that it is not possible to plot the comparison between the free energy cost of the two configurations in a manner that is independent of system size. Figure 5.3 was a plot for a droplet of size 10 microns. Naturally, we might expect the observed phenomena (S at which the transition occurs) to

be a dependent on the system size. Further work is needed to experimentally verify this prediction.

5.4 **Prediction of phenomenological theories**

Although there has not been a lot of experimental attention pertaining to the scaling of the saddle-splay elastic constant, the theoretical predictions were made quite a while ago. Following the usual lines of the Landua- deGennes treatment [31], a tensorial nematic order parameter can be introduced:

$$Q_{ij} = \frac{S}{2}(3n_i n_j - \delta_{ij})$$

Where n_i denotes the i*th* director field component and S is the uniaxial order parameter. With the tensorial order parameter defined, we can express the free energy with a general Landau- de Gennes type expansion:

$$\begin{aligned} F = {} & L^{(1)}Q_{ij,ij} + L_1^{(2)}Q_{jk,i}Q_{jk,i} + L_2^{(2)}Q_{ij,i}Q_{kj,k} + L_3^{(2)}Q_{jk,i}Q_{ik,j} + L_5^{(2)}Q_{ik,ij}Q_{jk} + L_6^{(2)}Q_{jk,ii}Q_{jk} \\ & + L_1^{(3)}Q_{ij}Q_{ij,k}\,Q_{kl,l} + L_2^{(3)}Q_{ij}Q_{ik,j}\,Q_{kl,l} + L_3^{(3)}Q_{ij}Q_{ik,k}\,Q_{jl,l} + L_1^{(3)}Q_{ij}Q_{ij,k}\,Q_{kl,l} \\ & + L_2^{(3)}Q_{ij}Q_{ik,j}\,Q_{kl,l} + L_3^{(3)}Q_{ij}Q_{ik,k}\,Q_{jl,l} + L_4^{(3)}Q_{ij}Q_{ik,l}\,Q_{jk,l} + L_5^{(3)}Q_{ij}Q_{ik,l}\,Q_{jl,k} \\ & + L_6^{(3)}Q_{ij}Q_{ik,l}\,Q_{kl,j} + \cdots \end{aligned}$$

Where, $L_i^{(j)}$'s are the temperature independent constants. Comparing the expansion terms with the conventional expression for Frank's free energy, we get:

$$K_{11} = \frac{9S^2}{2}\left(2L_1^{(2)} + L_2^{(2)} + L_3^{(3)} - L_5^{(2)} - 2L_6^{(2)}\right) + \frac{9S^3}{4}\left(-L_2^{(3)} + 2L_3^{(3)} + L_4^{(3)} + 2L_5^{(2)} - L_6^{(3)}\right)$$

$$K_{22} = 9S^2\left(L_1^{(2)} - L_6^{(2)}\right) + \frac{9S^3}{4}\left(L_4^{(3)}\right)$$

$$K_{33} = \frac{9S^2}{2}\left(2L_1^{(2)} + L_2^{(2)} + L_3^{(3)} - L_5^{(2)} - 2L_6^{(2)}\right) + \frac{9S^3}{4}\left(2L_2^{(3)} - L_3^{(3)} + L_4^{(3)} - L_5^{(3)} + 2L_6^{(3)}\right)$$

$$K_{24} = 3SL^{(1)} + \frac{9S^2}{2}\left(2L_1^{(2)} + L_3^{(2)} - \frac{1}{3}L_5^{(2)} - 2L_6^{(2)}\right) + \frac{9S^3}{2}\left(L_4^{(3)} + 2L_5^{(2)} - L_6^{(3)}\right)$$

$$K_{13} = 3SL^{(1)} + \frac{3S^2}{4}\left(L_5^{(2)}\right)$$

From the equations above we gather that the surface-like elastic constants K_{24} and K_{13} have a term linear in the order parameter while all the bulk terms to the leading order scale as square of the order parameter. We note that there could be higher order terms that scale linearly with S, but K_{24} and K_{13} are the only terms that correspond to deformations that are of the order $\sim\frac{1}{\lambda^2}$ (λ is the relevant system size). Hence we do not believe the contributions of the higher order terms are significant enough in comparison with K_{24} to influence the experiments we described above. However, we do note that the expansion of the free energy in the Landau- deGennes formalism is only valid very close to the transition where the order parameter is very small. Experimentally, the observations of the transitions from bipolar to radial droplet might correspond to an order parameter that is higher than those for which the Landau- deGennes expansion is applicable.

There has been some attention devoted to the determining if K_{13} indeed scales linearly with order parameter [28,97]. However, the very inclusion of K_{13} term in the Frank description of elasticity is fraught with controversy[26,28,98-102]. In order for the free energy functional to be well posed with the inclusion of K_{13}, higher order terms have to be included as well. Without the higher order terms the K_{13} term can be unbounded from below

allowing for large deformations in the director field[26]. Clearly, this contradicts the assumption of linear elasticity. Density functional theory calculations predict that the value of K_{13} is identically zero which automatically solves any paradoxes associated with the elastic constant[28].

In the same work[28], the authors also reveals a few important findings that are pertinent to our work. They discuss the influence of having a real boundary or interface on the way the elastic contributions are expressed. They conclude that although K_{24} is truly an intrinsic material parameter, it is not possible to isolate the contribution of the material K_{24} term from an interfacial K_{24}-like term (or an anchoring term). In the light of these results from density-functional theory we realize that the driving force for our experiments is an effective K_{24} term which is a combination of the bulk K_{24} term and a K_{24} like term that has its origin in the interfacial region and hence depends on the external medium as well. This effective K_{24} term is clearly not a material property anymore and would depend on the experimental conditions.

5.5 **Conclusions**

There have been a few studies recently about transition from bipolar to radial droplets induced via inclusion of endotoxins and through variation of droplet size[91,103]. Although fascinating experimentally, a full quantitative understanding is still lacking to explain these phenomena. Our work demonstrates how changes in internal order can bring about the same bipolar to radial transition. We explain the results by appealing to the theoretically predicted linear scaling of the surface elastic constants with order parameter. We bring to light this completely neglected aspect in the literature regarding the scaling of

the surface elastic constants. Further, manipulation of internal order opens up an array of interesting sensor applications using liquid crystal droplets. We foresee applications using liquid crystal droplets, where any external influence like contaminants and temperature fluctuations which can lower the order parameter and bring about switching in the droplet morphology.

CHAPTER 6. NEMATICS CONFINED TO TOROIDS WITH RADIAL ANCHORING

This section explores the ground state of nematic organization when confined to toroidal geometries with normal anchoring conditions. We study the coupling of the director configuration with geometry by varying the aspect ratio of the tori. All the experiments were performed in the laboratory and with the guidance of Dr. Fernandez-Nieves.

6.1 Introduction

Historically, the study of nematics confined in cylinders with radial boundary conditions has been a fertile area of research [29,31,32]. The first reported experimental observation of a point defect in nematics (hedgehog) was for a nematic confined to cylindrical capillary with normal anchoring conditions [104]. Further, some of the earliest research on measuring the saddle-splay elastic constant was also utilized the director configuration in a cylinder with radial anchoring [31,32,105]. This director configuration commonly observed in normally anchored cylinders has been artistically dubbed as the escape radial (ER) configuration. We describe some of the features of this director configuration below.

Consider a cylinder with radial anchoring. The expectation is that the director would only have a radial component with a defect line running through the center of the capillary. This configuration which is named as planar radial (PR) and is shown in Figure 6a. However, the PR configuration has never been experimentally observed. The director

instead bends out of plane and avoids the costly defect core. This is termed as escape in the third dimension. The schematic illustrating the escape radial configuration is shown in Figure 6b. The director profile of escape-radial configuration which minimizes the free energy is given by[105] $(n_r, n_\theta, n_z) = (sin\,\Omega, 0, \cos\Omega)$; where, $\Omega = 2Tan^{-1}(\frac{r}{a})$. Although the schematic shows a bend direction in one direction (right), it can be readily realized that there are two directions of escape (or two directions of bend) involve the same cost of director deformation. This creates an avenue for the presence of defects which separate regions that escape in opposite directions [104]. Hence, this setting was also suitable to study the annihilation dynamics of a radial and hyperbolic hedgehog [29]. The characteristic texture observed when escape-radial configuration is viewed under crossed-polarizers is shown in Figure 6.1c. The liquid crystal in question is 5CB and lecithin is used to coat the surface of the cylindrical capillary to ensure normal anchoring. The alternating dark and bright bands can be readily used to identify the escape-radial texture. The dark region at the edge of the capillary is due to the fact the liquid crystal molecules are normal to the surface and hence are along one polarizer. As we approach the center the molecules bend towards the long axis of the cylinder resulting in the bright region, as the director now makes an angle with either polarizer. Finally, close to the center the director points along the long axis of the cylinder and hence is parallel to the other polarizer resulting in the dark region at the center. We used cylindrical capillaries of diameters 400, 500 and 800 microns to perform these experiments. The intensity profile measured along the representative red dashed line of Figure 6.1c, is shown in Figure 6.1d. As we may expect, the intensity starts out at the lowest on the edge of the capillary and increases as the director bends towards the center. At the center of the capillary the profile has a local minima as it is again parallel to a polarizer.

We note that for the capillary diameters we use that ratio of the maxima/minima is always about 4.

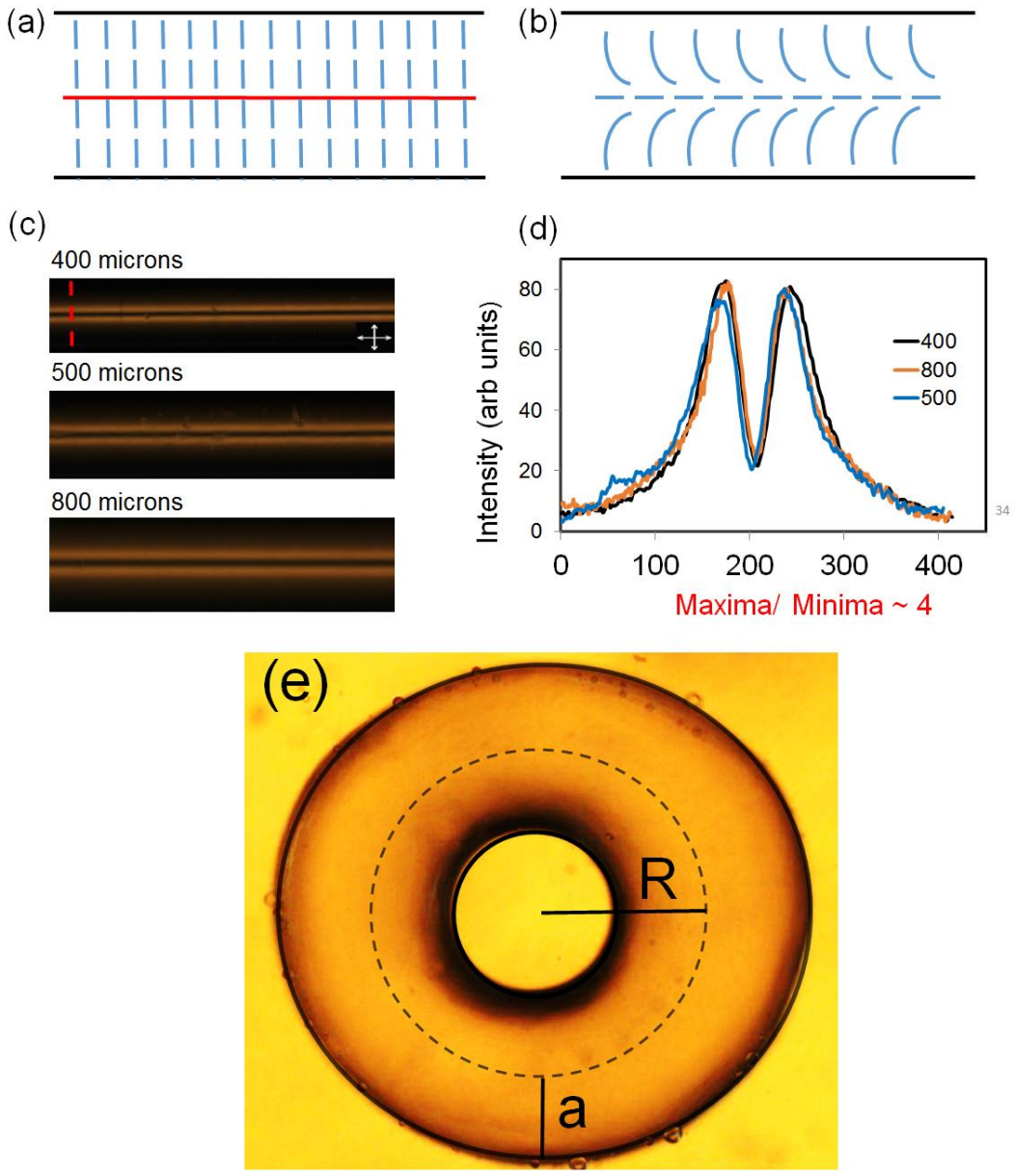

Figure 6.1 Director orientations along a horizontal slice along the long axis of the cylinder a) Planar-radial configuration with the red line in the center being the declination core b) Escape-radial configuration c) Texture of escaped-radial configuration observed under crossed-polarizers for cylindrical capillaries of diameter 400, 500 and 800 microns d) Intensity profile along a vertical slice of (c), the dashed line in red is a representative slice e) Brightfield image of a toroidal nematic

droplet depicting the two relevant length scalesed under crossed-polarizers for cylindrical capillaries of diameter 400, 500 and 800 microns d) Intensity profile along a vertical slice of (c), the dashed line in red is a representative slice e) Brightfield image of a toroidal nematic droplet depicting the two relevant length scales

A torus is defined by two characteristic length scales. This is illustrated in Figure 6.1e, where the 'a' is the tube radius and 'R' is the center to center distance. The ratio of the two length scales defines the aspect ratio of the torus ($\xi=\frac{R}{a}$). From a geometric perspective, a torus has inherent bend which is absent in a cylinder. This brings about additional physics pertaining to how these unique geometric aspects of a torus couple with the director configuration. For the case of a planar anchored torus, it was recently demonstrated that a novel doubly-twisted structure was the preferred ground state in place of an axial configuration [9]. The authors clearly exemplify the role of the two competing curvatures in a toroidal geometry which results to the director conforming to a doubly-twisted configuration. Motivated by these previous results, we seek to explore the director configuration under toroidal confinement but with normal anchoring conditions. We will contrast the results observed in the torus with the escape-radial configuration of the cylinders to help identify the new phenomenology. All the results described are with strong radial anchoring.

6.2 Director configuration in a torus with normal anchoring conditions:

Figure 6.2a shows the cross-polarized texture of a torus ($\xi\sim 5$) with radial anchoring. If we observe the parts of the torus that lie parallel to a polarizer (red line in Figure 6.2c), we can note that the texture is qualitatively similar to that observed for the escaped radial texture observed in cylindrical capillaries. The bright-field image in Figure 6.2b reveals the lack of scattering indicating the absence of singular defects. This is also

consistent with expectation of the escape-radial configuration provided there is only one direction of escape. Although, the optical texture is qualitatively consistent with the expectation from an escape-radial configuration, there are quantitative differences in the intensity profiles when compared to cylinders.

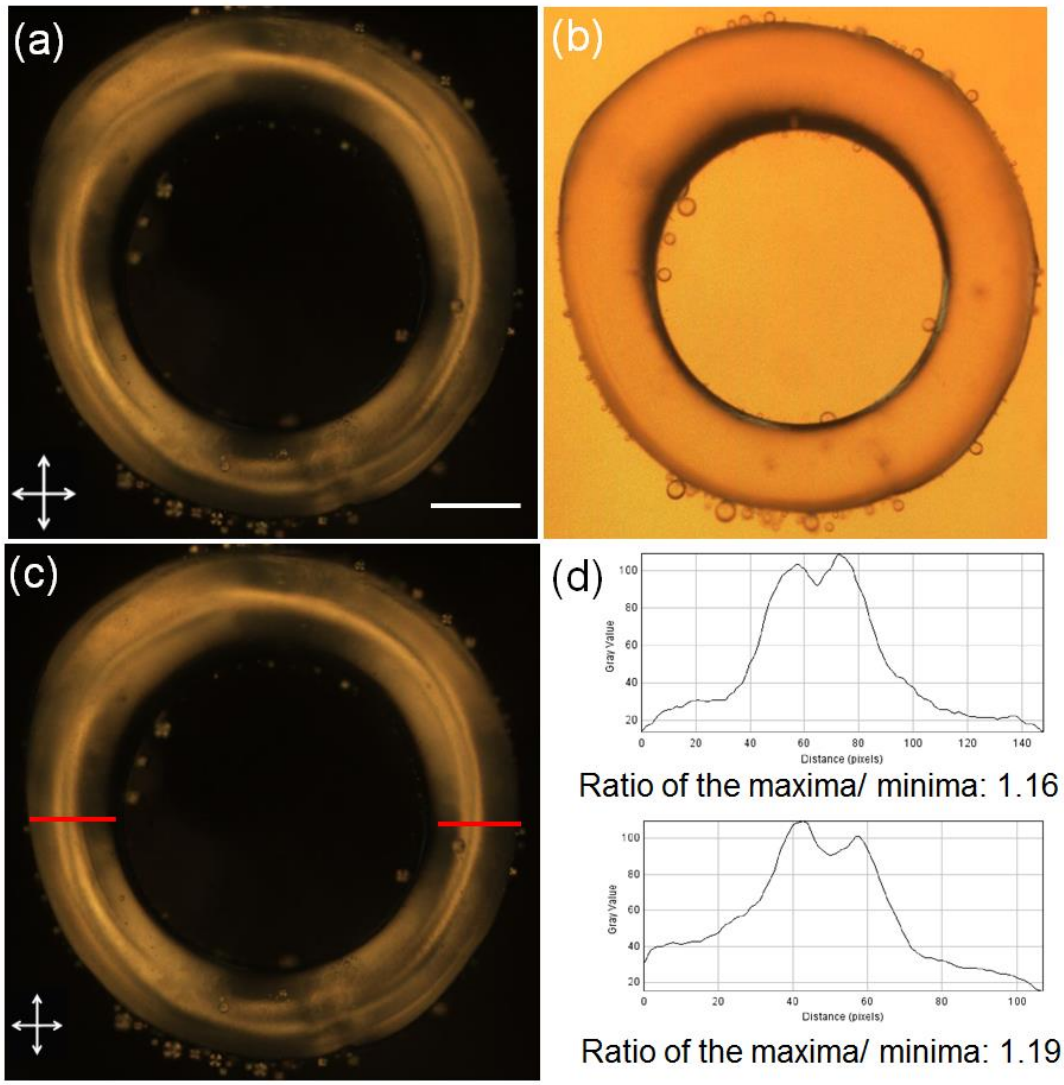

Figure 6.2 Nematic liquid crystals confined to toroidal geometry with radial anchoring a) Crossed-polarized image of a torus with aspect ratio ~4.7 b) Brightfield image of the same torus c) Red lines added to the cross-polarized image in (a) to denote the region of which we plot the intensity profile in (d), d) Intensity profile along a slice shown by the red line in (c)

Similar to the cylinder we measure the intensity profile along the red lines shown in Figure 6.2c. The intensity has a similar profile to what was noted earlier for cylinders. As expected close to the surface of the torus, the molecules are normal to the surface and hence parallel to the polarizer in the plane of the red line in Figure 6.2c. Hence the intensity is the lowest close to the surface. We see an increase in the intensity as we move away from the surface and finally, there is local minima close to the center of the torus. This is qualitatively similar to the observations in the case of cylindrical confinement. However, we observe that the ratio of $\frac{I_{max}}{I_{min}}$ ~ 1.2, which is considerably lower than what was observed for the escape radial configuration in a cylinder ($\frac{I_{max}}{I_{min}}$ ~ 4). The tube radius of the torus under observation is around 400 microns, which is similar to the size of the cylindrical capillaries. Hence the size dependent scattering of light has no role to play in influencing the observed intensity ratios[2]. It is likely that the additional cost of deformation that is inherent in a toroidal geometry is the likely cause of this new phenomenology.

The observation that the central region of the torus is brighter than what might be expected for an escaped-radial configuration hints to us that there can be a twist deformation in the director arrangement [9]. This postulation is in keeping with the observations of a planar anchored torus and cylinders wherein the central region of the was brighter than what would have been expected if the configuration was axial [9,12]. Further, we note that the profile of the intensity observed for the torus is reminiscent of twisted escaped-radial configuration observed for LCLCs confined to cylinders with radial anchoring[67]. In the case of LCLCs it is the anisotropy of elastic constants (K_{22}<<K_{11}~K_{33}) that results in the director resorting to a twist deformation to offset some of the more

expensive splay and bend deformations. However, in our experiments with 5CB, there is not a significant amount of anisotropy in the values of the elastic constants. It is the geometry alone that gives rise to the new phenomenology. We verify this with experiments using bent cylindrical capillaries below.

6.3 **Experiments on bent-cylinders:**

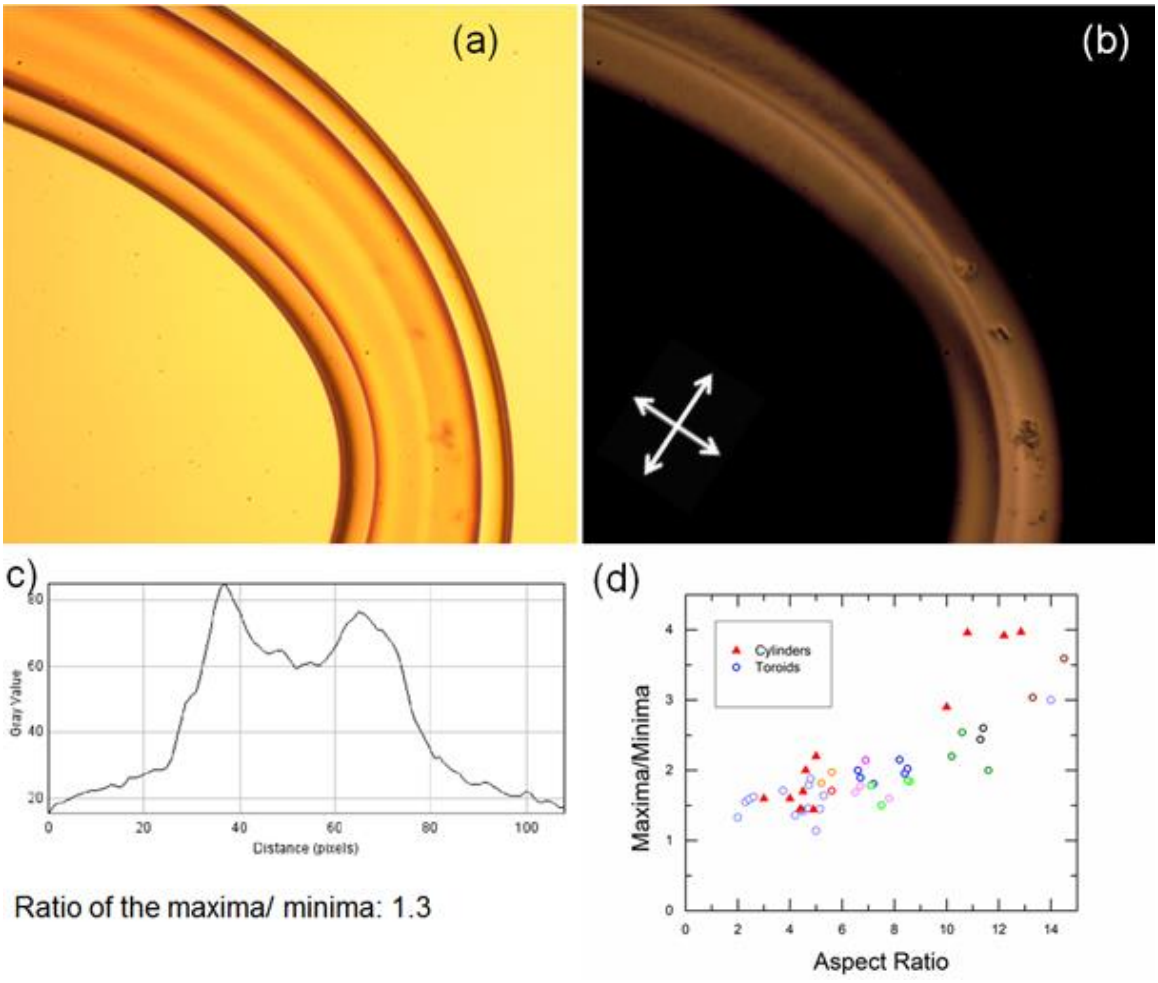

Figure 6.3 Nematic liquid crystals confined to bent cylindrical capillaries a) Brightfield image of 5CB confined to a bent cylindrical capillary b) Cross-polarized image of the 5CB confined to a bent capillary c) Intensity profile parallel to a polarizer d) Plot of the maxima/minima for tori and bent cylinder as a function of aspect ratio

After postulating that the configuration of radially anchored liquid crystals in a torus is that of an escaped-radial with twist we seek to decouple the role of geometry and topology in the observed phenomenology. For this reason, we perform experiments on bent cylindrical capillaries. The geometry of the bent cylindrical capillaries is similar to a torus but they are clearly distinct in a topological sense.

Brightfield image of representative bent cylinder is shown in Figure 6.3a. The corresponding cross-polarized image is shown in Figure 6.3b. From Figure 6.3c The intensity profile (along a polarizer) measured in a bent cylindrical capillary is similar to that of the torus. The intensity profiles of the bent cylinder help in clarifying that the phenomenology observed is a result of the additional bend in the geometry as compared to a cylinder. While topology might play a part in other phenomenology pertaining to defects and more [9], it appears that the escape-radial with twist configuration is a consequence of only the additional bend in the geometry. It would then seem natural that the observed intensity profile would be a function of the amount of bend (aspect ratio) in the geometry. We quantify the ratio of maxima/minima in the intensity as a function of aspect ratio in Figure 6.3d. The procedure to calculate the aspect ratio of the bent cylindrical capillaries is described in the material and methods section of this chapter. We see that for very high aspect ratios (ξ~12 and above), the intensity ratio is reminiscent of the behavior in cylinders ($\frac{I_{max}}{I_{min}}$ ~ 4). As the aspect ratio is lowered and consequently the bend in the geometry increases we see that the ratio of $\frac{I_{max}}{I_{min}}$ decreases. This is consistent with the idea that, some part of the additional splay and bend deformations imposed on the director by the geometry is relieved via a twist deformation. We provide some analytical estimates below for the

additional cost of splay and bend deformations involved with an escaped-radial configuration in a torus.

6.4 Additional Free energy cost of escaped-radial configuration in a torus:

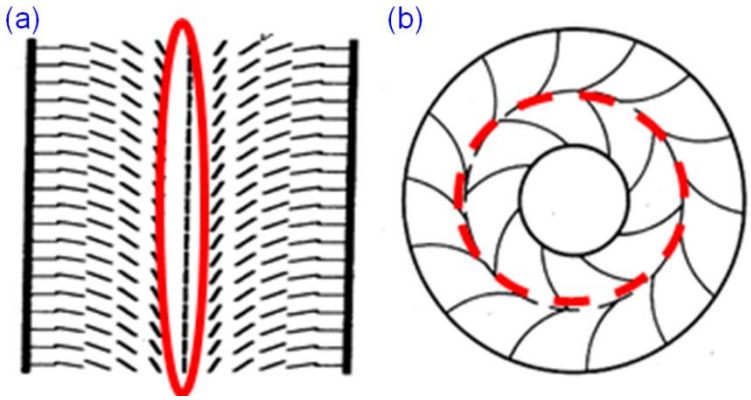

Figure 6.4 Schematic of the additional bend of the escaped core and splay at the inner handle in a torus as compared to the cylinder

The escaped core is the case of a cylinder is free of deformation and the director points along the long axis. This feature can be clearly noted from the schematic in Figure 6.4a. However, in the case of torus the escaped core has a significant amount of bend, which depends on the aspect ratio of the torus. Clearly, the bend in the geometry results in additional contribution of bend to the overall energy cost of deformation. In addition to this, we note that there is also additional splay deformation in the toroidal geometry that is absent in the case of the cylinder. It is easier to observe the splay by looking near the inner handle of the schematic in Figure 6.4b. In below we estimate the additional cost of these two deformations when the director conforms to an escape-radial configuration in a torus.

We extend the escaped-radial ansatz using the proper metric terms to assume an ansatz for the escape-radial configuration in a torus [31,32,105]:

$$(n_r, n_\theta, n_\emptyset) = (\frac{sin\ \Omega}{R+rcos\theta}, 0, \sqrt{1-n_r^2})\text{; where, } \Omega = 2Tan^{-1}(\frac{r}{a})$$

Where, θ is the polar angle and r is the radial co-ordinate. Expanding the deformation terms of the Frank's free energy, we find that there are two additional terms in comparison with the escape radial configuration in a cylinder.

$$F = 2\pi K_{33} \iint \frac{rcos^2\theta\ cos^2\Omega}{R+rcos\theta} d\theta\ dr + 2\pi K_{11} \iint \frac{rcos^2\theta\ sin^2\Omega}{R+rcos\theta} d\theta\ dr$$

$$F = \frac{\pi RK}{2\xi^2}\left(1 + \frac{3}{8\xi^2} + \frac{5}{48\xi^4} + O\left(\xi^{-6}\right)\right) \quad (6.1)$$

For a torus of $\xi \sim 1.5$, the additional deformation energy in the escape radial configuration of a torus is comparable to the cost of the escape radial configuration ($\sim 2\pi RK$) in a cylinder (assuming a single constant approximation).

While, the analytical approach is useful in estimating the cost of the additional deformation involved with having an escaped-radial configuration in a toroidal geometry, it becomes untenable to directly compare the free energy cost of escape-radial and twisted escape-radial configurations. Further work following a numerical approach is needed to determine the ground state of radially anchored tori.

6.5 **Conclusions**

In this chapter we study the ground states of normally anchored nematic tori. We find a preference of a twisted-escaped radial configuration when the aspect-ratios of the tori are sufficiently low. This configuration has never been observed previously in the case of small molecule liquid crystals like 5CB. Although, LCLCs show similar behavior when

confined to cylinders, we note that the emergence of the twisted escape-radial configuration in that instance is due to the anisotropy of the elastic constants. In our experiments it is the geometry of the confinement that results in the novel director configuration. However, more theoretical work is needed to unequivocally determine the ground state of normally anchored nematic tori.

6.6 **Materials and methods:**

6.6.1 Aspect ratio of bent cylinders

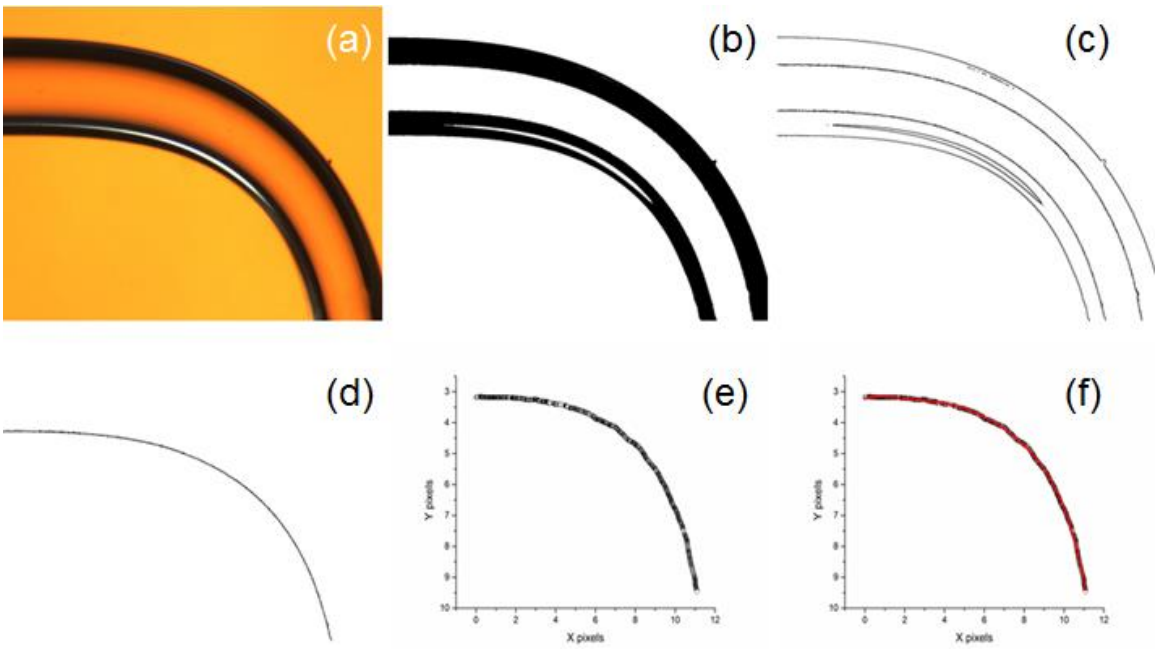

Figure 6.5 Procedure for the calculation of aspect ratio of bent cylinders a) Brightfield image b) Use Image J software's binary conversion c) Use Image J software's finding edges module d) Isolate inner edge of the capillary e) and f) curve- fitting of the inner edge to a polynomial function

Figure 6.5 describes the procedure involved in converting the brightfield image of a bent capillary to a polynomial fit of the inner diameter. After we obtain the polynmical function, calculation of the curvature is straightforward.

6.6.2 Ensuring normal anchoring of nematic tori

The procedure put forward to generate stable nematic drops with handles was used in the experiments pertaining to the toroidal droplets [9]. In their method carbopol is used as the yield-stress medium to prevent the collapse and breakup of toroidal droplets. We add sufficient amount (>10 mM) of sodium do-decylsulfate (SDS) to the carbopol to ensure normal anchoring.

CHAPTER 7. ROLE OF DIFFERENTIAL POLARIZABILITY IN RAMAN SCATTERING EXPERIMENTS ON LIQUID CRYSTALS

In this chapter we use nematics confined to rectangular cells to perform Raman scattering measurements of their order parameters. Polarized Raman scattering can be used to determine the orientational distribution function in ordered materials. Conventional measurements of the second (P_2) and fourth moments (P_4) of the orientational distribution function using polarized Raman scattering result in values of fourth moment which are in stark disagreement with theory. More recently, experimental improvements have been suggested with the full spectrum of depolarization ratios being used to measure the order parameters. This technique resulted in values of P_4 which were in much better agreement with theory. In this chapter, we show that when an accurate value of the ratio of the differential polarizability is used, the conventional method is equally effective in capturing the values of the fourth moment of the orientational distribution function accurately. We postulate based on ongoing theoretical calculations by our collaborators in Mc Gill university that, the difference in the molecular confirmations resulting from a different dihedral angles in the nematic and isotropic phase are likely to blame for the different values of the ratio of differential polarizability in the two phases.

7.1 Introduction

Nematic liquid crystals are rod like molecules that orient on average along a preferred direction called the director (**n**). Governed by thermal fluctuations, a molecule at a given instant makes a polar angle β with the director axis. The orientational distribution

function (ODF) can then be constructed to describe the orientation of all the molecules in the nematic phase [106,107] . Given the cylindrical symmetry that a typical nematogen possesses, the orientation of the molecule can be completely described by the polar angle β. The orientation distribution function can be expanded in terms of averaged Legendre polynomials <$P_n(\cos\beta)$> as $f(\beta) = \sum_L^{\infty} \frac{2L+1}{8\pi^2} < P_L(\beta) > P_L(\beta)$.

Although the ODF provides the complete description of the orientation distribution of all molecules in the system, the second (P_2) and fourth moments (P_4) are sufficient to determine many characteristic properties of nematics [88,108-110]. While P_2 can be measured by several experimental techniques, Polarized Raman Scattering is one of the few techniques that can measure both P_2 and P_4 simultaneously.

Conventionally the measurements of P_2 and P_4 using polarized Raman measurements have been based on the pioneering work of Jen et al [106,107]. The P_2 values found by their method are in satisfactory agreement with theory. However, the P_4 values so calculated were much lower than theoretical predictions [111]. For some materials like MBBA even negative values of P_4 have been reported [111,112]. There was considerable theoretical effort to make sense of the low P_4 values as simple mean field theories like Maier- Saupe do not permit a negative value of P_4 [113,114]. These corrections could not remedy the mismatch between the theory and experimental measurements.

7.2 **A better experimental methodology to determine P_4**

More recently Jones et al developed a framework to calculate the values of P_2 and P_4 using the full spectrum of depolarization ratios ($R = \frac{I_\perp}{I_{ll}}$) [45]. In their method the

depolarization ratio is measured as a function of the director orientation with respect to the polarizers at 5 degree intervals from 0 to 360 degrees. The value of P_4 obtained by this method is in much better agreement with theory as compared to the method of Jen et al. Measurements of P_2 and P_4 using the method of Jones et al has been made for a number of systems including some biaxial nematics [108,109].

We describe the methods of Jen et al and Jones et al in detail in the section below. In here we motivate what prompted us to have a deeper look at the method of Jones et al even though the data generated by the method gave satisfactory estimates of the order parameter.

We note that while the method of Jones et al does remedy the problem of unusually low values of P_4 resulting from conventional methods, there is need for caution while using this method. The method of Jones et al is based on a simple model for the intensity of the Raman signal as a function of the angle the director makes to the incident laser. A significant approximation of this method is to neglect the non-linear terms resulting from the coupling of the ordinary and extraordinary components on the wave-vector. The method of Jen et al is far cleaner in this regard as the method requires intensities only at angles 0 and 90 degrees, which the director makes with respect to the incident polarization. At these two angular positions there is no coupling of the ordinary and extraordinary components.

7.3 Comparing the methodology of Jen et al and Jones et al to determine the order parameters

Consider a nematic molecule that is making an angle β with the z-axis in the laboratory frame of reference. The induced dipole moment generated by an incident electric field ($\vec{E}$) can then be written as $\mu_Z = \alpha_{ZZ} E_Z cos\beta$, Where, α is the polarizability tensor. A suitable assumption to make for rod like molecules is that the in the molecular frame of reference the polarizability along the long axis of the molecules is much larger than the two perpendicular directions ($\alpha_{zz} > \alpha_{xx} = \alpha_{yy}$). Unlike spectroscopic techniques like Infra-red spectroscopy where in the intensity measured depends on the polarizability, the intensity measured in Raman spectroscopy depends on the differential polarizability ($\alpha'_{zz} = \frac{d\alpha_{zz}}{dz}$). The intensity of Raman scattering from a nematic medium can be expressed as: $I_{ij}(\theta) = k\, \alpha'^2_{ij} \int_{\beta} f(\beta) \left(E_{ij}(\beta)\right)^2 \sin(\beta) d\beta$

Where, β is the angle between the director and the incident polarization. The notation I_{ij} denotes the intensity with the polarizers along directions i and j in the laboratory frame of reference.

The method of Jen et al involves the measurement of Raman intensity with the director in two configurations; with the director parallel and perpendicular to the incident polarization.

$$R_1 = \frac{I_{\perp}(\theta = 0^{\circ})}{I_{ll}(\theta = 0^{\circ})}, \quad R_2 = \frac{I_{\perp}(\theta = 0^{\circ})}{I_{ll}(\theta = 90^{\circ})}, \quad R_{iso} = \frac{(1-r)^2}{3+4r+8r^2} \qquad (7.1)$$

Where, r is the ratio of the differential polarizability $r = \frac{\alpha'_{xx}}{\alpha'_{zz}} = \frac{\alpha'_{yy}}{\alpha'_{zz}}$. The equation above has the three expressions used to determine three variables P_2, P_4 and r. In order to

determine r the depolarization ratio (R_{iso}) in the isotropic phase where P_2 and P_4 drop off to zero is evaluated and solved for r. Jen et el assume the r so calculated in the isotropic phase is the same in the nematic phase as well. The authors provide the justification for the assumption based on the reasoning that the near neighbor correlations are not affected by a phase transition. Being a molecular property, they argue that the value of r should be governed mainly by near neighbor correlations. We will show below that this assumption may be flawed and is critical to the measurements of the value of P_4.

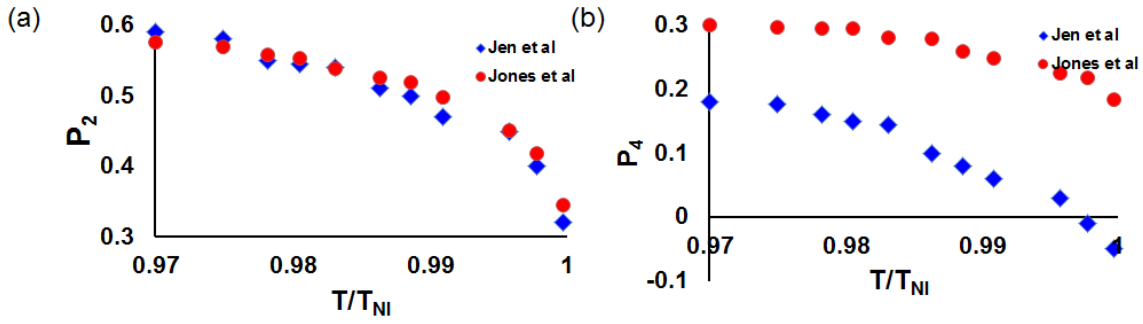

Figure 7.1 Order parameters P2 and P4 measured by the method of Jones et al and Jen et al

Figure 7.1 shows the data of P_2 and P_4 as obtained by the conventional method of Jen et al for 5CB. In accordance with several previous reports we also find that the values of P_2 are in good agreement with theory. However, the values of P_4 so determined are significantly lower than the theoretical expectations and for certain values of temperature even negative values were calculated.

The method of Jones et al measures the spectrum of depolarization ratio as a function of the angle which the director makes with the incident polarization as it varies from 0 to 360 degrees at fixed intervals. They derive the expression derive for the intensity as a function of the director angle with the polarizers.

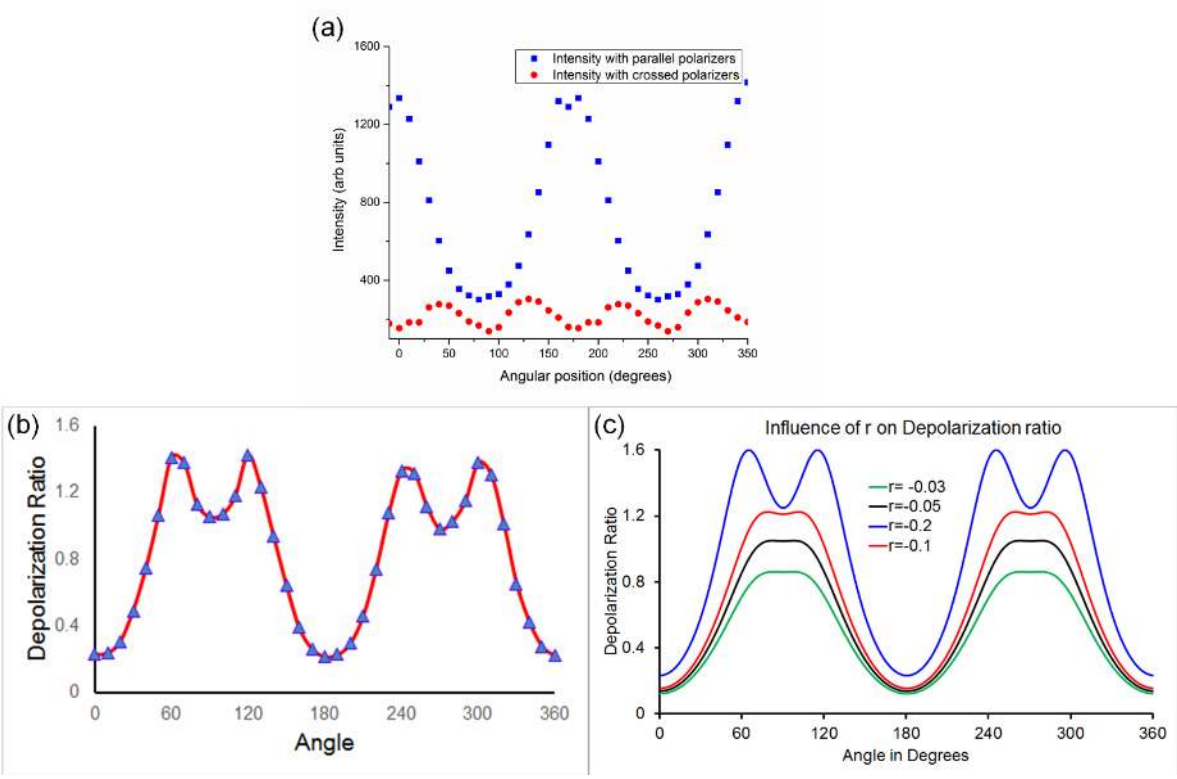

Figure 7.2 a) Intensity data measured by Raman scattering experiments for parallel and perpendicular polarizers (b) Experimental profile of the depolarization ratio (c) Simulations of the profile of the depolarization ratio for different values of differential polarizability

We note that in the method of Jones et al, the intensity profile of the depolarization ratio is curve fitted with the expression they derive. In their procedure the value of r in the nematic phase is treated as a fitting parameter free to take values different from that calculated in the isotropic phase. We take a closer look at the intensity profiles of the data generated by using the method of Jones et al below. We see in Figure 7.2a that there is a twofold symmetry in the intensity measured with parallel polarizers and a fourfold symmetry in the intensity data of perpendicular polarizers. This is consistent with the expectation from the intensity equation of Jones et al. A characteristic experimental profile of the depolarization ratio $R(\theta)$ is shown in Figure 7.2b. While the global minima of this profile is at 0^o, 180^o and 360^o, we observe that there are local shallow minima in between

the two peaks in the intensity profile. This is a universal feature that we observed for all liquid crystals we performed experiments on including LCLCs. This feature of the observed experimental profiles proves to be quite useful in bringing about some of the important aspects regarding the value of the differential polarizability.

Using the expression of Jones et al we simulate intensity profiles for different values of r. This is shown in Figure 7.2c. In this Figure, we note that when compared to the experimental intensity profile (shown in dotted lines), the simulated profiles which use values of r greater than -0.2, do not even qualitatively capture the profile. The shallow minimum in the intensity profile is only captured for values of r = -0.2. This is an important consideration because in the conventional method of Jen et al, the value of r, which was measured in the isotropic phase was around -0.03.

7.4 **Role of differential polarizability**

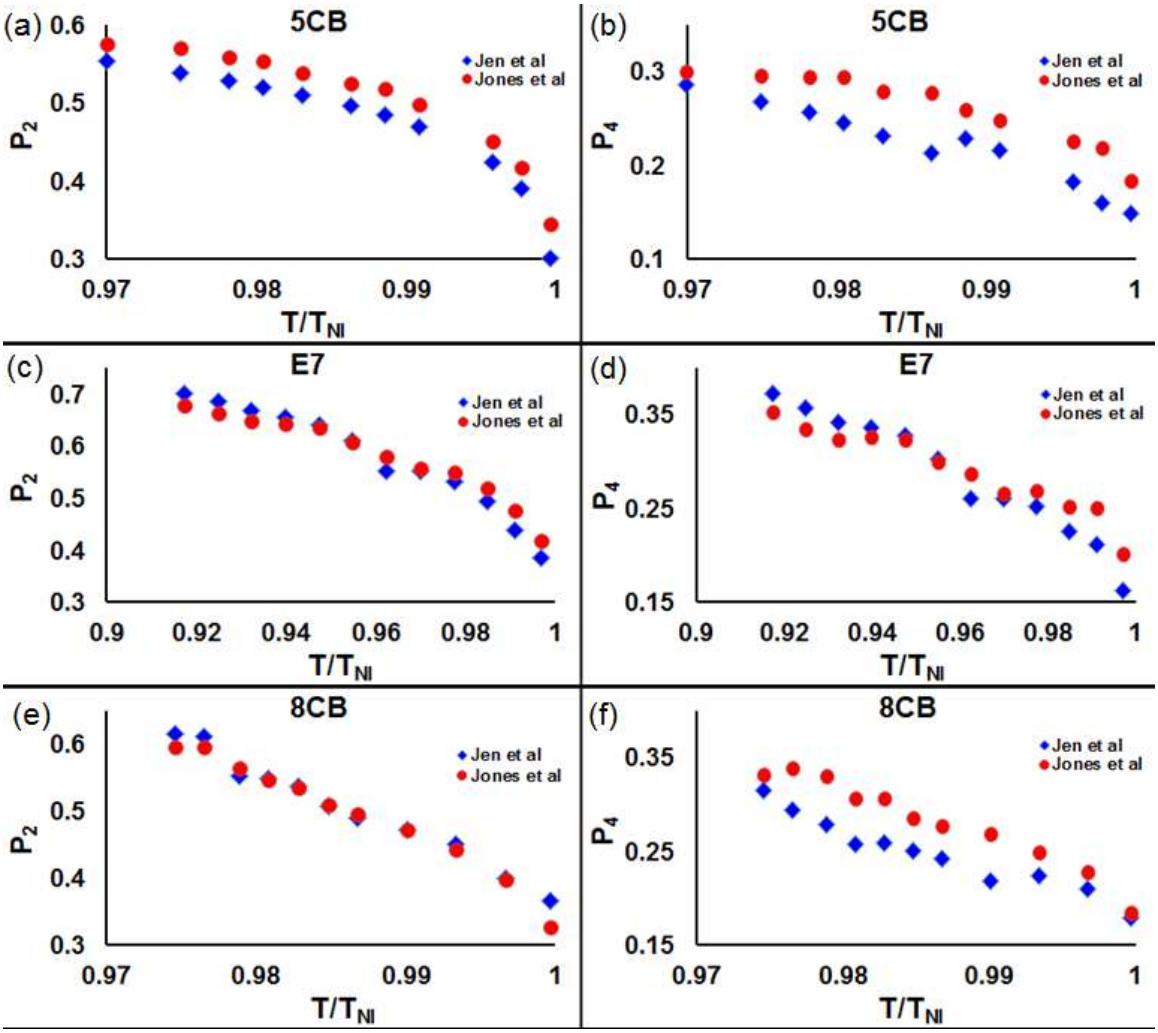

Figure 7.3 Order parameter data for the three liquid crystal 5CB, 8CB and E7 a) P_2 for 5CB b) P_4 for 5CB c) P_2 for E7 d) P_4 for E7 e) P_2 for 8CB f) P_4 for 8CB

With this understanding of how P_2 P_4 and "r" affect the depolarization spectrum we can ask a question about the method of Jones et al: If it is the better statistics that leads to better estimate of P_4 or would the method of Jen et al work equally well provided there was an apriori way to determine the value of "r". To answer that, we calculate using the values of depolarization ratio at angles equal to 0^o and 90^o, but instead of using the value of "r" from the isotropic phase as was the case in the old method of Jen et al we use "r" obtained from the fitting procedure of Jones et al. The results are shown in Figure 7.3 and it is evident

from the plots that for all the three liquid crystalline materials 5CB, 8CB and E7 the results obtained from the two methods are nearly identical. This leads us to believe that it is the accurate determination of the value of "r" which is the important variable in the problem, as opposed to better statistics which makes the method of Jones et al successful.

These results also bring to light the lack of theoretical attention in determining the value of r in the nematic phase. The conventional argument that r being a molecular property should not vary much across the nematic-isotropic transition might require a revisit [106,107]. It has been suggested that anisotropy of the local fields in the nematic phase can lead to different molecular properties [115]. The authors of that paper show that when a liquid crystal with a small optical anisotropy in the refractive index is used, the conventional method is suitable in determining P_4. The argument being that, the low anisotropy in the refractive index would result in negligible anisotropy of the local fields in the nematic phase. Hence, the assumption of having the same r in both the nematic and isotropic phase would hold true, leading to accurate determination of the order parameters using the conventional method. However, for conventional nematics this assumption might not always hold. The value of r in the nematic phase that is obtained from curve-fitting procedure of Jones et al is around ~ -0.2 in the nematic phase. it is significantly different from the value in isotropic phase which is around -0.03. This also bodes well with the idea that anisotropy of local fields might be an important consideration in determining some molecular properties in the nematic phase. While we do not have a clear way to think about the physics behind the different values of the r in the two phases, preliminary theoretical calculations using density function theory by our

collaborators in Mc Gill university seem to indicate that the different dihedral angle in the two phases could account for the observed phenomenology.

7.5 **Conclusion**

We put forward the idea that the accurate determination of the ratio of the differential polarizability is the main reason for the discrepancy of the values of P_4 calculated by the conventional method of Jen et al. When the values of "r" calculated from the fitting procedure were used as opposed to "r" calculated from the isotropic phase, the results using the method of Jen et al were in excellent agreement with theory. Further the discontinuity of "r" at T_{ni} highlights the need for furthere theoretical attention to this problem which can aid future experiments.

CHAPTER 8. MACROSCOPIC ALIGNMENT OF LYOTROPIC CHROMONIC LIQUID CRYSTALS USING PATTERNED SUBSTRATES

In this chapter we describe experiments and analysis pertaining to the homogeneous planar alignment of LCLCs. The experiments in this chapter were performed by collaborators in KAIST. We provide the analysis for their experiments and provide an outlook and guidelines for future experiments that seek to align LCLCs using tessellated patterns, which is the most ubiquitous method in the literature on aligning LCLCs.

8.1 Introduction

Lyotropic chromonic liquid crystals (LCLCs) are fundamentally different from thermotropic liquid crystals in the sense that the aspect ratio of the constituent units is dependent both on temperature and concentration [18,48,49,116-119]. The constituent units of LCLCs have flat aromatic cores with water-soluble peripheral groups that enable them to spontaneously assemble into long anisotropic structures in aqueous solutions. LCLCs have the added appeal of being water soluble, hence avoiding the complications of using volatile solvents for processing [120,121]. Further, aligned LCLCs have many interesting properties like dichroism due to their anisotropy of molecular structure. Monodomains of LCLCs on patterned surfaces can preserve their defect free structure when dried from the solution state, opening up many applications like use as polarizing sheets, water based organic electronics and bio sensing applications [46,120-123].

For using LCLCs in the aforementioned applications, it is essential that there exists a reliable way to obtain defect free monodomains over large areas. In addition, monodomains of LCLCs are essential to carry out fundamental studies for measuring the physical properties of ordered phases such as order parameters, elastic constants, and the anisotropic viscosities [18,46,124]. Aligning lyotropic systems and polymeric nematics has historically been rather difficult, thus limiting studies aimed at elucidating fundamental properties. Most conventional methods used for aligning small molecule thermotropic materials are not as effective in aligning these systems. There are a few examples, however, in the literature of polymeric systems that have been aligned using non-traditional methods [125-127]. Pressure driven extensional flow was used to align solutions of poly(1,4- phenylene-2,6-benzobisthiazole) in methane sulfonic acid. The extruding flow produces alignment of the nematic at the bounding surfaces, which in this case was a rectangular capillary. The alignment can be rationalized with the argument that the velocity of the front at the center of capillary is much greater than at the edges, resulting in the so-called "fountain flow" where the fluid at the center spills out to the edges of the capillary [127,128]. Solutions of poly-benzyl glutamates have also been aligned to produce monodomains and the elastic constants, various viscosities could be determined [125].

LCLCs bear similarity with polymeric nematics in the sense that the structural units leading to the formation of the nematic phase are long semiflexible rods. Curiously both LCLCs and polymeric nematics are notoriously hard to align using conventional techniques [129,130]. A possible explanation for this is that the anchoring energy (W) provided by conventional rubbing techniques is not sufficiently high for aligning LCLCs and polymeric nematics. Another curious aspect about both polymeric nematics and LCLCs is that the

value of the twist elastic constant is significantly lower than the bend and splay elastic constants [18]. We believe that the lower energy of twist deformation becomes very relevant in the anchoring energy calculations of LCLCs and polymeric nematics on grooved surfaces because it is possible that the bend and splay deformations relieve some of the energy cost via a twist mode, thus resulting in a lower effective anchoring energy. Hence there is a need for developing techniques that can provide for anchoring energies that are significantly higher than those that are used to align thermotropic materials.

Despite the fact that LCLCs have been studied for over a decade or two, reliable methods for forming stable monodomains are few. Homogeneous alignment of chromonic liquid crystals has been obtained by using an azo-polymer thin film that was irradiated with linearly polarized light [131], by the normal rubbing process as well as evaporating a SiO_x layer [130] has been reported. Superfine abrasive has been used to rub glass substrates and achieve planar anchoring of LCLCs providing weak anchoring [18,132]. Rubbed layer of polyamide has also been used to align LCLCs [19]. Very recently alignment of LCLCs has been demonstrated using rubbing and topographic patterns using nanoimprinting [62,133] . Interestingly when molecular grooves are small enough, LCLCs align perpendicular to the rubbing direction [133]. Nanoimprinting is used to generate micro-channels which align LCLCs along the direction of the channels [62]. Further, several interesting features in the biphasic regime are reported by the same authors when LCLCs are confined in these tessellated patterns.

Berreman's theory predicts that the anchoring energy increases monotonically as a function of the amplitude (A) of the grooves used to align nematics [134]. This was our motivation initially for creating large amplitude patterns using secondary sputtering

lithography (SSL). The failure of conventional rubbing techniques to align LCLCs seems to suggest that the amplitude of grooves created by rubbing is not large enough to align LCLCs [135]. We have shown in a prior publication that the most common thermotropic liquid crystal, 5CB is well-aligned on surface patterned bifunctional ITO substrates using SSL [136]. In this report we use SSL to fabricate nano-sized line patterns of high aspect ratio (ca.15), leading to a tessellated surface that provides sufficiently high anchoring energy for aligning LCLCs. We note that the experimental part is similar to the previously reported work using nanoimprinting [62]. The anchoring strength is varied by controlling the height and amplitude of the tessellated patterns (varying qA). An extension of the Berreman theory is used to calculate the anchoring energy. Our study provides a guideline for future experiments on LCLCs for the range of anchoring energies that can provide stable and good alignment. With the analysis presented here we contextualize some of the results present in the literature on aligning LCLCs in terms of the anchoring energy (via qA) and the quality of alignment.

8.2 Fabrication of high aspect-ratio tessellated patterns

Fabrication of the template began with spin coating a thin polystyrene (PS) film (8 wt% of PS (MW=18,000 g/mol, Sigma Aldrich) solution in anhydrous toluene (Sigma Aldrich)) on an ITO surface. A pre-patterned poly(dimethylsiloxane) (PDMS) mold with a wavelength ($2\pi/\lambda$) of grooves equal to 500 nm and depth 600 nm was put on the PS coated surface and heated above the glass transition temperature to drive the PS polymer into the spaces of the mold patterns by capillary force. After cooling to room temperature, the mold was removed and PS line arrays were formed on the substrate (Fig. 8.1 a). The PS layer that remained on the bottom of the imprinted structure was subsequently removed by

O_2/CF_4 reactive-ion etching (RIE) operated at a flow of 40/60 sccm, a chamber pressure of 20 mTorr, and an RF power of 80 W (Fig. 9.1 b). The target material layer, ITO, exposed at the bottom was etched by Ar^+ ion milling process using the PS layer as a mask, thereby generating line wall structures along the PS pattern shape (Fig. 8.1c). The PS remaining on top of the target material pattern was completely removed by secondary O_2 RIE operation at a flow of 100 sccm (Fig. 8.1d). The line amplitude and the wavelength of the pattern can be controlled by employing numerous etching conditions to produce high resolution ITO line patterns over a 5 mm x 5 mm area.

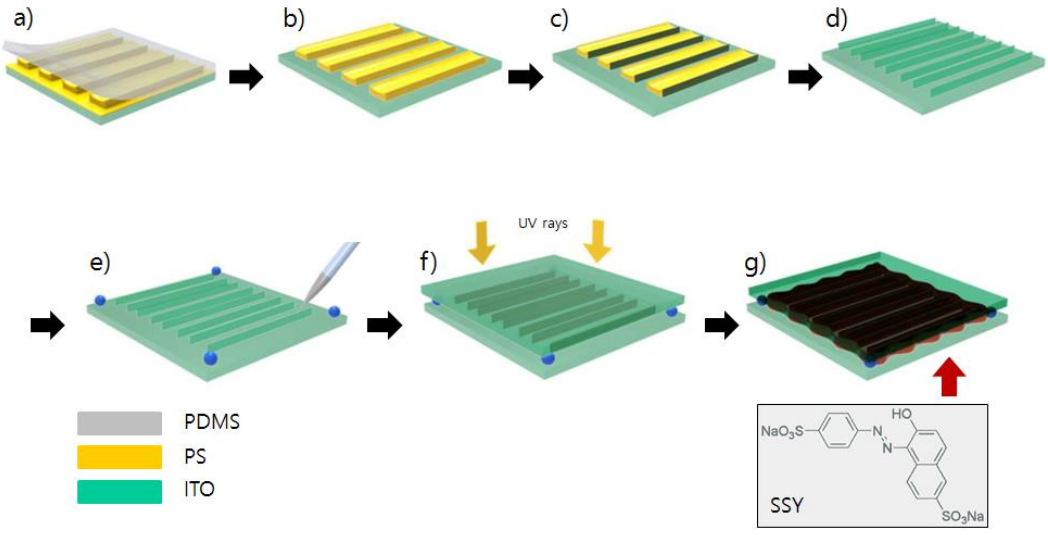

Figure 8.1 Scheme of the fabrication of LC cells using secondary sputtering lithography. (a) Line patterns are transferred from the PDMS mold to spin-coated PS substrates. (b) Residual PS layer is etched by RIE. (c) Formation of ITO walls by secondary sputtering llithography. (d) Removal of the PS template using O_2 plasma, resulting in ITO line patterns. (e) Control of the cell gap with PS micro-beads and NOA 63. (f) Upper substrate is placed parallel to the bottom substrate. NOA 63 is cured by UV rays. (g) The cell is filled with SSY using capillary force

The structural integrity of the patterns was tested using atomic force microscopy (AFM) and scanning electron microscopy (SEM) imaging. Fig. 8.2a and Fig. 8.2b show the 2D images of a substrate, observed using the noncontact mode of AFM and SEM. In

these representative images, the height of the patterns as measured by AFM was 250 nm and the width of lines is around 20 nm from SEM imaging. Fig. 8.2c to Fig. 9.2f show polarized optical microscope (POM) images of the cells filled with Sunset Yellow FCF (SSY) and disodium cromoglycate (DSCG). After sealing the cell with UV curable polymer (Norland Optical Adhesive 63), the cells are heated above the nematic-isotropic transition temperature (T_{NI}) to erase any effects of flow induced alignment.

8.3 Polarized optical microscopy observations

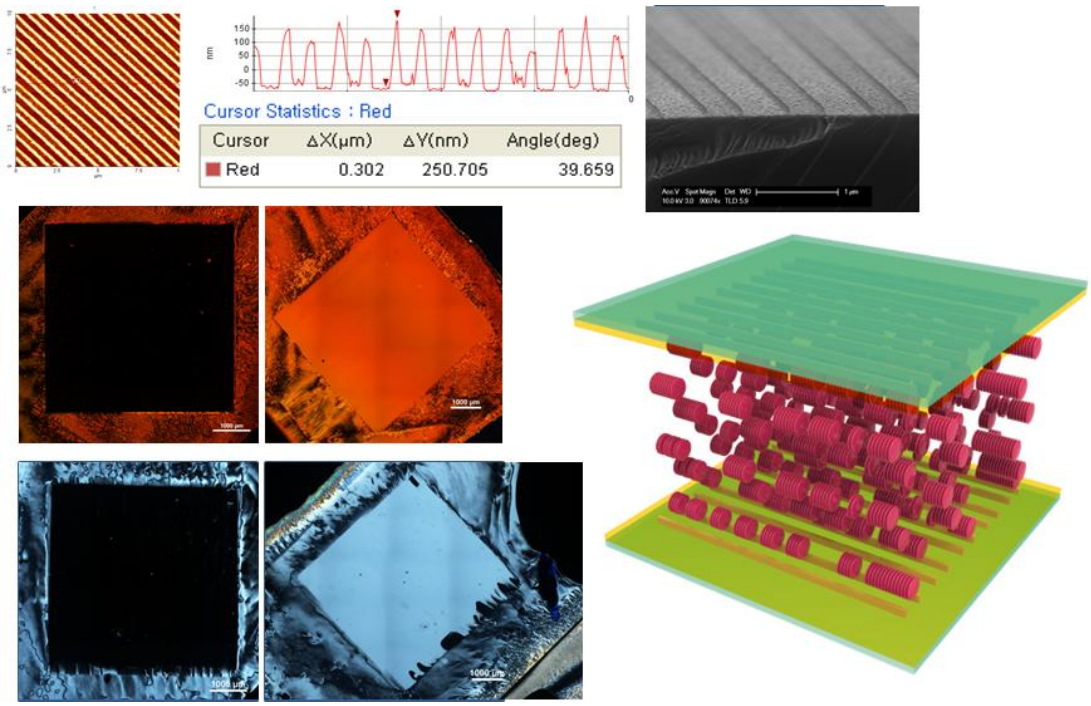

Figure 8.2 Alignment of SSY on patterned surfaces. (a) AFM images of the line patterns showing the periodicity and the amplitude of patterns. (b) An SEM image of the patterns. (c) SSY under crossed polarizers with the director parallel to the polarizer. (d) SSY with the director making an angle of 45° with the polarizers. (e) DSCG under crossed polarizers with the director parallel to the polarizer. (f) DSCG with the director making an angle of 45° with the polarizers. (g) Schematic of the alignment of the chromonics along the length of the patterns

It is clear from Fig. 8.2 that the cells show a 90^{o} periodicity under crossed polarizers and have the maximum intensity when the sample makes an angle 45^{o} with the polarizers. This confirms that the alignment caused by the line patterns is efficient in aligning LCLCs. Further to test the efficacy of the method, another LCLC, DSCG, was filled into the patterned structures (Fig. 9.2e and Fig. 9.2f). The cell with DSCG is fabricated with substrates having a groove height of 180 nm and the wavelength of the grooves is 500 nm. The behavior of DSCG is similar to SSY in the POM images and shows very good alignment on the surface of the periodic patterns.

8.4 Using an extension of Bereman's theory to explain the experimental observations

To better understand the alignment and to get an estimate of the anchoring strength created by the patterns, we employed Berreman's theory as a first approximation. In his seminal work, Berreman modeled the grooves to be sinusoidal and assumed that the amplitude of the grooves was much smaller than the period (wavelength) of the grooves [134]. Berreman also used a single constant approximation to estimate the cost of the elastic deformation. None of these assumptions is strictly valid in our experiments. We note that the Berreman theory gives an accurate estimate of the energy only when the amplitude of the grooves is comparable to the wavelength ($q = 2\pi/\lambda$) of the pattern but overestimates the energy for ($qA > 1$) [100]. The approximation of $qA << 1$ is clearly invalidated in many experimental conditions (for example, when A= 300 nm and λ= 500 nm). We evaluate the impact of the approximation on the anchoring energy from the numerical calculations reported by Barbero, et al [100].

The surface profile in our studies can be treated as a two dimensional sinusoidal profile in the x-z plane given by

$$z_0 = A(1 + \cos(qx)) \qquad (8.1)$$

In a previous study, it has been shown that the bend and splay elastic constants of LCLCs are quite close to one another, which allows for simplification of the problem with a single constant approximation [18]. The total cost of deformation, F, can then be written as:

$$F = \int_0^{\lambda} \int_0^{\infty} \frac{K}{2}\left(\theta_x^2 + \theta_z^2\right) dx\, dz \qquad (8.2)$$

Where, $\theta_x = d\theta/dx$ and $\theta_z = d\theta/dz$ and θ is the angle between the director and the x-axis.

Using the Leibnitz rule, it is straightforward to see that the solution of θ which minimizes the cost of deformation corresponds to the solution of the Laplace equation:

$$\frac{d^2\theta}{dx^2} + \frac{d^2\theta}{dz^2} = 0 \qquad (8.3)$$

with boundary conditions given by:

$$\lim_{z\to\infty} \theta = 0 \quad \text{and } \theta_0 = \arctan(qA \sin(qx)) \qquad (8.4)$$

When, $qA < 1$, the problem reduces to Berreman's original treatment. However, in our case, that assumption is clearly invalid. Analytical treatment of the problem becomes untenable when $qA \sim 1$, hence one has to resort to numerical methods as was done by Barbero, et al [100]. We use their numerical results to estimate the anchoring energies for our experimental system.

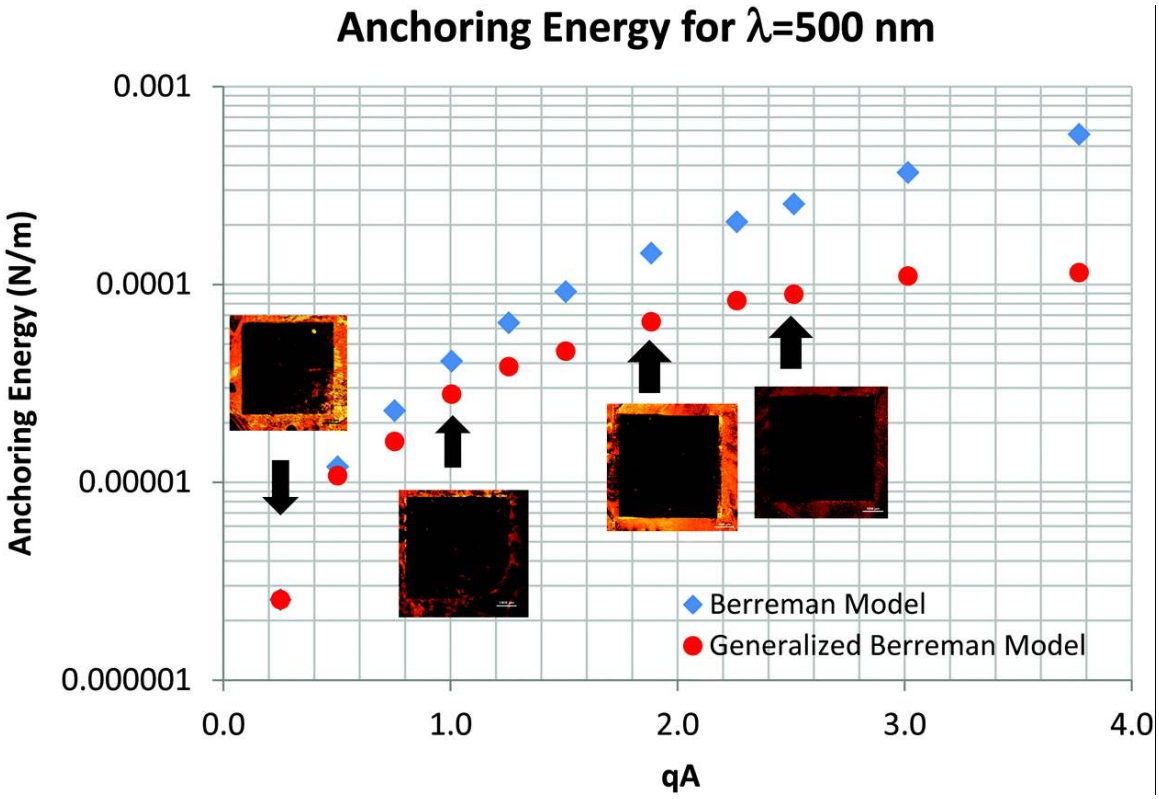

Figure 8.3 Calculated values of anchoring energy as a function of qA. Accompanying POM images show the integrity of alignment at different qA values. Notice that when qA < 3, unaligned regions are present indicating that the alignment is not perfect

As shown in Fig. 8.3, the values of the anchoring energies calculated from the Berreman's theory are significantly overestimated in the cases where $qA>1$. A crucial result to note is that unlike the Berreman analysis, the anchoring energy obtained by the numerical procedure levels off at around $qA= 3$. Hence the anchoring energy cannot be increased indefinitely by just increasing the height of the patterns. Also the plot in Fig 9.3 provides a rather convincing picture of why conventional rubbing techniques do not work well for aligning LCLCs. As can be seen in Fig 9.3, with the help of the accompanying POM images, we obtain good alignment when $qA \sim 3$. This result leads us to postulate that LCLCs cannot be aligned by conventional rubbing techniques as the amplitude of grooves caused by rubbing is much smaller than those used in our patterns [135]. The anchoring energy

corresponding to $qA\sim 3$ is 10^{-4} N/m. Anchoring energy around this value appears to be the cut off beyond which one can expect good homogeneous alignment of LCLCs. Comparing this with our previous results of using SSL to align 5CB, we note that the amplitude of the patterns needed to align LCLCs (A~250 nm) is much larger than what is needed to align thermotropic liquid crystals (A~100 nm) [13,136]. This corresponds to the anchoring energy needed to align LCLCs (10^{-4} N/m) is an order of magnitude larger than that needed to align thermotropic liquid crystals (10^{-5} N/m). Further, using the same analysis we can explain the weak anchoring of LCLCs (~ 10^{-6} N/m) obtained by using superfine abrasive ($qA << 1$) [27,132]. This result again highlights the importance of the use of SSL to achieve the high aspect ratio patterns that are essential to achieve anchoring energies large enough to align LCLCs.

8.5 **Conclusion**

In conclusion, we have successfully demonstrated a way to reliably align LCLCs using SSL. The SSL technique is utilized to make patterns that impose a sufficiently high anchoring strength on the LCLCs to enable good alignment. We conclude that the anchoring strength imposed by this technique (10^{-4} N/m) is higher than what is obtained from conventional rubbing techniques thus enabling the alignment. We observe with the help of POM that anchoring strength of about 10^{-4} appears to be a cutoff strength below which perfect alignment of LCLCs is not possible. The value of 10^{-4} N/m would serve as a cut off anchoring energy which future experiments seeking to align LCLCs should try to attain to achieve good alignment. Also when the appropriate corrections to the Berreman's theory are taken into consideration, it is noted that the anchoring energy using this technique levels off beyond (qA=3), suggesting one cannot achieve higher anchoring

strengths just simply by increasing the amplitude of the patterns. Further we postulate that the higher anchoring energy of LCLCs and polymeric nematics is related to their twist elastic constant being about an order of magnitude lower than the bend or splay. Future applications focusing on developing an aligned liquid crystal as a polarizer using SSL which can cover broad visible wavelength by mixing various LCLCs looks very promising. The technique of aligning LCLCs with patterns can also be extended to other fields like bio-sensors.

REFERENCES

1 Kleman, M. & Levrentovich, O. D. *Soft matter physics: An introduction*. (Springer, 2003).

2 de Gennes, P. G. & Prost, J. *"The Physics of Liquid Crystals", Chapter 4*. 2nd edn, (Clarendon Press, 1993).

3 Mermin, N. D. The topological theory of defects in ordered media. *Reviews of Modern Physics* **51**, 591-648 (1979).

4 Mikhail, V. K. & Lavrentovich, O. D. Defects in liquid crystals: homotopy theory and experimental studies. *Soviet Physics Uspekhi* **31**, 196 (1988).

5 CHUANG, I., DURRER, R., TUROK, N. & YURKE, B. Cosmology in the Laboratory: Defect Dynamics in Liquid Crystals. *Science* **251**, 1336-1342, doi:10.1126/science.251.4999.1336 (1991).

6 Irvine, W. T. M., Vitelli, V. & Chaikin, P. M. Pleats in crystals on curved surfaces. *Nature* **468**, 947-951, doi:http://www.nature.com/nature/journal/v468/n7326/abs/nature09620.html#supplementary-information (2010).

7 Frank, F. C. I. Liquid crystals. On the theory of liquid crystals. *Discussions of the Faraday Society* **25**, 19-28, doi:10.1039/DF9582500019 (1958).

8 LAVRENTOVICH, O. D. & PERGAMENSHCHIK, V. M. PATTERNS IN THIN LIQUID CRYSTAL FILMS AND THE DIVERGENCE ("SURFACELIKE") ELASTICITY. *International Journal of Modern Physics B* **09**, 2389-2437, doi:doi:10.1142/S0217979295000926 (1995).

9 Pairam, E. *et al.* Stable nematic droplets with handles. *Proceedings of the National Academy of Sciences of the United States of America* **110**, 9295-9300, doi:10.1073/pnas.1221380110 (2013).

10 Joshi, A. A., Whitmer, J. K., Guzman, O., Abbott, N. L. & de Pablo, J. J. Measuring liquid crystal elastic constants with free energy perturbations. *Soft Matter* **10**, 882-893, doi:10.1039/C3SM51919H (2014).

11 Koning, V., van Zuiden, B. C., Kamien, R. D. & Vitelli, V. Saddle-splay screening and chiral symmetry breaking in toroidal nematics. *Soft Matter* **10**, 4192-4198, doi:10.1039/C4SM00076E (2014).

12 Nayani, K. *et al.* Spontaneous emergence of chirality in achiral lyotropic chromonic liquid crystals confined to cylinders. *Nature Communications* **6**, doi:ARTN 8067
10.1038/ncomms9067 (2015).

13 Davidson, Z. S. *et al.* Chiral structures and defects of lyotropic chromonic liquid crystals induced by saddle-splay elasticity. *Physical Review E* **91**, doi:ARTN 050501
10.1103/PhysRevE.91.050501 (2015).

14 Lydon, J. Chromonic review. *J Mater Chem* **20**, 10071-10099, doi:10.1039/b926374h (2010).

15 Hunter, C. A. & Sanders, J. K. M. The Nature of Pi-Pi Interactions. *J Am Chem Soc* **112**, 5525-5534, doi:DOI 10.1021/ja00170a016 (1990).

16 Onsager, L. The Effects of Shape on the Interaction of Colloidal Particles. *Ann Ny Acad Sci* **51**, 627-659, doi:DOI 10.1111/j.1749-6632.1949.tb27296.x (1949).

17 Xiao, W. *et al.* Structural Correspondence of Solution, Liquid Crystal, and Crystalline Phases of the Chromonic Mesogen Sunset Yellow. *Crystal Growth & Design* **14**, 4166-4176, doi:10.1021/cg500752x (2014).
18 Zhou, S. *et al.* Elasticity of Lyotropic Chromonic Liquid Crystals Probed by Director Reorientation in a Magnetic Field. *Phys. Rev. Lett.* **109**, doi:10.1103/PhysRevLett.109.037801 (2012).
19 Zhou, S. *et al.* Elasticity, viscosity, and orientational fluctuations of a lyotropic chromonic nematic liquid crystal disodium cromoglycate. *Soft Matter* **10**, 6571-6581, doi:10.1039/c4sm00772g (2014).
20 Lee, S.-D. & Meyer, R. B. Crossover Behavior of the Elastic Coefficients and Viscosities of a Polymer Nematic Liquid Crystal. *Phys. Rev. Lett.* **61**, 2217-2220 (1988).
21 Meyer, R. B. in *Polymer Liquid Crystals* 133-163 (Academic Press, 1982).
22 Odijk, T. Elastic constants of nematic solutions of rod-like and semi-flexible polymers. *Liq. Cryst.* **1**, 553-559, doi:10.1080/02678298608086279 (1986).
23 Se, K. & Berry, G. C. Frank Elastic Constants and Leslie-Ericksen Viscosity Coefficients of Nematic Solutions of a Rodlike Polymer. *Molecular Crystals and Liquid Crystals Incorporating Nonlinear Optics* **153**, 133-142, doi:10.1080/00268948708074531 (1987).
24 Tortora, L. & Lavrentovich, O. D. Chiral symmetry breaking by spatial confinement in tactoidal droplets of lyotropic chromonic liquid crystals. *P Natl Acad Sci USA* **108**, 5163-5168, doi:10.1073/pnas.1100087108 (2011).
25 Jeong, J., Davidson, Z. S., Collings, P. J., Lubensky, T. C. & Yodh, A. G. Chiral symmetry breaking and surface faceting in chromonic liquid crystal droplets with giant elastic anisotropy. *P Natl Acad Sci USA* **111**, 1742-1747, doi:10.1073/pnas.1315121111 (2014).
26 Lavrentovich, O. D. & Pergramenshchik, V. M. Patterns in thin liquid crystal films and the divergence ("Surfacelike") elasticity. *International Journal of Modern Physics B* **09**, 2389-2437, doi:doi:10.1142/S0217979295000926 (1995).
27 Davidson, Z. S. *et al.* Chiral structures and defects of lyotropic chromonic liquid crystals induced by saddle-splay elasticity. *Phys. Rev. E* **91**, 050501 (2015).
28 Yokoyama, H. Density-functional theory of surfacelike elasticity of nematic liquid crystals. *Physical Review E* **55**, 2938-2957 (1997).
29 Cladis, P. E. & Brand, H. R. Hedgehog–antihedgehog pair annihilation to a static soliton. *Physica A: Statistical Mechanics and its Applications* **326**, 322-332, doi:http://dx.doi.org/10.1016/S0378-4371(03)00254-1 (2003).
30 Ambrozic, M. & Zumer, S. Chiral nematic liquid crystals in cylindrical cavities. *Phys. Rev. E* **54**, 5187-5197 (1996).
31 CRAWFORD, G. P. & ŽUMER, S. in *Liquid Crystals in the Nineties and Beyond* 331-376.
32 Kralj, S. & Žumer, S. Saddle-splay elasticity of nematic structures confined to a cylindrical capillary. *Phys. Rev. E* **51**, 366-379 (1995).
33 Nych, A. *et al.* Chiral bipolar colloids from nonchiral chromonic liquid crystals. *Phys. Rev. E* **89**, doi:ARTN 062502
10.1103/PhysRevE.89.062502 (2014).

34 Ondris-Crawford, R. *et al.* Microscope textures of nematic droplets in polymer dispersed liquid crystals. *Journal of Applied Physics* **69**, 6380, doi:10.1063/1.348840 (1991).
35 Jamali, V. *et al.* Experimental realization of crossover in shape and director field of nematic tactoids. *Phys Rev E* **91**, 042507 (2015).
36 Kaznacheev, A. V., Bogdanov, M. M. & Taraskin, S. A. The nature of prolate shape of tactoids in lyotropic inorganic liquid crystals. *Journal of Experimental and Theoretical Physics* **95**, 57-63, doi:10.1134/1.1499901 (2002).
37 Prinsen, P. & Schoot, P. v. d. Parity breaking in nematic tactoids. *Journal of Physics: Condensed Matter* **16**, 8835 (2004).
38 Yao, X., Nayani, K., Park, J. O. & Srinivasarao, M. Orientational Order of a Lyotropic Chromonic Liquid Crystal Measured by Polarized Raman Spectroscopy. *The Journal of Physical Chemistry B* **120**, 4508-4512, doi:10.1021/acs.jpcb.6b02054 (2016).
39 Horowitz, V. R., Janowitz, L. A., Modic, A. L., Heiney, P. A. & Collings, P. J. Aggregation behavior and chromonic liquid crystal properties of an anionic monoazo dye. *Phys. Rev. E* **72**, 041710 (2005).
40 Yao, X., Rey, A., Park, J. & Srinivasarao, M. Defect dynamics in monodomain formation of a lyotropic chromonic liquid crystal under confinement. *Bulletin of the American Physical Society* **56** (2011).
41 Shams, A., Yao, X. X., Park, J. O., Srinivasarao, M. & Rey, A. D. Disclination elastica model of loop collision and growth in confined nematic liquid crystals. *Soft Matter* **11**, 5455-5464, doi:10.1039/c5sm00708a (2015).
42 Chandrasekhar, S. & Ranganath, G. S. The Structure and Energetics of Defects in Liquid-Crystals. *Adv Phys* **35**, 507-596, doi:Doi 10.1080/00018738600101941 (1986).
43 Chandrasekhar, S. *"Liquid Crystals", Chapter 3*. 2nd edn, (Cambridge University Press, 1993).
44 Schoot, P. v. d. & Cates, M. E. The Isotropic-to-Nematic Transition in Semi-Flexible Micellar Solutions. *EPL (Europhysics Letters)* **25**, 515 (1994).
45 Jones, W. J., Thomas, D. K., Thomas, D. W. & Williams, G. On the determination of order parameters for homogeneous and twisted nematic liquid crystals from Raman spectroscopy. *J Mol Struct* **708**, 145-163, doi:10.1016/j.molstruc.2004.04.030 (2004).
46 Park, M. S., Wong, Y. S., Park, J. O., Venkatraman, S. S. & Srinivasarao, M. A Simple Method for Obtaining the Information of Orientation Distribution Using Polarized Raman Spectroscopy: Orientation Study of Structural Units in Poly(lactic acid). *Macromolecules* **44**, 2120-2131, doi:10.1021/ma101553v (2011).
47 (!!! INVALID CITATION !!!).
48 Park, H. S. *et al.* Self-Assembly of Lyotropic Chromonic Liquid Crystal Sunset Yellow and Effects of Ionic Additives. *J. Phys. Chem. B* **112**, 16307-16319, doi:10.1021/jp804767z (2008).
49 Edwards, D. J. *et al.* Chromonic Liquid Crystal Formation by Edicol Sunset Yellow. *J. Phys. Chem. B* **112**, 14628-14636, doi:10.1021/jp802758m (2008).

50 Israelachvili, J. N. in *Intermolecular and Surface Forces (Third Edition)* (ed Jacob N. Israelachvili) 503-534 (Academic Press, 2011).
51 Collings, P. J., Dickinson, A. J. & Smith, E. C. Molecular aggregation and chromonic liquid crystals. *Liq. Cryst.* **37**, 701-710, doi:Pii 923874354 10.1080/02678292.2010.481910 (2010).
52 Renshaw, M. P. & Day, I. J. NMR Characterization of the Aggregation State of the Azo Dye Sunset Yellow in the Isotropic Phase. *J. Phys. Chem. B* **114**, 10032-10038, doi:10.1021/jp104356m (2010).
53 Chami, F. & Wilson, M. R. Molecular Order in a Chromonic Liquid Crystal: A Molecular Simulation Study of the Anionic Azo Dye Sunset Yellow. *J Am Chem Soc* **132**, 7794-7802, doi:10.1021/ja102468g (2010).
54 Bernal, J. D. & Fankuchen, I. X-Ray And crystallographic studies of plant virus preparations III. *The Journal of General Physiology* **25**, 147-165 (1941).
55 Prinsen, P. & van der Schoot, P. Continuous director-field transformation of nematic tactoids. *The European Physical Journal E* **13**, 35-41, doi:10.1140/epje/e2004-00038-y (2004).
56 Prinsen, P. & van der Schoot, P. Shape and director-field transformation of tactoids. *Phys Rev E* **68**, 021701 (2003).
57 Maeda, H. An Atomic Force Microscopy Study for the Assembly Structures of Tobacco Mosaic Virus and Their Size Evaluation. *Langmuir* **13**, 4150-4161, doi:10.1021/la962105e (1997).
58 Oakes, P. W., Viamontes, J. & Tang, J. X. Growth of tactoidal droplets during the first-order isotropic to nematic phase transition of F-actin. *Phys. Rev. E* **75**, 061902 (2007).
59 S. Sonin, A. Inorganic lyotropic liquid crystals. *Journal of Materials Chemistry* **8**, 2557-2574, doi:10.1039/A802666A (1998).
60 Simon, K. A., Sejwal, P., Gerecht, R. B. & Luk, Y.-Y. Water-in-Water Emulsions Stabilized by Non-Amphiphilic Interactions: Polymer-Dispersed Lyotropic Liquid Crystals. *Langmuir* **23**, 1453-1458, doi:10.1021/la062203s (2007).
61 Williams, R. D. Two transitions in tangentially anchored nematic droplets. *Journal of Physics A: Mathematical and General* **19**, 3211 (1986).
62 Yi, Y. & Clark, N. A. Orientation of chromonic liquid crystals by topographic linear channels: multi-stable alignment and tactoid structure. *Liq. Cryst.* **40**, 1736-1747, doi:10.1080/02678292.2013.839831 (2013).
63 Wang, P.-X., Hamad, W. Y. & MacLachlan, M. J. Structure and transformation of tactoids in cellulose nanocrystal suspensions. *Nat Commun* **7**, doi:10.1038/ncomms11515 (2016).
64 Dierking, I. Chiral Liquid Crystals: Structures, Phases, Effects. *Symmetry* **6**, doi:10.3390/sym6020444 (2014).
65 Link, D. R. *et al.* Spontaneous Formation of Macroscopic Chiral Domains in a Fluid Smectic Phase of Achiral Molecules. *Science* **278**, 1924 (1997).
66 Hough, L. E. *et al.* Chiral Isotropic Liquids from Achiral Molecules. *Science* **325**, 452 (2009).
67 Jeong, J. *et al.* Chiral structures from achiral liquid crystals in cylindrical capillaries. *Proceedings of the National Academy of Sciences* **112**, E1837-E1844 (2015).

68 Martínez-González, J. A. *et al.* Blue-phase liquid crystal droplets. *Proceedings of the National Academy of Sciences* **112**, 13195-13200 (2015).
69 Humar, M. & Muševič, I. 3D microlasers from self-assembled cholesteric liquid-crystal microdroplets. *Opt. Express* **18**, 26995-27003, doi:10.1364/OE.18.026995 (2010).
70 Cox, J. S. G., Woodard, G. D. & Mccrone, W. C. Solid-State Chemistry of Cromolyn Sodium (Disodium-Cromoglycate). *J Pharm Sci* **60**, 1458-&, doi:DOI 10.1002/jps.2600601003 (1971).
71 Hartshorne, N. H. & Woodard, G. D. Mesomorphism in the System Disodium Chromoglycate-Water. *Molecular Crystals and Liquid Crystals* **23**, 343-368, doi:10.1080/15421407308083381 (1973).
72 Yu, L. J. & Saupe, A. Deuteron Resonance of D2o of Nematic Disodium-Cromoglycate Water-Systems. *Molecular Crystals and Liquid Crystals* **80**, 129-134, doi:Doi 10.1080/00268948208071026 (1982).
73 Attwood, T. K., Lydon, J. E. & Jones, F. The Chromonic Phases of Dyes. *Liq. Cryst.* **1**, 499-507, doi:Doi 10.1080/02678298608086274 (1986).
74 Masters, A. Chromonic liquid crystals: more questions than answers. *Liquid Crystals Today* **25**, 30-37, doi:10.1080/1358314X.2016.1149925 (2016).
75 Park, H.-S. & Lavrentovich, O. D. in *Liquid Crystals Beyond Displays* 449-484 (John Wiley & Sons, Inc., 2012).
76 Maiti, P. K., Lansac, Y., Glaser, M. A. & Clark, N. A. Isodesmic self-assembly in lyotropic chromonic systems. *Liq. Cryst.* **29**, 619-626, doi:10.1080/02678290110113838 (2002).
77 Mohanty, S., Chou, S. H., Brostrom, M. & Aguilera, J. Predictive modeling of self assembly of chromonics materials. *Molecular Simulation* **32**, 1179-1185, doi:10.1080/08927020601059919 (2006).
78 Walker, M. & Wilson, M. R. A Simple Model for Chromonic Aggregation. *Molecular Crystals and Liquid Crystals* **612**, 117-125, doi:10.1080/15421406.2015.1030580 (2015).
79 Collings, P. J. *et al.* The nature of the assembly process in chromonic liquid crystals. *Liquid Crystals Reviews* **3**, 1-27, doi:10.1080/21680396.2015.1025305 (2015).
80 Ould-Moussa, N. *et al.* Dispersion and orientation of single-walled carbon nanotubes in a chromonic liquid crystal. *Liq. Cryst.* **40**, 1628-1635, doi:10.1080/02678292.2013.772254 (2013).
81 Park, H.-S., Agarwal, A., Kotov, N. A. & Lavrentovich, O. D. Controllable Side-by-Side and End-to-End Assembly of Au Nanorods by Lyotropic Chromonic Materials. *Langmuir* **24**, 13833-13837, doi:10.1021/la803363m (2008).
82 Jeong, J. *et al.* Homeotropic Alignment of Lyotropic Chromonic Liquid Crystals Using Noncovalent Interactions. *Langmuir* **30**, 2914-2920, doi:10.1021/la404893t (2014).
83 Guo, F., Mukhopadhyay, A., Sheldon, B. W. & Hurt, R. H. Vertically Aligned Graphene Layer Arrays from Chromonic Liquid Crystal Precursors. *Advanced Materials* **23**, 508-513, doi:10.1002/adma.201003158 (2011).

84 Martens, K. *et al.* Alignment and Graphene-Assisted Decoration of Lyotropic Chromonic Liquid Crystals Containing DNA Origami Nanostructures. *Small* **12**, 1658-1666, doi:10.1002/smll.201503382 (2016).
85 Shiyanovskii, S. V. *et al.* Real-time microbe detection based on director distortions around growing immune complexes in lyotropic chromonic liquid crystals. *Physical Review E* **71**, 020702 (2005).
86 Yeh, P. & Gu, C. *Optics of Liquid Crystal Displays*. (Wiley Publishing, 2009).
87 Kuriabova, T., Betterton, M. D. & Glaser, M. A. Linear aggregation and liquid-crystalline order: comparison of Monte Carlo simulation and analytic theory. *Journal of Materials Chemistry* **20**, 10366-10383, doi:10.1039/C0JM02355H (2010).
88 Park, H.-S., Kang, S.-W., Tortora, L., Kumar, S. & Lavrentovich, O. D. Condensation of Self-Assembled Lyotropic Chromonic Liquid Crystal Sunset Yellow in Aqueous Solutions Crowded with Polyethylene Glycol and Doped with Salt. *Langmuir* **27**, 4164-4175, doi:10.1021/la200505y (2011).
89 Drzaic, P. S. *Liquid Crystal Dispersions*. (World Scientific, 1995).
90 Drzaic, P. S. A case of mistaken identity: spontaneous formation of twisted bipolar droplets from achiral nematic materials. *Liq. Cryst.* **26**, 623-627, doi:10.1080/026782999204660 (1999).
91 Lin, I. H. *et al.* Endotoxin-Induced Structural Transformations in Liquid Crystalline Droplets. *Science* **332**, 1297 (2011).
92 Lopez-Leon, T., Koning, V., Devaiah, K. B. S., Vitelli, V. & Fernandez-Nieves, A. Frustrated nematic order in spherical geometries. *Nat Phys* **7**, 391-394, doi:http://www.nature.com/nphys/journal/v7/n5/abs/nphys1920.html#supplementary-information (2011).
93 Fernández-Nieves, A. *et al.* Novel Defect Structures in Nematic Liquid Crystal Shells. *Physical Review Letters* **99**, 157801 (2007).
94 Parshin, A. M., Nazarov, V. G., Zyryanov, V. Y. & Shabanov, V. F. Bipolar-homogeneous structural phase transition in nematic droplets formed in the polymer matrix in a magnetic field. *Crystallography Reports* **54**, 1191-1196, doi:10.1134/S1063774509070098 (2009).
95 Humar, M. & Muševič, I. Surfactant sensing based on whispering-gallery-mode lasing in liquid-crystal microdroplets. *Opt. Express* **19**, 19836-19844, doi:10.1364/OE.19.019836 (2011).
96 Li, J., Gauza, S. & Wu, S.-T. Temperature effect on liquid crystal refractive indices. *Journal of Applied Physics* **96**, 19-24, doi:10.1063/1.1757034 (2004).
97 Alexe-Ionescu, A. L. On the temperature dependence of the surface elastic constant K13. *Physics Letters A* **175**, 345-348, doi:http://dx.doi.org/10.1016/0375-9601(93)90632-A (1993).
98 Pergamenshchik, V. M. & Žumer, S. Surface variations of the density and scalar order parameter and the elastic constants of a uniaxial nematic phase. *Physical Review E* **59**, R2531-R2534 (1999).
99 Faetti, S. The effects of curvature on nematic liquid crystals confined in a cylindrical cavity. *Physics Letters A* **237**, 264-270, doi:http://dx.doi.org/10.1016/S0375-9601(97)00834-7 (1998).

100 Barbero, G., Gliozzi, A. S., Scalerandi, M. & Evangelista, L. R. Generalization of Berreman's model to the case of large amplitude of the grooves. *Phys. Rev. E* **77**, 051703 (2008).
101 Barbero, G., Sparavigna, A. & Strigazzi, A. The structure of the distortion free-energy density in nematics: Second-order elasticity and surface terms. *Il Nuovo Cimento D* **12**, 1259-1272, doi:10.1007/BF02450392 (1990).
102 Barbero, G. NON-LOCAL TERMS IN THE ELASTIC FREE ENERGY OF DISTORTED NEMATICS. *Modern Physics Letters B* **04**, 983-988, doi:10.1142/S0217984990001227 (1990).
103 Miller, D. S. & Abbott, N. L. Influence of droplet size, pH and ionic strength on endotoxin-triggered ordering transitions in liquid crystalline droplets. *Soft Matter* **9**, 374-382, doi:10.1039/C2SM26811F (2013).
104 Meyer, R. B. On the existence of even indexed disclinations in nematic liquid crystals. *Philosophical Magazine* **27**, 405-424, doi:10.1080/14786437308227417 (1973).
105 Crawford, G. P., Allender, D. W. & Doane, J. W. Surface elastic and molecular-anchoring properties of nematic liquid crystals confined to cylindrical cavities. *Physical Review A* **45**, 8693-8708 (1992).
106 Jen, S., Clark, N. A., Pershan, P. S. & Priestley, E. B. Polarized Raman scattering studies of orientational order in uniaxial liquid crystalline phases. *The Journal of Chemical Physics* **66**, 4635-4661, doi:10.1063/1.433720 (1977).
107 Jen, S., Clark, N. A., Pershan, P. S. & Priestley, E. B. Raman Scattering from a Nematic Liquid Crystal: Orientational Statistics. *Phys. Rev. Lett.* **31**, 1552-1556 (1973).
108 Park, M. S. *et al.* Raman Scattering Study of Phase Biaxiality in a Thermotropic Bent-Core Nematic Liquid Crystal. *Phys. Rev. Lett.* **105**, 027801 (2010).
109 Southern, C. D. & Gleeson, H. F. Using the full Raman depolarisation in the determination of the order parameters in liquid crystal systems. *Eur. Phys. J. E* **24**, 119-127, doi:10.1140/epje/i2007-10223-3 (2007).
110 Madhusudana, N. V. & Pratibha, R. Elasticity and Orientational Order in Some Cyanobiphenyls: Part IV. Reanalysis of the Data. *Molecular Crystals and Liquid Crystals* **89**, 249-257, doi:10.1080/00268948208074481 (1982).
111 Miyano, K. Order parameters of a nematic liquid crystal measured by Raman scattering. *Physics Letters A* **63**, 37-38, doi:http://dx.doi.org/10.1016/0375-9601(77)90600-4 (1977).
112 Miyano, K. Raman depolarization ratios and order parameters of a nematic liquid crystal. *The Journal of Chemical Physics* **69**, 4807-4813, doi:10.1063/1.436508 (1978).
113 Luckhurst, G. R. & Viloria, F. R. The relationship between the second and fourth rank order parameters for liquid crystals composed of non-rigid molecules. *Molecular Crystals and Liquid Crystals* **72**, 201-209, doi:10.1080/01406568208084680 (1982).
114 Feng, K., Woo, C.-W. & Sheng, P. Anisotropic steric effects and negative $〈{P}_{4}〉$ in nematic liquid crystals. *Physical Review A* **28**, 1587-1595 (1983).

115 Seeliger, R., Haspeklo, H. & Noack, F. Raman studies of <P 2> and <P 4> of some homologous nematic liquid crystals with small optical anisotropy. *Molecular Physics* **49**, 1039-1063, doi:10.1080/00268978300101761 (1983).
116 Joshi, L., Kang, S. W., Agra-Kooijman, D. M. & Kumar, S. Concentration, temperature, and pH dependence of sunset-yellow aggregates in aqueous solutions: An x-ray investigation. *Phys. Rev. E* **80**, doi:10.1103/PhysRevE.80.041703 (2009).
117 Kostko, A. F. *et al.* Salt effects on the phase behavior, structure, and rheology of chromonic liquid crystals. *J. Phys. Chem. B* **109**, 19126-19133, doi:10.1021/jp052575u (2005).
118 Lydon, J. Chromonic review. *Journal of Materials Chemistry* **20**, 29, doi:10.1039/B926374H (2010).
119 Park, H. S., Kang, S. W., Tortora, L., Kumar, S. & Lavrentovich, O. D. Condensation of Self-Assembled Lyotropic Chromonic Liquid Crystal Sunset Yellow in Aqueous Solutions Crowded with Polyethylene Glycol and Doped with Salt. *Langmuir* **27**, 4164-4175, doi:10.1021/la200505y (2011).
120 Nazarenko, V. G. *et al.* Lyotropic chromonic liquid crystal semiconductors for water-solution processable organic electronics. *Applied Physics Letters* **97**, 263305-263303 (2010).
121 Shiyanovskii, S. V. *et al.* Real-time microbe detection based on director distortions around growing immune complexes in lyotropic chromonic liquid crystals. *Phys. Rev. E* **71**, doi:Artn 020702
Doi 10.1103/Physreve.71.020702 (2005).
122 Bae, Y. J., Yang, H. J., Shin, S. H., Jeong, K. U. & Lee, M. H. A novel thin film polarizer from photocurable non-aqueous lyotropic chromonic liquid crystal solutions. *Journal of Materials Chemistry* **21**, 2074-2077, doi:10.1039/c0jm03882b (2011).
123 Lavrentovich, M., Sergan, T. & Kelly, J. Planar and twisted lyotropic chromonic liquid crystal cells as optical compensators for twisted nematic displays. *Liq. Cryst.* **30**, 851-859, doi:10.1080/0267829031000121017 (2003).
124 Nastishin, Y. A. *et al.* Optical characterization of the nematic lyotropic chromonic liquid crystals: Light absorption, birefringence, and scalar order parameter. *Phys. Rev. E* **72**, doi:10.1103/PhysRevE.72.041711 (2005).
125 Taratuta, V. G., Srajer, G. M. & Meyer, R. B. PARALLEL ALIGNMENT OF POLY-GAMMA-BENZYL-GLUTAMATE NEMATIC LIQUID-CRYSTAL AT A SOLID-SURFACE. *Molecular Crystals and Liquid Crystals* **116**, 245-252, doi:10.1080/00268948508074576 (1985).
126 Toney, M. F. *et al.* NEAR-SURFACE ALIGNMENT OF POLYMERS IN RUBBED FILMS. *Nature* **374**, 709-711, doi:10.1038/374709a0 (1995).
127 Srinivasarao, M. & Berry, G. C. Rheo-optical studies on aligned nematic solutions of a rodlike polymer. *Journal of Rheology* **35**, 379-397 (1991).
128 Srinivasarao, M. RHEOLOGY AND RHEO-OPTICS OF POLYMER LIQUID CRYSTALS. *International Journal of Modern Physics B* **09**, 2515-2572, doi:10.1142/S0217979295000951 (1995).

129 Tone, C. M., De Santo, M. P. & Ciuchi, F. Alignment of Chromonic Liquid Crystals: A Difficult Task. *Molecular Crystals and Liquid Crystals* **576**, 2-7, doi:10.1080/15421406.2013.789393 (2013).
130 Tone, C. M., De Santo, M. P., Buonomenna, M. G., Golemme, G. & Ciuchi, F. Dynamical homeotropic and planar alignments of chromonic liquid crystals. *Soft Matter* **8**, 8478-8482, doi:10.1039/c2sm26021b (2012).
131 Ichimura, K., Fujiwara, T., Momose, M. & Matsunaga, D. Surface-assisted photoalignment control of lyotropic liquid crystals. Part 1. Characterisation and photoalignment of aqueous solutions of a water-soluble dye as lyotropic liquid crystals. *Journal of Materials Chemistry* **12**, 3380-3386, doi:10.1039/B208310H (2002).
132 McGinn, C. K., Laderman, L. I., Zimmermann, N., Kitzerow, H.-S. & Collings, P. J. Planar anchoring strength and pitch measurements in achiral and chiral chromonic liquid crystals using 90-degree twist cells. *Phys. Rev. E* **88**, 062513 (2013).
133 McGuire, A., Yi, Y. & Clark, N. A. Orthogonal Orientation of Chromonic Liquid Crystals by Rubbed Polyamide Films. *ChemPhysChem* **15**, 1376-1380, doi:10.1002/cphc.201301040 (2014).
134 Berreman, D. W. SOLID SURFACE SHAPE AND ALIGNMENT OF AN ADJACENT NEMATIC LIQUID-CRYSTAL. *Phys. Rev. Lett.* **28**, 1683-&, doi:10.1103/PhysRevLett.28.1683 (1972).
135 Kumar, S., Kim, J.-H. & Shi, Y. What Aligns Liquid Crystals on Solid Substrates? The Role of Surface Roughness Anisotropy. *Phys. Rev. Lett.* **94**, 077803 (2005).
136 Jeong, H. S. *et al.* Bifunctional ITO layer with a high resolution, surface nano-pattern for alignment and switching of LCs in device applications. *NPG Asia Mater.* **4**, doi:10.1038/am.2012.12 (2012).